CSIRO
AUSTRALIA

LADM: A Lagrangian Atmospheric Dispersion Model

W.L. Physick, J.A. Noonan, J.L. McGregor,
P.J. Hurley, D.J. Abbs and P.C. Manins

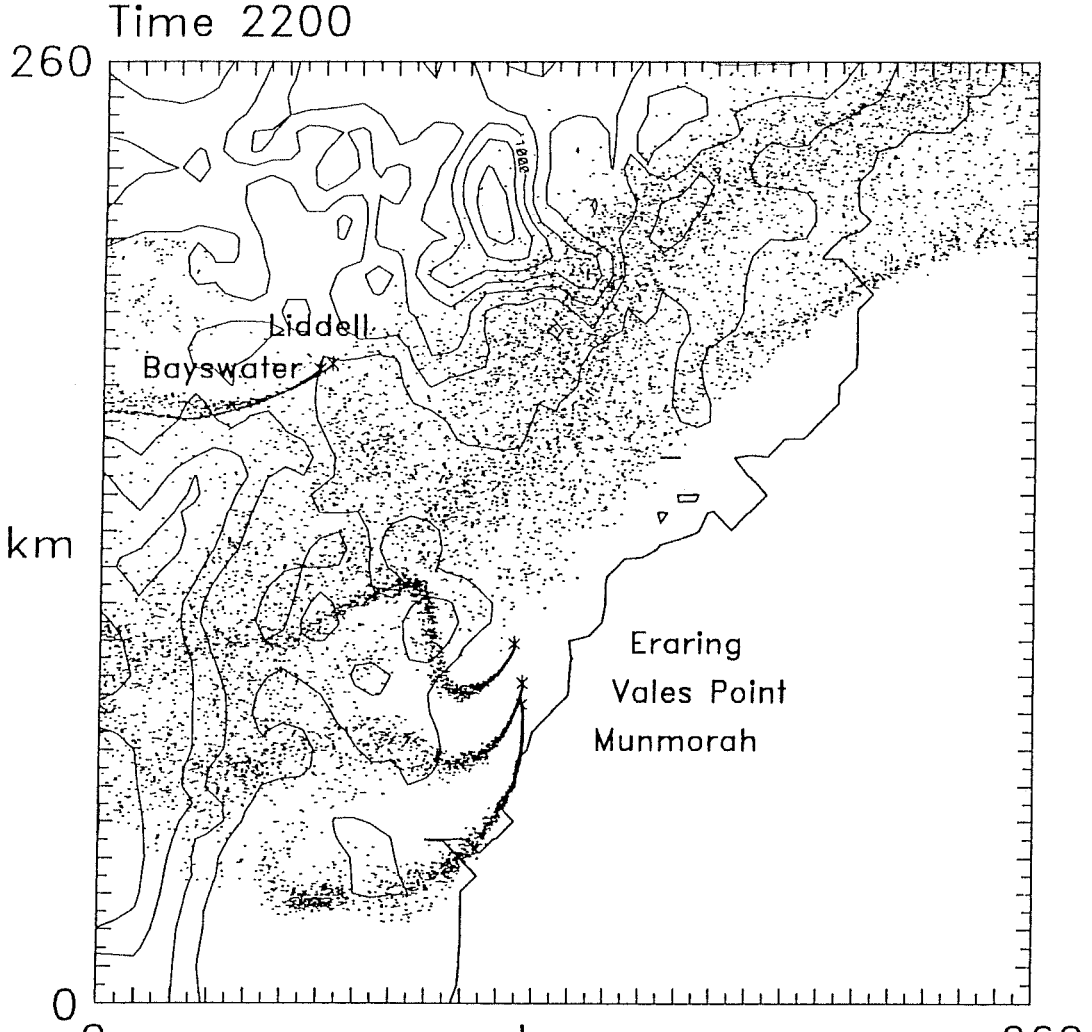

CSIRO DIVISION OF ATMOSPHERIC RESEARCH TECHNICAL PAPER NO. 24

CSIRO
AUSTRALIA

LADM: A Lagrangian Atmospheric Dispersion Model

W.L. Physick, J.A. Noonan, J.L. McGregor,
P.J. Hurley, D.J. Abbs and P.C. Manins

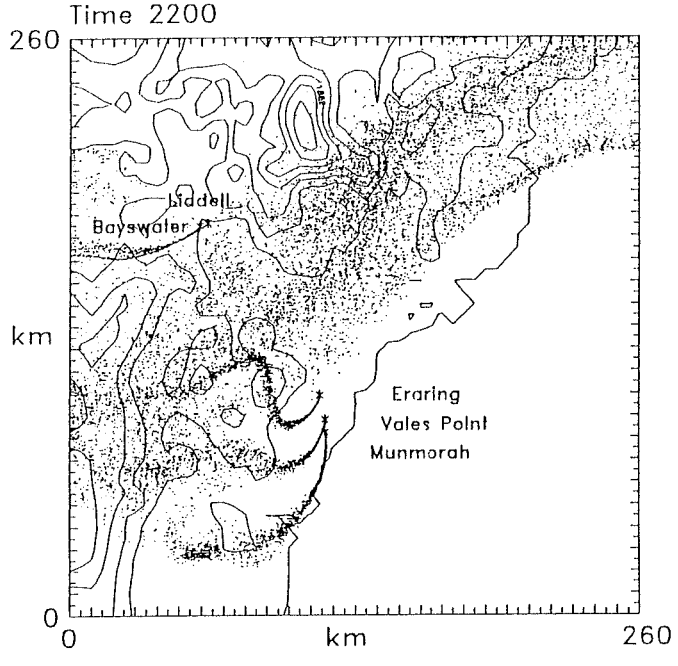

CSIRO DIVISION OF ATMOSPHERIC RESEARCH TECHNICAL PAPER NO. 24

National Library of Australia Cataloguing-in-Publication Entry

LADM: a Lagrangian atmospheric dispersion model.

Bibliography.
ISBN 0 643 05247 X

1. Air-Pollution-Mathematical models.
2. Atmospheric diffusion-Mathematical models.
I. Physick, William Lloyd. II. CSIRO. Division of Atmospheric Research.
(Series: CSIRO Division of Atmospheric Research technical paper; no. 24)

628.53015118

Printed on recycled and environmentally friendly paper

Erratum sheet for CSIRO Technical Report No.24; LADM: A Lagrangian Atmospheric Dispersion Model.

Page

3 $$\frac{\partial \phi}{\partial \sigma} = -\frac{RT}{\sigma} \qquad (2.1.3)$$

22
$$\frac{\partial z_i}{\partial t} = -\underline{V}.\nabla z_i + w_i$$
$$+1.8\left(w_*^3 + 1.1u_*^3 - 3.3u_*^2|f|z_i\right)/\left\{\left(gz_i^2/\theta_s\right)\partial\theta^+/\partial z + 9w_*^2 + 7.2u_*^2\right\} \qquad (2.3.4)$$

26 $$u_i''(t+\Delta t) = u_i''(t) + a_i\Delta t + (C_0\varepsilon)^{1/2} r_i\, \Delta t^{1/2} \qquad (3.1.3)$$

30 $$\sigma_w = 1.2l\left[\frac{Ri_{cr} - Ri}{Ri_{cr}}\right]^{0.58}\left|\frac{dV}{dz}\right| \qquad \text{for Ri} < \text{Ri}_{\text{cr}} \qquad (3.3.2)$$

31 $$T_{L,w} = \beta T_{E,w} \qquad (3.3.3)$$

31 $$\sigma_u = \sigma_v = 2.3u_* \qquad (3.3.4)$$

111 $$0 = \frac{1}{\rho}\frac{\partial p}{\partial z} + g \qquad (A.3)$$

111 $$\frac{1}{\rho}\frac{\partial \rho}{\partial t} + \frac{u}{\rho}\frac{\partial \rho}{\partial x} + \frac{v}{\rho}\frac{\partial \rho}{\partial y} + \frac{w}{\rho}\frac{\partial \rho}{\partial z} + \frac{\partial u}{\partial x} + \frac{\partial v}{\partial y} + \frac{\partial w}{\partial z} = 0 \qquad (A.4)$$

LADM: A Lagrangian Atmospheric Dispersion Model

W.L. Physick, J.A. Noonan, J.L. McGregor,
P.J. Hurley, D.J. Abbs and P.C. Manins

CSIRO, Division of Atmospheric Research
Private Bag 1, Mordialloc, Vic 3195, Australia

Abstract

This Report provides a detailed description of the equations and parameterizations used in LADM Version 1.2. Meteorological and dispersion predictions are compared to experimental data. Upgrades to be incorporated in the next version of LADM are also presented.

1. INTRODUCTION

The Lagrangian Atmospheric Dispersion Model (LADM) is an air pollution dispersion model which simulates the transport and diffusion of emissions of pollutants from discrete sources for impact distances ranging from hundreds of metres to a few hundred kilometres. It is applicable to air quality studies that involve simple to very rugged terrain, time-varying conditions such as the diurnal cycle, and the interaction of complex wind flows such as sea breezes and drainage winds. The system is most readily applied to emissions from facilities such as power stations, refinery complexes, and smelters.

There are two components to LADM:

A prognostic windfield model. The model equations and parameterizations are presented in Chapter 2. Developed primarily by J.McGregor, this model predicts the three-dimensional windfield and turbulence characteristics on a grid in the region of application. The winds and turbulence fields are stored for later use by the second component of LADM. By splitting the advective and gravity wave terms in the model equations and by taking a semi-Lagrangian approach to the computation of horizontal advection, the model is able to

circumvent the conventional Courant-Friedrichs-Lewy restriction on the size of the timestep used to step forward through the integration. In our work, we usually use a timestep of 300 seconds with a 10 km grid spacing, compared to perhaps 90 seconds with the conventional explicit Eulerian-based advection techniques.

As the modelled region must be large enough to include all relevant terrain that causes the local wind to deviate from the large-scale (synoptic) wind, domain sizes usually range from about 200 x 200 km to 500 x 500 km. The associated grid resolution is usually of the order of 10 km, and is often too coarse to resolve features of interest in a local valley or lake region. For this reason the model was designed to be nested within itself so that further runs with finer resolution and smaller domains can be carried out. These runs take their boundary conditions from the previous run. A grid spacing as small as 1 km is used in LADM.

The model equations, derived for an (x,y,σ) coordinate system in Appendix A, are presented in Section 2.1, followed in Section 2.2 by the numerical techniques employed in solving these equations. Details of boundary-layer and radiation parameterizations, boundary conditions and initialization can also be found in Chapter 2.

A Lagrangian particle dispersion model. This component, details of which can be found in Chapter 3, predicts the dispersion (including a plume-rise height for buoyancy emissions) from pollutant sources using the predicted wind and turbulence fields. Particles are released each timestep from the sources at a rate proportional to the specified emissions. Each particle is tracked as it is transported by the wind and by random perturbations simulating the turbulence. Hourly-averaged ground-level concentrations are calculated by counting particles in small boxes covering the model domain. Box sizes are 25 m deep and range horizontally from 250 x 250 m to 1000 x 1000 m, according to the distance from the source.

2. THE MESOSCALE WINDFIELD MODEL

2.1 Model equations

The windfield component of LADM solves five prognostic equations in an (x,y,σ) coordinate system, where $\sigma = p/p_s$ and p_s is the surface pressure. In

Appendix A, we use the appropriate coordinate transformations to derive these equations from the standard conservation and thermodynamic laws written in Cartesian (x,y,z) form. In equations (2.1.1-6), p_s, T and ϕ denote the mesoscale components of surface pressure, temperature and geopotential height. The synoptic components have been eliminated by partitioning the variables into a base state plus synoptic and mesoscale perturbations and by representing the synoptic pressure gradient by an equivalent velocity (see Appendix A). In summary the σ-coordinate system equations used in LADM are:
For the u-component of velocity,

$$\frac{Du}{Dt} - f(v-v_g) = - RT \frac{\partial(\ln p_s)}{\partial x} - \frac{\partial \phi}{\partial x} + (\underline{\nabla}_H \cdot K_m^H \underline{\nabla}_H) u - \frac{g}{p_s} \frac{\partial \tau_{\sigma x}}{\partial \sigma}. \qquad (2.1.1)$$

For the v-component of velocity,

$$\frac{Dv}{Dt} + f(u-u_g) = - RT \frac{\partial(\ln p_s)}{\partial y} - \frac{\partial \phi}{\partial y} + (\underline{\nabla}_H \cdot K_m^H \underline{\nabla}_H) v - \frac{g}{p_s} \frac{\partial \tau_{\sigma y}}{\partial \sigma}. \qquad (2.1.2)$$

The geopotential height ϕ of a σ-surface is obtained diagnostically from

$$\frac{\partial \phi}{\partial \sigma} = \frac{RT}{\sigma} . \qquad (2.1.3)$$

For the surface pressure p_s,

$$\frac{D(\ln p_s)}{Dt} + \underline{\nabla}_H \cdot \underline{v}_H + \frac{\partial \dot{\sigma}}{\partial \sigma} = 0. \qquad (2.1.4)$$

For temperature T,

$$\frac{DT}{Dt} = \frac{TR}{c_p} \left\{ \frac{D(\ln p_s)}{Dt} + \frac{\dot{\sigma}}{\sigma} \right\} + (\underline{\nabla}_H \cdot K_h^H \underline{\nabla}_H) T + \frac{g}{c_p p_s} \frac{\partial H}{\partial \sigma} + \left(\frac{\partial T}{\partial t} \right)_{rad} . \qquad (2.1.5)$$

For specific humidity q,

$$\frac{Dq}{Dt} = (\underset{-H}{\nabla} \cdot K_q^H \underset{-H}{\nabla}) q + \frac{g}{L\, p_s} \frac{\partial E}{\partial \sigma} , \qquad (2.1.6)$$

where $$\frac{D}{Dt} = \frac{\partial}{\partial t} + u \frac{\partial}{\partial x} + v \frac{\partial}{\partial y} + \dot{\sigma} \frac{\partial}{\partial \sigma}$$

and ∇_H is the horizontal Laplacian operator. Other variables are denoted by the following symbols: R is the gas constant for dry air, f is the Coriolis parameter, u_g, v_g are synoptic wind components, K_m^H, K_h^H and K_q^H are horizontal diffusion coefficients for momentum, heat and moisture respectively, g is gravitational acceleration, c_p is the specific heat of dry air, L is the latent heat of condensation, E is evaporative flux, H is sensible heat flux, $\tau_{\sigma x}$ and $\tau_{\sigma y}$ are the momentum flux components, and $\dot{\sigma}$ is the vertical velocity in the (x,y,σ) coordinate system.

2.2 Numerical techniques

2.2.1 The model grid

The model grid is an Arakawa C-grid and is illustrated schematically below. The horizontal velocity u is calculated at the points marked u, v is calculated at the points marked v and all other variables are calculated at the points marked T. Throughout this report, (i,j,k) is always used to denote a (x,y,σ) position, respectively, and (il,jl,kl) are the (i,j,k) maximum values. The variables at T(i=1,j), T(i,j=1), v(i=1,j) and u(i,j=1) are not used; their purpose is to allow the same array sizes for all the three-dimensional variables. The boundaries used by the model are shown by the boxed-in region and the variables outside this region are set equal to their nearest equivalent neighbour.

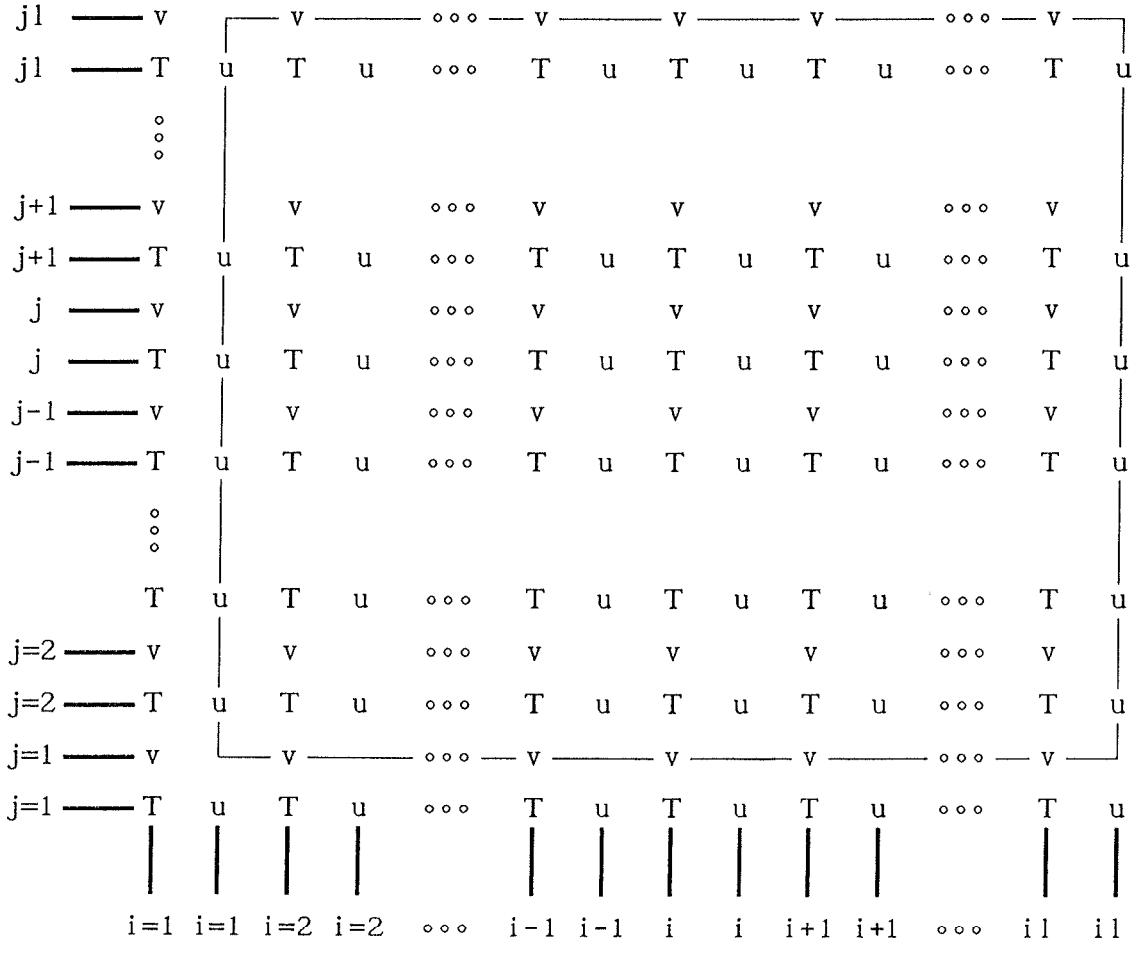

2.2.2 Method of solution

The method of solution for each of the five prognostic equations is similar and the procedure is detailed below for the u-momentum equation.

The u-momentum equation (eq. 2.1.1) can be written as

$$\frac{D_H u}{Dt} = -\dot{\sigma}\frac{\partial u}{\partial \sigma} + f(v-v_g) - RT\frac{\partial(\ln p_s)}{\partial x} - \frac{\partial \phi}{\partial x} + F_{turb}$$

where $D_H u/Dt$ is the horizontal Lagrangian total derivative and F_{turb} denotes the turbulence terms.

In finite-difference form it becomes

$$\frac{u^{t+\Delta t}_{i,j,k} - u^{t}_{*}}{\Delta t} = \frac{1}{2}\left[\left\{ aa \right\}^{t+\Delta t}_{i,j,k} + \left\{ aa \right\}^{t}_{*} \right] \qquad (2.2.1)$$

where $$aa = -\dot{\sigma}\frac{\partial u}{\partial \sigma} + f(v-v_g) - RT\frac{\partial(\ln p_s)}{\partial x} - \frac{\partial \phi}{\partial x}.$$

The subscript i,j,k represents the (i,j,k) grid point (in the (x,y,σ) direction, respectively) and the * subscript represents the position of the departure point of the parcel on the k^{th} σ-surface. The turbulence terms do not appear as they are solved separately and will be discussed later.

Rearranging eq. (2.2.1) gives

$$u^{t+\Delta t}_{i,j,k} - \frac{\Delta t}{2}\left\{ aa \right\}^{t+\Delta t}_{i,j,k} = UX^{t}_{*}$$

where

$$UX^{t} = u^{t} + \frac{\Delta t}{2}\left\{ aa \right\}^{t}.$$

Adding and subtracting various terms gives

$$u^{t+\Delta t}_{i,j,k} + \left\{ -u^{t}_{i,j,k} + u^{t}_{i,j,k} \right\} - \frac{\Delta t}{2}\left\{ aa \right\}^{t+\Delta t}_{i,j,k}$$

$$+ \left\{ \frac{\Delta t}{2}\left\{ aa \right\}^{t}_{i,j,k} - \frac{\Delta t}{2}\left\{ aa \right\}^{t}_{i,j,k} \right\}$$

$$= UX^{t}_{*}$$

which when rearranged becomes

$$u^{t+\Delta t}_{i,j,k} - u^{t}_{i,j,k} - \frac{\Delta t}{2}\left\{ aa \right\}^{t+\Delta t}_{i,j,k} - \frac{\Delta t}{2}\left\{ aa \right\}^{t}_{i,j,k}$$

$$= UX^{t}_{*} - u^{t}_{i,j,k} - \frac{\Delta t}{2}\left\{ aa \right\}^{t}_{i,j,k}$$

$$= UX^{t}_{*} - UX^{t}_{i,j,k} \; .$$

This equation is a finite-difference expression for

$$\frac{\partial u}{\partial t}_{i,j,k} = \left\{ aa \right\}_{i,j,k} + \frac{UX_{*}}{\Delta t} - \frac{UX}{\Delta t}_{i,j,k} \; . \qquad (2.2.2)$$

In a similar way the v-momentum equation becomes

$$\frac{\partial v}{\partial t}_{i,j,k} = \left\{ bb \right\}_{i,j,k} + \frac{VX}{\Delta t}_{*} - \frac{VX}{\Delta t}_{i,j,k} \qquad (2.2.3)$$

where $$bb = -\dot{\sigma}\frac{\partial v}{\partial \sigma} - f(u-u_g) - RT\frac{\partial(\ln p_s)}{\partial y} - \frac{\partial \phi}{\partial y} \; .$$

These equations, as shown below, are solved simultaneously with a fractional time step equal to $\Delta t/\alpha$, where $\alpha = 2.0c\Delta t/\Delta s$ and c $(=(gH)^{0.5}$ where H is the height of the top model level) is the approximate speed of the external mode. The coefficient of 2.0 has been determined through numerical experiments rather than theoretically. Δt is the full time step and Δs is equal to the horizontal grid spacing. Rearranging the equations and dropping the subscripts gives

$$\frac{\partial u}{\partial t} = fv + AA + \frac{UX_{*}}{\Delta t} - \frac{UX}{\Delta t}_{i,j,k} \qquad (2.2.4a)$$

and $$\frac{\partial v}{\partial t} = - fu + BB + \frac{VX_*}{\Delta t} - \frac{VX_{i,j,k}}{\Delta t} \qquad (2.2.4b)$$

where $$AA = -\dot{\sigma}\frac{\partial u}{\partial \sigma} - fv_g - RT\frac{\partial(\ln p_s)}{\partial x} - \frac{\partial \phi}{\partial x}$$

and $$BB = -\dot{\sigma}\frac{\partial v}{\partial \sigma} + fu_g - RT\frac{\partial(\ln p_s)}{\partial y} - \frac{\partial \phi}{\partial y}.$$

In finite difference form the equations (2.2.4) become at the (i,j,k) point

$$u^{t+\Delta t''} - u^{t+\Delta t'} = \frac{\Delta t}{\alpha}\left\{\frac{v^{t+\Delta t''} + v^{t+\Delta t'}}{2}\right\} f + \frac{\Delta t}{\alpha}\left\{AA^{t+\Delta t'} + \frac{UX^t_*}{\Delta t} - \frac{UX^t_{i,j,k}}{\Delta t}\right\}, \qquad (2.2.5)$$

$$v^{t+\Delta t''} - v^{t+\Delta t'} = -\frac{\Delta t}{\alpha}\left\{\frac{u^{t+\Delta t''} + u^{t+\Delta t'}}{2}\right\} f + \frac{\Delta t}{\alpha}\left\{BB^{t+\Delta t'} + \frac{VX^t_*}{\Delta t} - \frac{VX^t_{i,j,k}}{\Delta t}\right\}, \qquad (2.2.6)$$

where $$\Delta t'' = n\Delta t/\alpha, \quad \Delta t' = (n-1)\Delta t/\alpha \qquad (2.2.7)$$

and $n = 1,\ldots,\alpha$ is the number of fractional time steps within each full time step Δt.

Equation (2.2.6) gives an expression for $v^{t+\Delta t''}$ which is substituted into equation (2.2.5) to solve for u at the new time step, $u^{t+\Delta t''}$. Eq. (2.2.5) becomes

$$u^{t+\Delta t''} - u^{t+\Delta t'} = \frac{\Delta t}{2\alpha}\left\{2v^{t+\Delta t'} + \frac{\Delta t}{\alpha}\left\{BB^{t+\Delta t'} + \frac{VX^t_*}{\Delta t} - \frac{VX^t_{i,j,k}}{\Delta t}\right\}\right\} f$$

$$- \left\{ \frac{\Delta t}{2\alpha} f \right\}^2 \left\{ u^{t+\Delta t''} + u^{t+\Delta t'} \right\}$$

$$+ \frac{\Delta t}{\alpha} \left\{ AA^{t+\Delta t'} + \frac{UX^t_*}{\Delta t} - \frac{UX^t_{i,j,k}}{\Delta t} \right\} .$$

Rearranging gives

$$\left\{ 1 + \left\{ \frac{\Delta t}{2\alpha} f \right\}^2 \right\} u^{t+\Delta t''} = \left\{ 1 - \left\{ \frac{\Delta t}{2\alpha} f \right\}^2 \right\} u^{t+\Delta t'}$$

$$+ \frac{\Delta t}{2\alpha} f \left\{ 2v^{t+\Delta t'} + \frac{\Delta t}{\alpha} \left\{ BB^{t+\Delta t'} + \frac{VX^t_*}{\Delta t} - \frac{VX^t_{i,j,k}}{\Delta t} \right\} \right\}$$

$$+ \frac{\Delta t}{\alpha} \left\{ AA^{t+\Delta t'} + \frac{UX^t_*}{\Delta t} - \frac{UX^t_{i,j,k}}{\Delta t} \right\} ,$$

and finally $u^{t+\Delta t''}$ can be written as

$$u^{t+\Delta t''} = \frac{\left[\left\{ 1 - \left\{ \frac{\Delta t}{2\alpha} f \right\}^2 \right\} u^{t+\Delta t'} + \frac{\Delta t}{\alpha} \left\{ AA^{t+\Delta t'} + \frac{UX^t_*}{\Delta t} - \frac{UX^t_{i,j,k}}{\Delta t} \right\} \right]}{\left\{ 1 + \left\{ \frac{\Delta t}{2\alpha} f \right\}^2 \right\}}$$

$$+ \frac{\frac{\Delta t}{2\alpha} f \left\{ 2v^{t+\Delta t'} + \frac{\Delta t}{\alpha} \left\{ BB^{t+\Delta t'} + \frac{VX^t_*}{\Delta t} - \frac{VX^t_{i,j,k}}{\Delta t} \right\} \right\}}{\left\{ 1 + \left\{ \frac{\Delta t}{2\alpha} f \right\}^2 \right\}} .$$

Substituting this expression back into equation (2.2.6), gives for $v^{t+\Delta t''}$ after some manipulation

$$v^{t+\Delta t''} = \frac{\left[\left\{ 1 - \left\{ \frac{\Delta t}{2\alpha} f \right\}^2 \right\} v^{t+\Delta t'} + \frac{\Delta t}{\alpha} \left\{ BB^{t+\Delta t'} + \frac{VX^t_*}{\Delta t} - \frac{VX^t_{i,j,k}}{\Delta t} \right\} \right]}{\left\{ 1 + \left\{ \frac{\Delta t}{2\alpha} f \right\}^2 \right\}}$$

$$- \frac{\frac{\Delta t}{2\alpha} f \left\{ 2u^{t+\Delta t'} + \frac{\Delta t}{\alpha} \left\{ AA^{t+\Delta t'} + \frac{UX^t_*}{\Delta t} - \frac{UX^t_{i,j,k}}{\Delta t} \right\} \right\}}{\left\{ 1 + \left\{ \frac{\Delta t}{2\alpha} f \right\}^2 \right\}} .$$

An equation similar to eq.(2.2.2) can be obtained for T using the same method as that for u, and is

$$\frac{\partial T}{\partial t}_{i,j,k} = \left\{ - \dot{\sigma} \frac{\partial T}{\partial \sigma} + \frac{TR}{C_p} \left\{ \frac{D(\ln p_s)}{Dt} + \frac{\dot{\sigma}}{\sigma} \right\} \right\}_{I,j,k} + \frac{TX_*}{\Delta t} - \frac{TX_{I,j,k}}{\Delta t} ,$$

where

$$TX = T + \frac{\Delta t}{2} \left\{ - \dot{\sigma} \frac{\partial T}{\partial \sigma} + \frac{TR}{C_p} \left\{ \frac{D(\ln p_s)}{Dt} + \frac{\dot{\sigma}}{\sigma} \right\} \right\} .$$

The radiative cooling and turbulence terms do not appear in this expression and will be discussed later (see Sections 2.2.4 and 2.4). This equation is solved using the same fractional time step introduced above and becomes

$$T^{t+\Delta t''} - T^{t+\Delta t'} = \frac{\Delta t}{\alpha}\left\{ -\dot{\sigma}\frac{\partial T}{\partial \sigma} + \frac{TR}{C_P}\left\{ \frac{D(\ln p_s)}{Dt} + \frac{\dot{\sigma}}{\sigma} \right\} \right\}^{t+\Delta t'} + \frac{\Delta t}{\alpha}\left\{ \frac{TX_*}{\Delta t} - \frac{TX}{\Delta t} \right\}^{t}$$

where the subscripts, i,j,k, are implied.

The equation for surface pressure (2.1.4) is used to diagnose $\dot{\sigma}$ as follows:

$$\frac{\partial \dot{\sigma}}{\partial \sigma} = -\frac{\partial(\ln p_s)}{\partial t} - u\frac{\partial(\ln p_s)}{\partial x} - v\frac{\partial(\ln p_s)}{\partial y} - \underline{\nabla}_H \cdot \underline{v}_H \ .$$

Integrating the equation with respect to sigma, $\int_\sigma^0 d\sigma$, gives

$$\int_\sigma^0 \frac{\partial \dot{\sigma}}{\partial \sigma}\, d\sigma = \int_\sigma^0 \left(-\frac{\partial(\ln p_s)}{\partial t} - u\frac{\partial(\ln p_s)}{\partial x} - v\frac{\partial(\ln p_s)}{\partial y} - \underline{\nabla}_H \cdot \underline{v}_H \right) d\sigma \ ,$$

which reduces to

$$\left[\dot{\sigma} \right]_\sigma^0 = \left[-\frac{\partial(\ln p_s)}{\partial t}\,\sigma \right]_\sigma^0 + \int_\sigma^0 \left(-u\frac{\partial(\ln p_s)}{\partial x} - v\frac{\partial(\ln p_s)}{\partial y} - \underline{\nabla}_H \cdot \underline{v}_H \right) d\sigma$$

and finally, using $\dot{\sigma} = 0$ at $\sigma = 0$,

$$\dot{\sigma} = -\sigma\frac{\partial(\ln p_s)}{\partial t} + \int_\sigma^0 \left(u\frac{\partial(\ln p_s)}{\partial x} + v\frac{\partial(\ln p_s)}{\partial y} + \underline{\nabla}_H \cdot \underline{v}_H \right) d\sigma \ .$$

Equation (2.1.4) is also used to predict the surface pressure and is solved in a similar way to the u, v and T equations above. The resulting equation is

$$\frac{\partial(\ln p_s)}{\partial t}_{i,j,k} = \left\{ -\underline{\nabla}_H \cdot \underline{v}_H - \frac{\partial \dot{\sigma}}{\partial \sigma} \right\}_{i,j,k} + \frac{PSLX_*}{\Delta t} - \frac{PSLX_{1,j,k}}{\Delta t} \ ,$$

where

$$PSLX = \ln p_s + \frac{\Delta t}{2}\left\{ - \frac{\partial u}{\partial x} - \frac{\partial v}{\partial y} - \frac{\partial \dot{\sigma}}{\partial \sigma} \right\} .$$

This is solved by firstly integrating the equation with respect to sigma,

$$\int_{\sigma_k}^{0} \frac{\partial(\ln p_s)}{\partial t}\, d\sigma = \int_{\sigma_k}^{0} \left\{ - \frac{\partial u}{\partial x} - \frac{\partial v}{\partial y} - \frac{\partial \dot{\sigma}}{\partial \sigma} + \frac{PSLX_*}{\Delta t} - \frac{PSLX}{\Delta t} \right\} d\sigma ,$$

where the i,j,k subscripts have been dropped. This reduces to

$$- \frac{\partial(\ln p_s)}{\partial t}\, \sigma_k = \int_{\sigma_k}^{0} \left\{ - \frac{\partial u}{\partial x} - \frac{\partial v}{\partial y} + \frac{PSLX_*}{\Delta t} - \frac{PSLX}{\Delta t} \right\} d\sigma - \dot{\sigma}_k$$

and finally to

$$\frac{\partial(\ln p_s)}{\partial t} = \int_{0}^{1} \left\{ - \frac{\partial u}{\partial x} - \frac{\partial v}{\partial y} + \frac{PSLX_*}{\Delta t} - \frac{PSLX}{\Delta t} \right\} d\sigma$$

as $\dot{\sigma}$ =0 at the surface (σ =1).

Solving this with the fractional time steps gives

$$\ln p_s^{t+\Delta t''} - \ln p_s^{t+\Delta t'} = \frac{\Delta t}{\alpha}\left\{ \int_0^1 \left\{ - \frac{\partial u}{\partial x} - \frac{\partial v}{\partial y} \right\} d\sigma \right\}^{t+\Delta t'}$$

$$+ \frac{\Delta t}{\alpha}\left\{ \int_0^1 \left\{ \frac{PSLX_*}{\Delta t} - \frac{PSLX}{\Delta t} \right\} d\sigma \right\}^{t} .$$

The specific humidity equation (2.1.6) is solved in a slightly different manner. The equation can be written as

$$\frac{\partial q}{\partial t} = - u \frac{\partial q}{\partial x} - v \frac{\partial q}{\partial y} - \dot{\sigma} \frac{\partial q}{\partial \sigma} ,$$

where, as with the previous equations, the turbulence terms are omitted and will be discussed later. The equation is solved using a split approach.

Firstly, $$\frac{\partial q}{\partial t} = - u \frac{\partial q}{\partial x} - v \frac{\partial q}{\partial y} ,$$

can be written as $$\frac{D_H q}{Dt} = 0 ,$$

and therefore solved as $q^{t+\Delta t}_{i,j,k} = q^{t}_{*}$.

Then $$\frac{\partial q}{\partial t} = - \dot{\sigma} \frac{\partial q}{\partial \sigma}$$ is solved using the fractional time steps.

$$q^{t+\Delta t''} - q^{t+\Delta t'} = \frac{\Delta t}{\alpha} \left\{ - \dot{\sigma} \frac{\partial q^{t+\Delta t'}}{\partial \sigma} \right\} ,$$

with q^{t}_{*} as the first value for $q^{t+\Delta t'}$ in the fractional time step.

2.2.3 Advection

To compute the terms UX_*, VX_*, $PSLX_*$, TX_* and q_*, the horizontal position of the (i,j) parcel on each sigma surface at the previous time step, denoted as the departure point $\underline{r}$ = (X,Y), must be calculated. To calculate $\underline{r}$, a truncated Taylor series along the trajectory is used as follows (McGregor, 1993):

$$\underline{r}(t) \approx \underline{r}(t+\Delta t) + \sum_{n=1}^{N} \frac{(-\Delta t)^n}{n!} \frac{D^n \underline{r}(t+\Delta t)}{Dt^n}$$

and using dX/dt = u, the X position of the (i,j) parcel at the previous time step becomes

$$X(t) = i\,\Delta x - \Delta t\, u^{t+\Delta t} + \frac{\Delta t^2}{2}\left(\frac{\partial u}{\partial t} + u\frac{\partial u}{\partial x} + v\frac{\partial u}{\partial y}\right)^{t+\Delta t} - \frac{\Delta t^3}{6}\left(\frac{\partial}{\partial t} + u\frac{\partial}{\partial x} + v\frac{\partial}{\partial y}\right)\left(\frac{\partial u}{\partial t} + u\frac{\partial u}{\partial x} + v\frac{\partial u}{\partial y}\right)^{t+\Delta t} + O(\Delta t^4)$$

and similarly for Y. By retaining only terms up to $O(\Delta t^3)$, and by using the approximation that $\frac{D}{Dt} \approx u\frac{\partial}{\partial x} + v\frac{\partial}{\partial y}$, McGregor (1993) obtained the following expressions for the X and Y departure points:

$$X(t) = i\,\Delta x - u\,\Delta t + \frac{\Delta t^2}{2}\left(u\frac{\partial u}{\partial x} + v\frac{\partial u}{\partial y}\right) - \frac{\Delta t^3}{6}\left(u\frac{\partial}{\partial x}\left(u\frac{\partial u}{\partial x} + v\frac{\partial u}{\partial y}\right) + v\frac{\partial}{\partial y}\left(u\frac{\partial u}{\partial x} + v\frac{\partial u}{\partial y}\right)\right),$$

$$Y(t) = j\,\Delta y - v\,\Delta t + \frac{\Delta t^2}{2}\left(u\frac{\partial v}{\partial x} + v\frac{\partial v}{\partial y}\right) - \frac{\Delta t^3}{6}\left(u\frac{\partial}{\partial x}\left(u\frac{\partial v}{\partial x} + v\frac{\partial v}{\partial y}\right) + v\frac{\partial}{\partial y}\left(u\frac{\partial v}{\partial x} + v\frac{\partial v}{\partial y}\right)\right).$$

Third-order time accuracy is maintained, provided that the velocities u and v are evaluated at time t+Δt/2. These are obtained by a three time-level extrapolation (using a 3 point Lagrange formula) from velocities at times t-2Δt, t-Δt and t as suggested by Temperton and Staniforth (1987) and shown below for u.

$$u^{t+\Delta t/2} = \frac{3}{8}u^{t-2\Delta t} - \frac{5}{4}u^{t-\Delta t} + \frac{15}{8}u^{t}.$$

To use the velocities at t+Δt/2 in the X and Y expressions, they are firstly interpolated to the $T_{i,j}$ spatial position using a 4 point Lagrange interpolation as follows:

$$u_{T_{i,j}} = -\frac{1}{16}u_{i-2,j} + \frac{9}{16}u_{i-1,j} + \frac{9}{16}u_{i,j} - \frac{1}{16}u_{i+1,j},$$

and similarly for $v_{T_{l,j}}$.

Once the departure positions (X, Y) are found, TX^t_*, $PSLX^t_*$ and q^t_* are evaluated at those points using a 4 point Lagrange interpolation formula, first interpolated in the x-direction then in the y-direction as shown below for TX. In the x-direction the grid points can be represented as follows:

$$\dot{x}_{l\,d-1} \qquad \dot{x}_{l\,d} \qquad \dot{X} \qquad \dot{x}_{l\,d+1} \qquad \dot{x}_{l\,d+2} \quad , \text{ where } X = (id+x_d)\Delta x.$$

Therefore,

$$TX(id+x_d, j) = -\frac{x_d(x_d-1)(x_d-2)}{6} TX_{l\,d-1,\,j} + \frac{(x_d^2-1)(x_d-2)}{2} TX_{id,j}$$

$$-\frac{x_d(x_d+1)(x_d-2)}{2} TX_{id+1,\,j} + \frac{x_d(x_d^2-1)}{6} TX_{id+2,j}$$

for each j value, and then finally

$$TX(id+x_d, jd+y_d) = -\frac{y_d(y_d-1)(y_d-2)}{6} TX_{l\,d+x_d,\,jd-1} + \frac{(y_d^2-1)(y_d-2)}{2} TX_{id+x_d,jd}$$

$$-\frac{y_d(y_d+1)(y_d-2)}{2} TX_{l\,d+x_d,\,jd+1} + \frac{y_d(y_d^2-1)}{6} TX_{id+x_d,jd+2},$$

which is TX at the point (X, Y).

The (X, Y) are then interpolated to the (u, v) - grid and UX^t_* and VX^t_* are evaluated in the same manner as TX.

2.2.4 Vertical diffusion

The vertical diffusion term is solved implicitly with respect to time at the beginning of each full time step and is illustrated below for u. The equation is

$$\frac{\partial u}{\partial t} = -\frac{g}{p_s}\frac{\partial \tau_{zx}}{\partial \sigma}$$

$$= -\frac{g}{p_s}\frac{\partial}{\partial \sigma}\left\{\rho K_m \frac{\partial u}{\partial z}\right\} \qquad \text{(see Section 2.3)}$$

$$= -\frac{g}{p_s}\frac{\partial}{\partial \sigma}\left\{\frac{p}{RT} K_m \frac{\partial u}{\partial z}\right\}$$

$$= \frac{\partial}{\partial \sigma}\left\{-\frac{g\sigma}{RT} K_m \frac{\partial u}{\partial z}\right\}$$

$$= \frac{\partial}{\partial \sigma}\left\{\frac{\partial \sigma}{\partial z} K_m \frac{\partial u}{\partial z}\right\}, \text{ using equation (2.1.3).}$$

In finite difference form the equation becomes

$$\frac{u_k^{t+\Delta t} - u_k^t}{\Delta t} = \frac{\left\{\frac{\Delta \sigma}{\Delta z} K_m \frac{\Delta u}{\Delta z}\right\}_{k+1/2}^{t+\Delta t} - \left\{\frac{\Delta \sigma}{\Delta z} K_m \frac{\Delta u}{\Delta z}\right\}_{k-1/2}^{t+\Delta t}}{(\sigma_{k+1/2} - \sigma_{k-1/2})}$$

for k=2,...,kl-1. Further manipulation gives

$$\frac{u_k^{t+\Delta t} - u_k^t}{\Delta t} = \frac{\left\{\frac{\Delta \sigma}{(\Delta z)^2} K_m\right\}_{k+1/2} (u_{k+1}^{t+\Delta t} - u_k^{t+\Delta t}) - \left\{\frac{\Delta \sigma}{(\Delta z)^2} K_m\right\}_{k-1/2} (u_k^{t+\Delta t} - u_{k-1}^{t+\Delta t})}{(\sigma_{k+1/2} - \sigma_{k-1/2})}$$

Rearranging gives

$$A_k u_{k-1}^{t+\Delta t} + B_k u_k^{t+\Delta t} + C_k u_{k+1}^{t+\Delta t} = D_k$$

where $A_k = \dfrac{\Delta t}{\Delta\sigma_k} \left(- \dfrac{\Delta\sigma}{(\Delta z)^2} K_m \right)_{k-1/2}$,

$$C_k = \frac{\Delta t}{\Delta\sigma_k} \left(- \frac{\Delta\sigma}{(\Delta z)^2} K_m \right)_{k+1/2},$$

$$B_k = 1 - A_k - C_k ,$$

and $D_k = u_k^t$ for k=2,...,kl-1.

For k = 1, the surface stress is used instead of an exchange coefficient formulation (see Section 2.3).

$$\frac{u_1^{t+\Delta t} - u_1^t}{\Delta t} = \frac{\left\{ \dfrac{\Delta\sigma}{(\Delta z)^2} K_m \right\}_{1+1/2} (u_2 - u_1)^{t+\Delta t} + \dfrac{g}{RT_s} C_d |V_{-1}| \, u_1^{t+\Delta t}}{(\sigma_{1+1/2} - \sigma_{surf})}$$

where $u_0 = 0$.
Rearranging gives

$$A_1 u_0^{t+\Delta t} + B_1 u_1^{t+\Delta t} + C_1 u_2^{t+\Delta t} = D_1$$

where $A_1 = \dfrac{\Delta t}{\Delta\sigma_1} \dfrac{g}{RT_s} C_d |\underline{v}_{-1}|$,

$$C_1 = \frac{\Delta t}{\Delta\sigma_1} \left(- \frac{\Delta\sigma}{(\Delta z)^2} K_m \right)_{1+1/2},$$

$$B_1 = 1 - A_1 - C_1 ,$$

and $$D_1 = u_1^t .$$

For temperature the method is the same but since T_0 is not zero the term $A_1 T_0$ is moved to the right hand side of the equation and added into D_1.

At k= kl, $\tau_{zx} = 0$ and the equation at k=kl for u becomes

$$\frac{u_{kl}^{t+\Delta t} - u_{kl}^{t}}{\Delta t} = \frac{-\left\{ \frac{\Delta\sigma}{\Delta z} K_m \frac{\partial u}{\partial z} \right\}_{kl-1/2}^{t+\Delta t}}{(\sigma_{kl+1/2} - \sigma_{kl-1/2})} ,$$

$$\frac{u_{kl}^{t+\Delta t} - u_{kl}^{t}}{\Delta t} = \frac{-\left\{ \frac{\Delta\sigma}{(\Delta z)^2} K_m \right\}_{kl-1/2} (u_{kl} - u_{kl-1})^{t+\Delta t}}{(\sigma_{kl+1/2} - \sigma_{kl-1/2})} .$$

Rearranging gives

$$A_{kl} u_{kl-1}^{t+\Delta t} + B_{kl} u_{kl}^{t+\Delta t} = D_{kl}$$

where $$A_{kl} = \frac{\Delta t}{\Delta\sigma_{kl}} \left(- \frac{\Delta\sigma}{(\Delta z)^2} K_m \right)_{kl-1/2} ,$$

$$B_{kl} = 1 - A_{kl} ,$$

and $$D_{kl} = u_{kl}^t .$$

This system is solved using the Thomas algorithm for a tridiagonal system.

The equations are $A_k u_{k-1}^{t+\Delta t} + B_k u_k^{t+\Delta t} + C_k u_{k+1}^{t+\Delta t} = D_k$ for $1 \le k \le kl$

with $A_1 = C_{kl} = 0$. The solution is

$$u_{kl} = \gamma_{kl} \quad \text{and} \quad u_k = \gamma_k - \frac{C_k u_{k+1}}{\beta_k} ,$$

$$\text{where} \quad \beta_k = B_k - \frac{A_k C_{k-1}}{\beta_{k-1}} \quad \text{and} \quad \beta_1 = B_1 ,$$

$$\gamma_k = \frac{D_k - A_k \gamma_{k-1}}{\beta_k} \quad \text{and} \quad \gamma_1 = \frac{D_1}{B_1} .$$

2.2.5 Horizontal diffusion

The horizontal diffusion terms are evaluated at the end of each small time step using a deformation type formulation (Kikuchi *et al.*, 1981) as follows. In finite-difference form,

$$\frac{\partial u}{\partial t} = \frac{\partial}{\partial x} K_m^H \frac{\partial u}{\partial x} + \frac{\partial}{\partial y} K_m^H \frac{\partial u}{\partial y} \quad \text{becomes}$$

$$u^{t+\Delta t''} - u^{t+\Delta t'} = \frac{\Delta t}{\alpha} \left\{ \frac{\partial}{\partial x} K_m^H \frac{\partial u}{\partial x} + \frac{\partial}{\partial y} K_m^H \frac{\partial u}{\partial y} \right\}^{t+\Delta t'}$$

where $\Delta t''$, $\Delta t'$ are given by eq. (2.2.7),

$$K_m^H = a^2 \Delta x \Delta y \left[\frac{1}{2} \left\{ \frac{\partial v}{\partial x} + \frac{\partial u}{\partial y} \right\}^2 + \left\{ \frac{\partial u}{\partial x} \right\}^2 + \left\{ \frac{\partial v}{\partial y} \right\}^2 \right]^{1/2} ,$$

and a is an adjustable coefficient. The horizontal derivatives are calculated by centered differencing.

2.3 Boundary-layer parameterization

The momentum (τ), heat (H) and evaporation fluxes (E) in the above equations are parameterised by K-theory. In the surface layer, the flux-profile relationships are specified in terms of numerically-fitted

functions of bulk Richardson number Ri_B following Louis (1979). An advantage of this approach is that analytical derivatives may be taken with respect to Richardson number, a feature which is important in allowing subsequent efficient iterative solution of the surface heat balance equation. The surface stress $\underset{-0}{\tau}$, sensible heat flux H_0, and latent heat flux E_0 are written as:

$$\underset{-0}{\tau} = - \rho_1 C_d \, |\underset{-1}{V}| \, \underset{-1}{V} \tag{2.3.1a}$$

$$H_0 = \rho_1 c_p C_h \, |\underset{-1}{V}| \, (\theta_0 - \theta_1) \tag{2.3.1b}$$

$$E_0 = \rho_1 C_w C_e L \, |\underset{-1}{V}| \, (q_{sat}(T_0) - q_1), \tag{2.3.1c}$$

where the subscripts 0 and 1 denote the surface and first model level respectively.

The transfer coefficients C_d, C_h and C_e are given by

$$C_d = a^2 F_m(z_1/z_0, Ri_B) \tag{2.3.2a}$$

$$C_h = C_e = (a^2/0.74) F_h(z_1/z_0, Ri_B), \tag{2.3.2b}$$

where $a^2 = k^2/(\ln(z_1/z_0))^2$ is the transfer coefficient for neutral conditions. The bulk Richardson number is $Ri_B = gz_1(\theta_1 - \theta_0)/(\theta_1 \, |V_1|^2)$. C_w is a soil moisture availability parameter defined as the ratio of the actual evaporation rate to the potential evaporation rate. Equation (2.3.1c) can be written equivalently as

$$E_0 = \rho_1 C_e L \, |\underset{-1}{V}| \, (q_0 - q_1),$$

where the surface specific humidity is calculated from the expression

$$q_0 = C_w q_{sat}(T_0) + (1 - C_w) q_1.$$

F_m and F_h are the functions of Ri_B (for momentum and heat respectively) incorporating the flux-profile relationships.

In **stable** conditions

$$F_m = F_h = 1/(1 + 4.7 Ri_B)^2 \tag{2.3.3a}$$

and in **unstable** conditions

$$F_m = F_h = 1-(9.4Ri_B)/(1+c|Ri_B|^{1/2}), \qquad (2.3.3b)$$

where for F_m, $c = 69.56a^2(z/z_0)^{1/2}$ and for F_h, $c = 49.82a^2(z/z_0)^{1/2}$.

Above the surface layer, the turbulent fluxes are formulated in terms of a gradient diffusion approach. For example, the u-momentum flux in (x,y,σ) coordinates is

$$\tau_{\sigma x} = (\rho^2 g/p_s)K_m \partial u/\partial\sigma$$

where the vertical momentum exchange coefficient K_m depends on height, shear and stability.

$$K_m = l^2 \left|\partial \underline{V} /\partial z\right| F_m(Ri_B).$$

In **unstable** conditions ($Ri_B < 0.0$), F_m and F_h are essentially the same functions as for the surface layer, with Ri_B now defined as $g(\partial\theta_v/\partial z)/(\theta_v(\partial \underline{V}/\partial z)^2)$. The coefficient c in (2.3.3b) now becomes

$$c = 9.4C^* l^2[(z+\Delta z/z)^{1/3}-1]^{3/2}/(z^{1/2}\Delta z^{3/2})$$

with $C^* = 7.4$ for F_m and $C^* = 5.3$ for F_h. The mixing length l is given by Blackadar's (1962) formula $l = k\lambda z/(\lambda + kz)$ where λ is the asymptotic mixing length, which is assigned a value of 100 m.

In **stable** conditions ($Ri_B \geq 0.0$), F_m ($= F_h$) varies linearly between 0.0 and 1.0 according to the following formulae:

$$F_m = (Ri_{cr} - Ri_B)/Ri_{cr} \qquad \text{for } Ri_B \leq Ri_{cr}$$
$$F_m = 0.0 \qquad \text{for } Ri_B > Ri_{cr}.$$

The following expression is used for the critical Richardson number

$$Ri_{cr} = 0.067\ (100\ \Delta z)^{0.25}$$

where Δz is in metres. In this way, Ri_{cr} is a function of the grid spacing and, in the near-surface regions where the grid resolution is fine (Δz = 2 m), approaches the theoretical value for turbulence cut-off of 0.25. Towards the top of the model where the spacing is about 800 m, Ri_{cr} approaches a value of 1.1.

The height of the convective boundary layer z_i, needed for the

dispersion model, is computed from a prognostic equation developed by Deardorff (1974) from laboratory and numerical experiments.

$$\frac{\partial z_i}{\partial t} = -\underline{V}.\nabla z_i + w_i + 1.8(w_* + 1.1u_* - 3.3u_* |f|z_i)/\{(gz_i/\theta_s)\partial\theta^+/\partial z + 9w_* + 7.2u_*\} \quad (2.3.4)$$

where w_i is vertical velocity at z_i, w_* is the mixed-layer convective velocity scale, u_* is friction velocity, f is the Coriolis parameter, g is gravitational acceleration, θ_s is surface-layer potential temperature and $\partial\theta^+/\partial z$ is stability immediately above z_i.

A modified version of this equation is used here to allow a better representation of the thermal internal boundary layer associated with the sea breeze (Physick et al., 1989). In this scheme, the first (advection) term is omitted from Equation (2.3.4) and the stability of each layer in a column is checked every timestep, from the ground upwards, to find the first layer with a lapse rate greater than a critical value. If such a layer exists within the current mixed layer, z_i is reduced to the top of that layer. However, the mixed layer is allowed to grow according to Equation (2.3.4) (minus advection) if no such layer is found. The critical stability value is set to 1K km^{-1}, following Anthes (1978) who used such a criterion to define the mixed- layer top in a sea-breeze model.

2.4 Radiation parameterization

Short-wave radiation at the ground is specified as a function of solar zenith angle, latitude and day of the year, using standard astronomical formulae. Terrain slope and orientation are also taken into account. Heating of the atmosphere by water vapour absorption of short-wave radiation is implemented following Atwater and Brown (1974). Outgoing long- wave radiation from the ground is specified as σT^4, where σ is the Stefan-Boltzmann constant and T is surface temperature. The heating and cooling of the atmosphere due to long-wave radiative flux divergence is computed from broadband emissivities for water vapour and carbon dioxide. A detailed description of the radiation parameterization can be found in Mahrer and Pielke (1977). A water vapour - carbon dioxide overlap band has also been added in the LADM code, and incoming long-wave radiation at the model top (19700 m) is set to zero, rather than σT_{top}^4. Both changes have improved the long-wave cooling

predictions of the model.

2.5 Boundary conditions

Surface

At the ground (σ = 1), horizontal wind speed is zero, as is $\dot{\sigma}$ the vertical velocity in the (x,y,σ) coordinate system. Sea-surface temperature is kept constant, while at land gridpoints temperature is calculated at each timestep by an iterative solution of the surface energy balance equation. This involves the radiative, sensible heat and evaporative fluxes (all described previously), and the heat flux to or from the soil. The latter is obtained by computing temperature T using a heat conduction equation

$$\partial T/\partial t = K_s \partial^2 T/\partial z^2$$

at 6 levels in the soil, located at 1, 3, 7, 15, 31, and 63 cm below the surface. Values must be specified for soil density (ρ_s), diffusivity (K_s) and specific heat (c_s), and for the soil temperature at 63 cm, which is assumed to be constant over the integration period. The soil heat flux at the surface is calculated from

$$F_{soil} = \rho_s c_s K_s (T_0 - T_{-1})$$

where T_0 = surface temperature and T_{-1} = temperature at the first level in the soil.

A roughness length z_0 is specified over land while over water surfaces z_0 is dependent on wind speed through the Charnock (1955) formula

$$z_0 = 0.018 u_*^2/g.$$

Surface specific humidity q_0, though not used explicitly in the model, can be derived from the moisture availability parameter C_w via the expression $q_0 = C_w q_{sat}(T_0) + (1-C_w)q_1$ where q_1 is the humidity at the first model level (about 2 m).

Upper

Increased horizontal diffusion, extending over 5 levels from about 8500 m to the model top at about 19700 m, is employed to prevent the reflection of upward-propagating waves from the top of the model (Durran and Klemp, 1983).

Lateral

For the outer grid, zero-gradient boundary conditions, normal to the boundary, are used for horizontal velocity, surface pressure, and temperature. A buffer zone, in which the terrain gradient normal to each boundary is set to zero, is used between the region of interest and the domain boundaries. For example, we have found that an extra 10 gridpoints on all sides of a 50 x 50 gridpoint area of interest, producing a 70 x 70 domain, is sufficient to prevent boundary-generated noise from affecting the central region, even by the end of a 60 hour simulation.

Near the boundaries of nested grids, a blending of the boundary value from the coarse-grid run and the predicted value from the fine-mesh run is used for the five outermost gridpoints (see Davies 1976). The weighting towards the coarse-grid value decreases markedly with distance from the boundary.

2.6 Initial data requirements

Input data for the model includes elevation of the terrain above sea level and the surface characteristics discussed in the previous Sections (roughness length, albedo, surface moisture availability, soil characteristics, etc.). Also needed are surface pressure at the lowest elevation in the domain and vertical profiles of wind and temperature. The latter is usually obtained from a radiosonde profile and should be representative of the region. All columns in the domain are set to this profile. The wind profile must reflect the synoptic-scale pressure gradients and is obtained from mean sea-level pressure charts and geopotential height charts at 850 hPa, 700 hPa, 500 hPa etc. Rawinsonde data can also be of use, but do contain mesoscale effects. The wind profile is also applied at all grid columns. As the wind and temperature data are given as a function of height above sea level, and the sigma surfaces are terrain following, it is necessary to carry out an interpolation process to produce initial fields. Surface pressure at each gridpoint is obtained via the hydrostatic equation and interpolation using the temperature profile. Note that if there is no terrain, the horizontal gradients of surface pressure, temperature, and geopotential are initially zero, as the equations are written in terms of the mesoscale components of these variables (see Appendix A).

The model run usually begins at midnight to allow the wind to adjust to the terrain and to allow time for drainage flows to develop before diurnal heating begins at sunrise. It is also advisable to run the model for 48 hours and compare predictions to observations during the second 24 hours, thus allowing time for the formation of mesoscale pressure gradients from the diurnal heating of the previous day.

3. THE ATMOSPHERIC DISPERSION MODEL

3.1 Overview and model equations

A popular approach to investigating pollution dispersion has been solution of the advection-diffusion equation by numerical difference schemes on a mesoscale grid in a similar manner to the meteorological model described previously. However, it is not possible to reduce the grid spacing to such a size that concentration gradients from point sources are represented accurately. In addition, the numerical diffusion inherent in many advection schemes, and the application of gradient transfer theory to plumes whose scale is small compared to the dominant turbulence scales, add further to the limitations of this approach.

A Lagrangian scheme in which individual particles are transported and diffused according to wind and turbulence fields provided by the mesoscale model overcomes these disadvantages. The relevant fields are supplied on a three-dimensional grid every 10 minutes, although this time interval is variable. Particles, which are assumed to be inert and neutrally buoyant, can be released at any rate from any number of locations in the horizontal and vertical and are moved with a timestep of typically 20 seconds. The wind and turbulence fields remain constant over the 10-minute period.

The location of a particle at time $t + dt$ is determined from the following equations.

$$x_i(t+dt) = x_i(t) + [\bar{u}_i(t) + u_i''(t)]\, dt \qquad (i = 1,2,3) \qquad (3.1.1)$$

where $(x_1, x_2, x_3) = (x, y, z^*)$ are the coordinates in a terrain-following coordinate system, and

$$(\bar{u}_1, \bar{u}_2, \bar{u}_3) = (u, v, w^*)$$

are the velocity components supplied by the mesoscale model, bilinearly interpolated to the particle location. The terrain-following coordinate system is related to a Cartesian (x, y, z) system via the transformation

$$z^* = H(z-z_G)/(H-z_G)$$

where H is the model top, z is height above sea level, and z_G is terrain elevation. Prior to being written to a file during a mesoscale model run, the velocity and turbulence fields (see Section 3.6) are linearly interpolated from the model's (x, y, σ) coordinate system to the (x, y, z^*) system of the particle model. The z-levels chosen are those approximating the initial heights of the σ-levels over the sea. The turbulent velocity fluctuations in equation (3.1.1),

$$(u_1'', u_2'', u_3'') = (u'', v'', w^{*''}),$$

are obtained from the Langevin equation in the following manner.

The general form of the Langevin equation for u_i'', derived by Thomson (1987), can be written as

$$du_i'' = a_i\, dt + (C_0\varepsilon)^{1/2} dW_i \,. \qquad (3.1.2)$$

This form is capable of representing inhomogeneous, non-stationary turbulence and, with an appropriate choice of a_i, satisfies the criterion that a well-mixed profile of particles will remain well mixed with time. In equation (3.1.2), a_i is an acceleration, du_i'' is the change in turbulent velocity over the time interval dt, ε is the rate of dissipation of turbulent kinetic energy, C_0 is a universal constant, and dW_i is a random variable which has a Gaussian distribution (mean 0, variance dt). The finite-difference form of equation (3.1.2) is

$$u_i''(t+\Delta t) = u_i''(t) + a_i\Delta t + (C_0\varepsilon)^{1/2} r_i \Delta t \qquad (3.1.3)$$

where r_i is a random variable with a Gaussian distribution (mean 0, standard deviation 1) and Δt is the timestep.

An expression for a_i is obtained by solving the following form of the Fokker-Planck equation (Thomson, 1987),

$$\frac{\partial a_i P_E}{\partial u_i''} = -\frac{\partial u_i'' P_E}{\partial x_i} + \frac{1}{2} C_0 \varepsilon \frac{\partial^2 P_E}{\partial u_i''^2} - \frac{\partial P_E}{\partial t} \qquad (3.1.4)$$

subject to the boundary condition $a_i P_E \Rightarrow 0$ as $|u_i''| \Rightarrow \infty$ (Sawford, CSIRO, personal communication, 1989). P_E is the Probability Density Function (PDF) representing the turbulence.

In Sections 3.2 and 3.3, we present expressions for a_i, T_{L,u_i}, and σ_{u_i} in convective and stable conditions.

3.2 Diffusion formulation in convective conditions

3.2.1 Vertical turbulent component

In our model formulation, we assume the turbulence is stationary and homogeneous, thus enabling a considerably larger timestep dt to be used than is required for the modelling of inhomogeneous turbulence. Results from experiments justifying our assumption of homogeneity can be found in Section 4.2 and in Hurley and Physick (1991, 1993). We also assume independence of the three components so that (3.1.4) separates into individual equations for each component.

The solution of equation (3.1.4) for the vertical component of a_i under homogeneous turbulence conditions is

$$a_w = \frac{1}{2} C_0 \varepsilon \frac{1}{P_E} \frac{\partial P_E}{\partial w''} \qquad (3.2.1)$$

A skewed PDF made up of two Gaussian functions, one representing the updrafts (+) and the other representing the downdrafts (-) of the convective boundary layer, is used to represent the turbulence as follows;

$$P_E = pN(m_+,\sigma_+) + (1-p)N(m_-,\sigma_-)$$

with

$$N(m, \sigma) = \sigma^{-1}(2\pi)^{-0.5}\exp(-(w''-m)^2/2\sigma^2).$$

Here p is the probability of a particle being in an updraft, m_+ is the mean velocity in an updraft and σ_+ is the velocity standard deviation in an updraft, and similarly for the downdraft terms. Upon substitution for P_E into (3.2.1), an expression for a_w can be obtained :

$$a_w = -\frac{1}{2} C_0 \varepsilon \left(\frac{pN(m_+,\sigma_+)(w''-m_+)/\sigma_+^2 + (1-p)N(m_-,\sigma_-)(w''-m_-)/\sigma_-^2}{pN(m_+,\sigma_+) + (1-p)N(m_-,\sigma_-)} \right).$$

The first three moments of P_E are equated to the first three moments of the vertical velocity distribution $\overline{w''} = 0$, $\overline{w''^2} = \sigma_w^2$, and $\overline{w''^3} = S_w^3$. Then the equations can be solved for the variables p, m_+, and m_- (by making the assumption $\sigma = |m|$ for both updrafts and downdrafts). The solutions are :

$$p = 0.5[1-(Sk^2/(8+Sk^2))^{0.5}] \quad (3.2.2a)$$

$$m_+^2 = 0.5\sigma_w^2(1-p)/p \quad (3.2.2b)$$

$$m_- = -m_+ p/(1-p), \quad (3.2.2c)$$

where $Sk = (S_w/\sigma_w)^3$ is the degree of skewness of the turbulence (see next Section).

a. Turbulence formulation

According to Thomson (1987), C_0 should be in the range 2.0-4.0. We choose a value of 2.0, in agreement with the value used by Luhar and Britter (1989) when simulating the Willis and Deardorff convective dispersion experiments. The homogeneous turbulence parameterisations used are

$$\sigma_w = 0.6w_*$$

$$\varepsilon = 0.6w_*^3/z_i ,$$

where w_* is the convective velocity scale and z_i is the mixed layer height. These agree with observations in the middle 80% of the convective boundary layer, and result in a Lagrangian timescale (with $C_0 = 2.0$) of

$$T_{L,w} = 0.6z_i/w_* .$$

The value of skewness used

$$Sk = (S_w/\sigma_w)^3 = 0.4$$

enables a good comparison to be made with maximum concentrations from laboratory experiments and is consistent with field and laboratory measurements in the bulk of the mixed layer. Further discussion can be found in Hurley and Physick (1993).

3.2.2 Horizontal turbulent components

Equations (3.1.3 and 3.2.1) are also used to calculate the horizontal fluctuations, with w'' replaced by u'' and v''. However we assume Gaussian (non-skewed) turbulence for these components, using the following PDF:

$$P_E = N(0,\sigma_u) = \sigma_u^{-1}(2\pi)^{-0.5}\exp(-u''^2/2\sigma_u^2)).$$

Substitution of P_E into equation (3.2.1) leads to

$$a_u = -\frac{C_0\varepsilon}{2\sigma_u^2}u'' \qquad (3.2.4)$$

a. Turbulence formulation

The homogeneous turbulence parameterisations used in equations (3.1.3) and (3.2.4) are the same as for w'',

$$\sigma_u = \sigma_v = 0.6w_* ,$$

$$\varepsilon = 0.6w_*^3/z_i .$$

3.2.3 Boundary conditions

Inhomogeneous models usually use perfect reflection boundary conditions, both at the ground and at the top of the mixed layer, where both the velocity perturbation and the remaining distance of travel are reflected. However, use of these conditions in our skewed homogeneous model resulted in accumulation of particles near the ground (a non-dimensional crosswind integrated concentration C^y of approximately 1.3) and a deficit of particles near the top of the mixed layer (C^y slightly less than 1.0), at relatively large distances from the source. This effect was due to the inconsistency between the velocity statistics and the Gaussian-type boundary condition. The correct boundary condition is one which is consistent with the probability distribution for w''. The boundary condition used is one of skewed memory reflection, where w'' is scaled by the absolute value of the ratio of the mean updraft velocity to the mean downdraft velocity when reflecting at the ground, and the inverse of this ratio at the mixing height.

This approach predicts well-mixed conditions (C^y=1) to within 10% for large distances downwind, while not affecting maximum values of concentration

near the source. The 10% error in the profiles was due to the fact that to match the probability distribution properly, the random and non-random components need to be separated and only the non-random component of the memory reflected in the above skewed manner. As this approach was considered too complex, the above approximation was made, giving C^y=1 everywhere except at approximately z/z_i= 0.2 (C^y=0.9) and z/z_i=0.7-0.8 (C^y=1.05).

3.3 Diffusion formulation in stable conditions

The turbulence in stable conditions is discussed here in terms of a Lagrangian timescale T_{L,u_i}, instead of ε. These quantities are related by the expression

$$T_{L,u_i} = 2\sigma_{u_i}^2 /(C_0\varepsilon).$$

In stable conditions, we follow the turbulence formulations used by McNider (1981) (see also McNider *et al.*, 1988).

3.3.1 Vertical turbulent component

Under the assumption of Gaussian turbulence, the PDF is written as

$$P_E = N(0,\sigma_w) = \sigma_w^{-1}(2\pi)^{-0.5}\exp(-w''^2/2\sigma_w^2)).$$

With the additional assumption of inhomogeneous turbulence, the solution of equation (3.1.4) is

$$a_w = -\frac{C_0\varepsilon}{2\sigma_w^2} w + \sigma_w \frac{\partial\sigma_w}{\partial z}\left\{1 + \left(\frac{w''}{\sigma_w}\right)^2\right\}. \qquad (3.3.1)$$

a. Turbulence formulation

The formulation for σ_w,

$$\sigma_w = 1.2l^2\left[\frac{Ri_{cr} - Ri}{Ri_{cr}}\right]^{0.58}\left|\frac{dV}{dz}\right| \qquad \text{for } Ri < Ri_{cr}$$

$$= .01 \text{ m s}^{-1} \qquad \text{for } Ri \geq Ri_{cr}$$

is based on the work of Blackadar (1979) and expresses σ_w in terms of the

gradient Richardson number Ri, mixing length l, and windshear dV/dz (all obtained from the mesoscale windfield model). The critical Richardson number Ri_{cr} is written as a function of vertical grid spacing in the same way as for the windfield model (see Section 2.3).

The relation between Eulerian and Lagrangian timescales (Pasquill, 1974) is used to calculate $T_{L,w}$.

$$T_{L,w} = \beta T_{E,w}$$

where

$$\beta = \min\ (5.,\ 0.6\ (\bar{u}^2 + \bar{v}^2)^{0.5} / \sigma_w)$$

and

$$T_{E,w} = 0.2\ \lambda_{m,w} / (\bar{u}^2 + \bar{v}^2)^{0.5}$$

with

$$\lambda_{m,w} = \min\ (203m,\ z).$$

3.3.2 Horizontal turbulent components

Gaussian homogeneous turbulence is assumed, as for the horizontal components under convective conditions, and a_u takes the form of equation (3.2.4).

a. Turbulence formulation

The formulations for σ_u and σ_v are based on the field work of Panofsky *et al.* (1977),

$$\sigma_u = \sigma_v = 2.3\ u_* .$$

Similar relations for $T_{L,u}$ and $T_{L,v}$ apply as for the vertical components:

$$T_{L,u} = T_{L,v} = \beta T_{E,u}$$

where

$$\beta = \min\ (5.,\ 0.6\ (\bar{u}^2 + \bar{v}^2)^{0.5} / \sigma_u)$$

and

$$T_{E,u} = 0.2\ \lambda_{m,u} / (\bar{u}^2 + \bar{v}^2)^{0.5}$$

with

$$\lambda_{m,u} = 0.7 z_i (z/z_i)^{0.5} .$$

3.3.3 Boundary conditions

The only boundary condition employed in stable conditions is at the ground where perfect reflection of a particle's velocity and position is assumed to occur.

3.4 Plume-rise equations

The height at which particles are released throughout the simulation period is determined from the equations governing the rise of a bent-over plume (Briggs, 1975). We assume adiabatic motion for the plume, with the gas cooling only due to expansion as it rises. This form of buoyancy conservation leads to the following equation,

$$dF/dt = -s(M/M_{eff})wV \tag{3.4.1}$$

where F = buoyancy flux, s = stability parameter $((g/\theta_a)\partial\theta_a/\partial z)$, w = vertical velocity, V = Ur^2 = volume flux, M/M_{eff} = ratio of actual to effective vertical momentum flux = 0.444, g = gravitational acceleration, θ_a = ambient potential temperature, U = horizontal windspeed and r = plume radius.

Conservation of momentum is expressed as follows:

$$dM/dt = F \tag{3.4.2}$$

where M = wV is the flux of vertical momentum. Using the closure assumption that the radius of the plume increases linearly with height ($r = \beta z$, where β = 0.6 is recommended for bent-over plumes), the following equation for height above the virtual origin can be derived (Briggs, 1975):

$$dz^3/dt = 3wV/(U\beta^2) \; . \tag{3.4.3}$$

Initial conditions for equations (3.4.1) - (3.4.3) at the stack top are:

i. For buoyancy flux (F)

$$\begin{aligned} F_0 &= g(T_0 - T_a)V_0/T_0 \\ &= g(T_0 - T_a)w_0 r_s^2/T_0 \; . \end{aligned} \tag{3.4.4}$$

ii. For momentum flux (M)

$$\begin{aligned} M_0 &= (T_a/T_0)w_0 V_0 \\ &= (T_a/T_0)w_0^2 r_s^2 \; , \end{aligned} \tag{3.4.5}$$

where T_a = ambient temperature (K), T_0 = plume temperature (K), w_0 = plume exit velocity, and r_s = stack radius.

iii. For plume height (z)

At stack top, the plume radius is non-zero, so that z_0 the distance of the plume virtual origin below stack top is obtained from

$$z_0 = \beta r_0 \tag{3.4.6}$$

where the initial radius r_0 is obtained by equating the actual source mass flux to the flux at t=0 under the bent-over plume assumption,

$$r_0 = r_s (T_a w_0 / T_0 U)^{1/2} \tag{3.4.7}$$

Equations (3.4.1-3.4.3) are solved by the Runge-Kutta method with a timestep of one second.

Final plume rise height (or effective stack height) under convective conditions (when the mixed-layer height z_i is greater than the stack height z_s) is defined as the lower height of (a) the height at which the dissipation rate of the plume's turbulent kinetic energy (ε_p) has decreased to that of the atmosphere (ε_a), and (b) the height at which the plume buoyancy is equal to five percent of its initial value.

Here

$$\varepsilon_p = 1.5 w^3 / z \tag{3.4.8}$$

and

$$\varepsilon_a = 0.6 w_*^3 / z_i \tag{3.4.9}$$

The convective scaling velocity w_* is defined as

$$w_* = u_* (z_i / (-kL))^{1/3}$$

with u_* = friction velocity and L = Monin - Obukhov length. In stable conditions, final rise height is defined as the height at which the buoyancy flux F becomes five percent of its initial value. A downwind distance for particle release is calculated by advecting particles with the wind at each level as they rise to the effective stack height.

3.4.1 Plume-rise enhancement

For sources with more than one stack, the effective number of stacks, NE, depends on the source buoyancy flux and the stack spacing, as well as wind direction relative to stack orientation. A methodology developed by Briggs (1984) for calculating NE is discussed and applied to Latrobe Valley power stations by Manins (1987). Values of NE for ECNSW power stations have been calculated and are shown in Table 3.1 of Section 3.6. No dependence on wind direction has been used, following the data analysis of Briggs (1984) and the findings for the Latrobe Valley, although wind tunnel studies do show a strong dependence (Overcamp and Ku, 1980). The NE values in Table 3.1 are used to increase the initial plume buoyancy F_0 calculated from equation (3.4.4).

3.5 Computation of surface concentrations

Ground-level concentrations (*glcs*) are calculated at any time by dividing the region into square boxes Δz high and counting the number of particles in each box. In Appendix B, we discuss the results of numerical experiments investigating the dependence of hourly-averaged *glcs* on the number of particles and the size of the sampling boxes. At distances further than about 5 km from the source, we have found that a value of 1000 m is sufficiently small for the horizontal dimensions Δx and Δy of the sampling volume. A value of 25 m is chosen for the depth Δz. Concentrations are averaged over one hour, although sometimes during the morning fumigation period half-hourly averages are computed.

During convective conditions, the maximum concentration is found near the source. Convective scaling theory estimates this distance to be in the vicinity of

$$x_{max} = 2Uz_e/w_* , \qquad (3.5.1)$$

where z_e is the effective stack height, w_* is the convective scaling velocity and U is the mean wind speed between the ground and z_e. Substitution of realistic parameter values in equation (3.5.1) shows that x_{max} is expected to be less than 5 km. In order that modelled concentrations are not underestimated in this near-stack region, it is necessary to choose a smaller value for Δx and Δy than the 1000 m used at larger distances. From

experiments in which the sampling box sides were systematically reduced, we found that a value of 250 m is sufficiently small to avoid any underestimation (see Appendix B). In our modelling studies, the dispersion (particle) component is run twice; once with a small sampling box size and a small near-stack domain and once with the larger box size and larger domain to examine medium to long-range dispersion of material.

We determine the number of particles to be released each timestep Δt in the following manner. If the emission rate of a pollutant is Q g s^{-1} and the release rate of particles is N s^{-1}, then the pseudo mass of each particle is Q/N g. Thus one particle in the sampling volume represents a concentration of

$$C = Q/(N\Delta x\Delta y\Delta z). \qquad (3.5.2)$$

If we desire the accuracy of predicted ground-level concentrations to be greater than e, then C must be less than e. This relation is used to calculate N as follows.

$$N = Q/(e\Delta x\Delta y\Delta z). \qquad (3.5.3)$$

For the Hunter Valley study of Chapter 4 in which maximum concentrations of about 350 μg m^{-3} are predicted, we have specified a value of 20 μg m^{-3} for e. As calculated from equation (3.5.3), the value of N, in particles per second, is 5.6 when $\Delta x = \Delta y = 1000$ m, and 89.6 when the size is 250 m. In practice, we release $N\Delta t$ particles each timestep (Δt = 20 s). In Appendix B, results are presented from experiments on the choice of N as function of e and Q.

3.6 Input data requirements

The dispersion model uses gridded winds and turbulence parameters (such as PBL height, u_*, w_*, Obukhov length L) from a run of the windfield model to advect and diffuse the particles. These values are updated every ten minutes. Note that values of $\sigma_{u,v,w}$ needed for equations (3.3.2) and (3.3.4) under stable conditions are actually calculated by the windfield model, but that all calculations for convective conditions are done by the dispersion model.

For each source, it is necessary to specify emission characteristics needed for the plume rise calculations using the equations of Section 3.4. Table 3.1 contains values for Bayswater and Liddell power stations in the

Hunter Valley , as supplied by the Electricity Commission of New South Wales. Results from a case study in this region are presented in Chapter 4.

Values of power station load at half-hourly intervals were also provided by ECNSW and are plotted for Bayswater and Liddell in Fig. 3.1 for 30 November 1989. These values were used to vary the initial plume buoyancy via the exit velocity w_0 as follows:

$$w_0 = w_{0m}(MW/MW_m) \tag{3.6.1}$$

where MW is actual megawatt load and w_{0m} and MW_m are design maximum values specified in Table 3.1. It is assumed that the exit temperature of the plume does not vary with load.

station	maximum capacity MW_m	stack height z_s (m)	exit vel. w_{0m}	stack radius r_s (m)	stack gas temp.	enhance. factor N_E
Bayswater	2640	250 x 2	23.0	5.28	403	1.3
Liddell	1860	168 x 2	22.2	4.35	396	1.4

Table 3.1. Power station characteristics

The load curves in Fig. 3.1 are also used in conjunction with the coal statistics in Table 3.2 to determine the sulfur dioxide emission rate Q for each station,

$$Q = (MW \times SC \times 2)/(SE\ TE) \tag{3.6.2}$$

where SC = sulphur content (%), SE = specific energy (mJ/kg) and TE = thermal efficiency (%). The diurnal variation of emission rate for 30 November 1989 is shown in Fig. 3.2.

Station	Specific Energy mJ kg^{-1}	Thermal Efficiency % generated	Nov '89 Sulfur Content %
Bayswater	22.4	38	0.61
Liddell	22.3	33	0.60

Table 3.2. Coal statistics

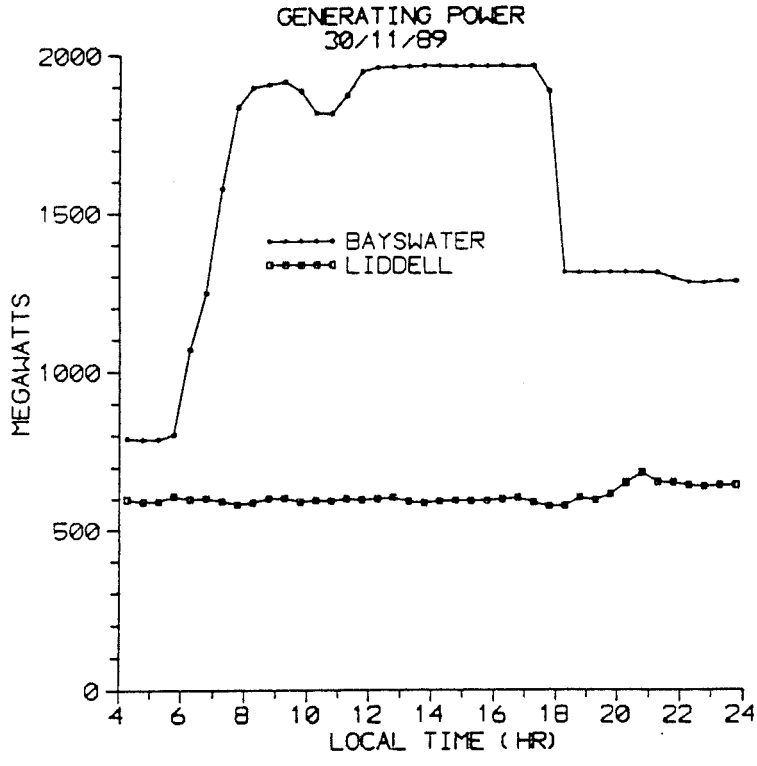

Figure 3.1: Load curves in megawatts for Bayswater and Liddell power stations on 30 November 1989.

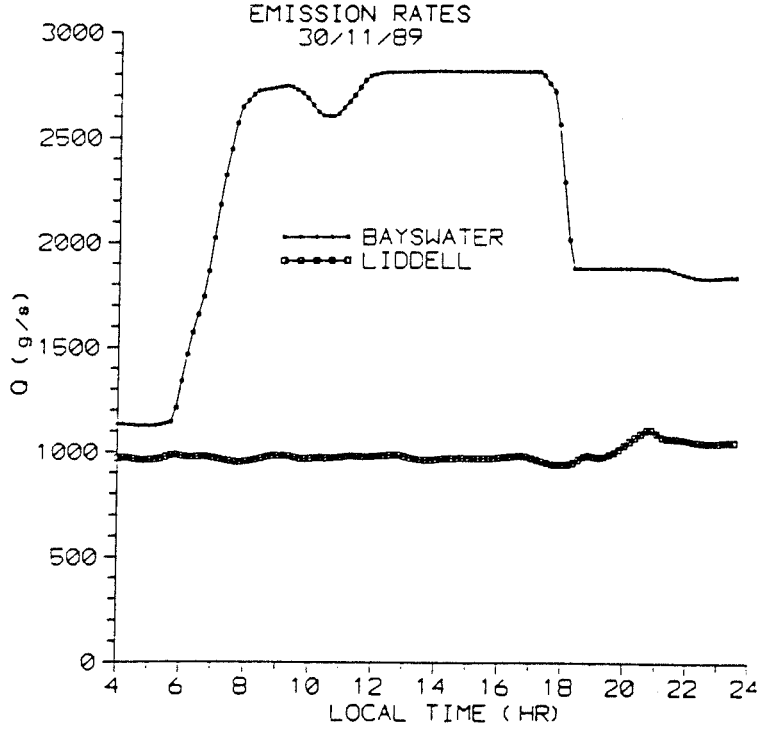

Figure 3.2: Diurnal variation of sulphur dioxide emission rate for each power station on 30 November 1989.

4 CASE STUDIES

In this Chapter validation studies of both the windfield and dispersion components of LADM are presented. We begin with an examination of the boundary-layer parameterisation by simulating a day from the Wangara data set.

4.1 Simulation of Wangara Day 33

The Wangara Day 33 data was used to evaluate the boundary-layer parameterization in the mesoscale model component of LADM. Results were also compared to a simulation with an established mesoscale model (the Colorado State University model, Mahrer and Pielke, 1977; McNider and Pielke, 1981).

The model was initialised using the 0900 Eastern Standard Time (EST) sounding on Day 33. The first model level was at 10 m followed by 25 m, with the next five at 25 m intervals to 150 m. Levels at a 50 m spacing up to 300 m were followed by levels at 100 m intervals to 900 m. The top three levels were at 1200, 1500 and 2000 m. The diurnal variation of the surface geostrophic wind (U_{g0},V_{g0}) was specified according to Yamada and Mellor (1975). Parabolic profiles were fitted to the observed geostrophic winds at 0900 and 2100 EST, also following Yamada and Mellor (1975), as follows:

$$U_g(z,t) = \frac{(\Delta U_g)_2 - (\Delta U_g)_1}{2 \times 10^6} z^2 + \frac{3(\Delta U_g)_1 - (\Delta U_g)_2}{2 \times 10^3} z + U_{g0}(t)$$

where $(\Delta U_g)_1$ and $(\Delta U_g)_2$ are the reported thermal winds differences from the surface to 1 km and from 1 to 2 km, respectively. The values for $(\Delta U_g)_1$ and $(\Delta U_g)_2$ at times between observations are linearly interpolated. V_g is obtained in the same way as U_g.

Values of soil and surface parameters used in the simulation were albedo = 0.2, roughness length = 0.01 m, soil density = 1.6×10^3 kg m^{-3}, soil specific heat = 858 J K^{-1} kg^{-1} and soil diffusivity = 5×10^{-7} m^2 s^{-1}.

The observed and predicted profiles of potential temperature at 1800 EST in Fig.4.1 indicate that the boundary-layer schemes of both models are able to simulate the temperature and depth of the mixed layer satisfactorily. However there is a suggestion that near-surface cooling at night is too shallow and this is confirmed by the 2400 EST profiles which show observed cooling to a height of 400 m (Fig.4.1). This problem is associated with the

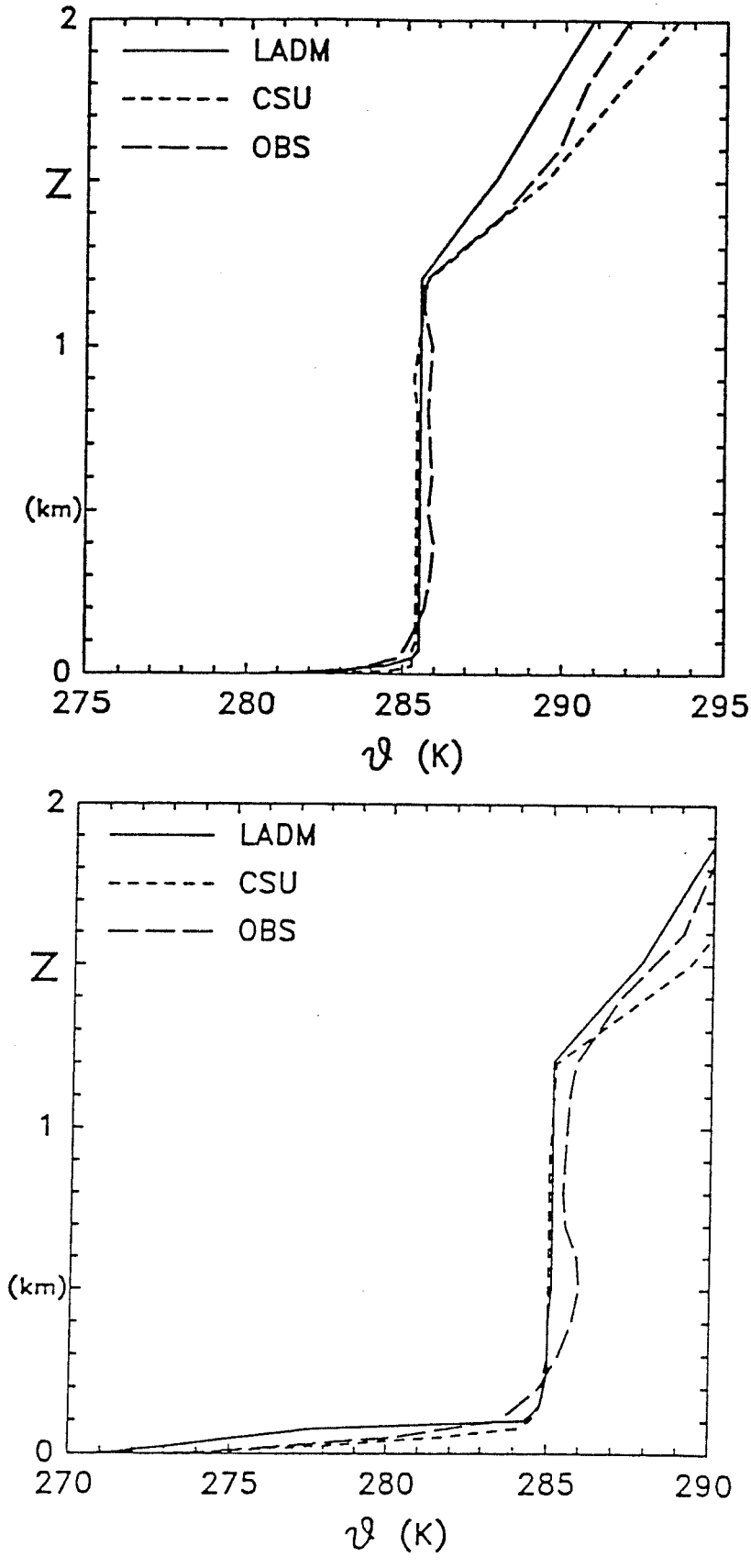

Figure 4.1: Predicted and observed profiles of potential temperature at 1800 EST (top) and 2400 EST (bottom) for Wangara Day 33.

longwave radiation scheme, as cooling from surface-generated nocturnal turbulence on Day 33 extends only to about 100 m (Andre et al., 1978). Day 33 simulations with higher-order turbulence schemes but similar radiation schemes (Yamada and Mellor, 1975; Andre et al., 1978; Mahfouf et al., 1987) also show inadequate nocturnal cooling. The temperature profile in the lowest 100 m is reproduced well by both models, but the scheme in LADM cools the surface too much.

Wind profiles at 1800 EST (Fig.4.2) show that both models predict the u-component to be slightly weaker than the observed and that both overestimate the v-component. This problem with the v-component is also encountered in other simulations of Day 33 (Yamada and Mellor, 1975; McNider and Pielke, 1981). The strong nocturnal jet at 2400 LST is well simulated by both models (Fig.4.2), although at a lower height than is observed. This is a consequence of the inadequate nocturnal cooling.

The components of the surface energy balance are also reproduced satisfactorily by both models. Fig.4.3 shows the net radiation and soil heat flux.

4.2 Deardorff and Willis laboratory experiments on fumigation

The fumigation of a plume during nocturnal inversion break-up is a process by which large ground level concentrations of pollutants can occur. After sunset in flat terrain a nocturnal temperature inversion grows upwards from the ground due to longwave radiative cooling. This layer grows throughout the night until the sun rises in the early morning and starts to heat the ground. The heating of the ground produces an upward sensible heat flux which creates ground-based convective turbulence which starts to 'eat away' the nocturnal inversion, thus producing a ground-based convective layer commonly called the mixed layer. As this convective layer grows, it can entrain an elevated plume which was emitted into the stable atmosphere within or above the nocturnal inversion and so fumigate (or mix) it to ground.

In the laboratory, Manins (1977) clarified aspects of inversion erosion by examining the fumigation process in a qualitative manner. Deardorff and Willis (1982) performed water tank experiments for a ribbon plume under both slow and fast entrainment conditions. The experiments, representative of free convection conditions, showed that the instantaneous mixing of pollutant uniformly into the mixed layer was physically wrong, and that the mixing

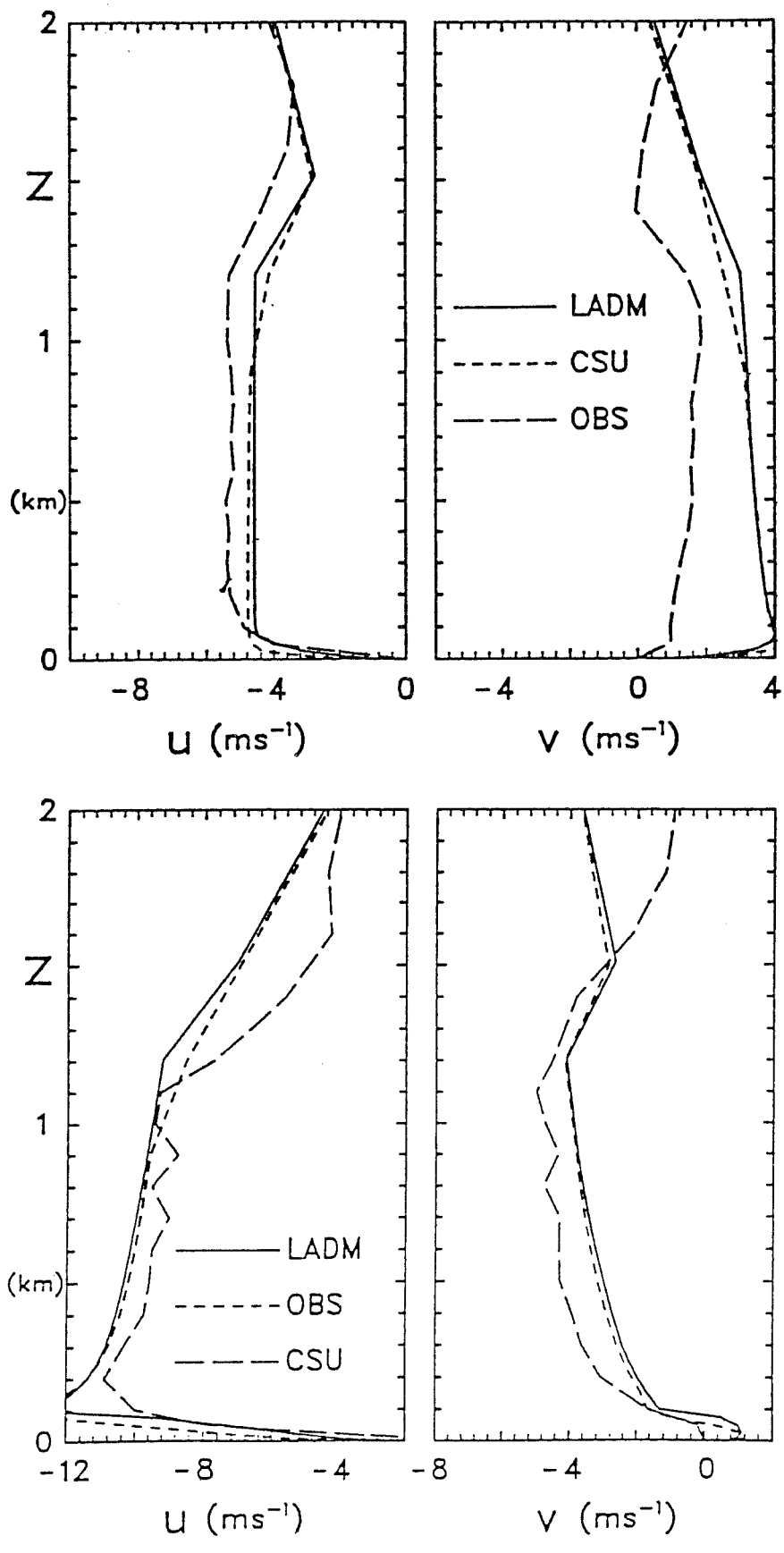

Figure 4.2: Predicted and observed profiles of the u- and v-components of the wind vector at 1800 EST (top) and 2400 EST (bottom) for Wangara Day 33.

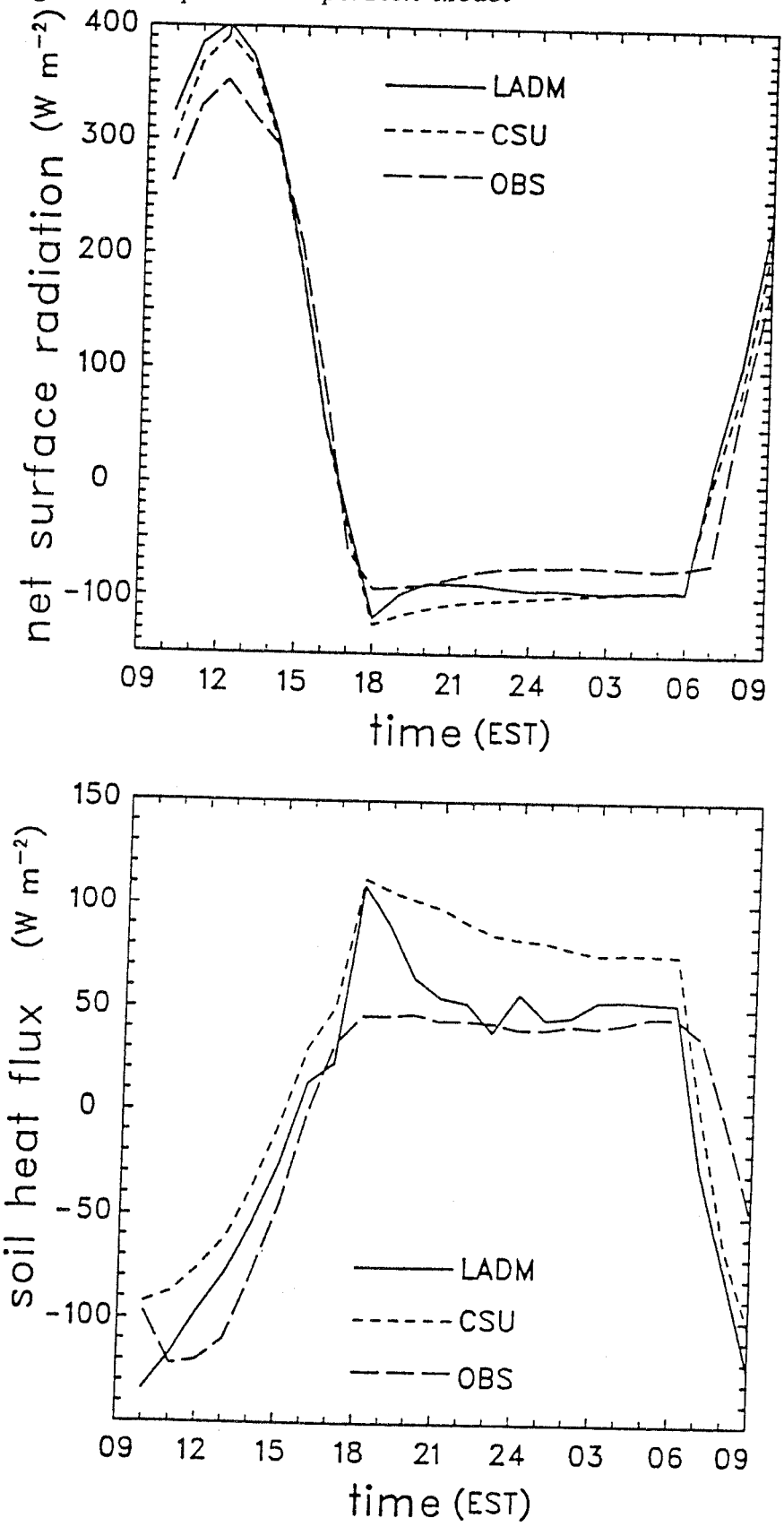

Figure 4.3: Predicted and observed diurnal variation of net surface radiation (top) and soil heat flux (bottom) for Wangara Day 33.

height is not strictly a step-like boundary but a layer of transition between the convective eddies and the stable atmosphere aloft. Using Gaussian plume assumptions, those authors developed a mathematical model for the prediction of ground-level concentrations arising from fumigation processes. Important features of the model are a) time-weighted functions to account for the non-instantaneous mixing assumption and for variability of the mixing height with position, and b) an enhanced lateral dispersion function. The equations were fitted to the averaged tank data and are applicable to conditions under which the experiments were done; namely an infinitely thin (ribbon) plume and free convective conditions. The modified Deardorff and Willis fumigation model (MDWFM) is an extension of their model which accounts for the effect of finite σ_{z_i} (see Hurley and Physick, 1991).

Earlier, Turner (1970) had used a Gaussian plume approach to model the fumigation process, in which the standard Gaussian plume equation is integrated over the vertical extent of the mixed layer. This approach assumes instantaneous uniform mixing in the mixed layer of that fraction of the plume below the mixing height, with the only time-dependent variable needed being the height of the mixed layer.

The extent to which the dispersion component of LADM is able to simulate the fumigation process has been investigated by simulating the Deardorff and Willis (1982) laboratory experiments. The results of this study can be found in Hurley and Physick (1991). A summary of the findings from that paper is now presented here.

4.2.1 The Numerical Experiment

Fumigation of an elevated plume with an initial Gaussian cross-section was simulated with the Lagrangian particle model described in Chapter 3. The initial dimensions of the plume were σ_y = 250 m and σ_z = 40 m with an initial plume centerline height of z_p = 400 m. The emission rate used was Q = 100 g s^{-1}, and the wind speed along the plume was u = 5 m s^{-1}, corresponding to the synoptic wind of the mesoscale model.

The Gaussian plume was set up for the Lagrangian particle model by discretising the plume and calculating the number of particles needed for each cross-sectional segment to give an overall cross-sectional Gaussian distribution for a given mass emission rate. This was done by using the

standard Gaussian plume equation and converting concentration at a point into a particle number density within a discretised box. Each particle was assigned a mass Δm = Q*(unit time)/10 chosen to give a reasonable number of particles (5000) for the simulation. Particles were then given an initial position corresponding to the discretisation box position.

The two-dimensional grid used for calculating concentrations was 1000 m high with 25 m spacing and 10000 m wide with a spacing of 100 m. Concentrations were calculated by counting the number of particles in each box for each time-step and averaging these over time.

In these fumigation experiments (carried out while the windfield model component of LADM was still under development), the meteorological variables needed by the particle model were provided by the Colorado State University mesoscale model (Mahrer and Pielke, 1977; McNider and Pielke, 1981). It was run in one-dimensional mode and initialised at sunrise with parameter values representative of summertime conditions in the mid-latitudes. Relevant model predictions are shown in Figure 4.4. In order to properly simulate the conditions of the Deardorff and Willis fumigation experiments, the wind of the mesoscale model was forced to be constant in direction, i.e. there was no frictional turning.

4.2.2 Results

In our first experiment, once all of the plume had been entrained into the mixed layer,the mesoscale inputs were kept constant for a further 100 minutes (approximately 18 convective timescales). An hourly-average concentration was calculated over the final 60 minutes of these steady state-conditions in order to examine the model's ability to mix particles uniformly throughout the convective layer. The right-hand plot of Figure 4.5 shows the steady-state cross-plume integrated concentration profile for this final hour, non-dimensionalised by the analytic solution C_a, using a timestep of 60 seconds. It is obvious that our model with a *homogeneous* turbulence parameterisation does satisfy the well-mixed criterion. However the other profile of Fig. 4.5, which shows results from a similar Lagrangian particle model (Sawford and Guest, 1987) but with *inhomogeneous* turbulence and a 20-second timestep, exhibits a deficit of particles near the surface and is definitely not well mixed. We show this profile merely to illustrate our

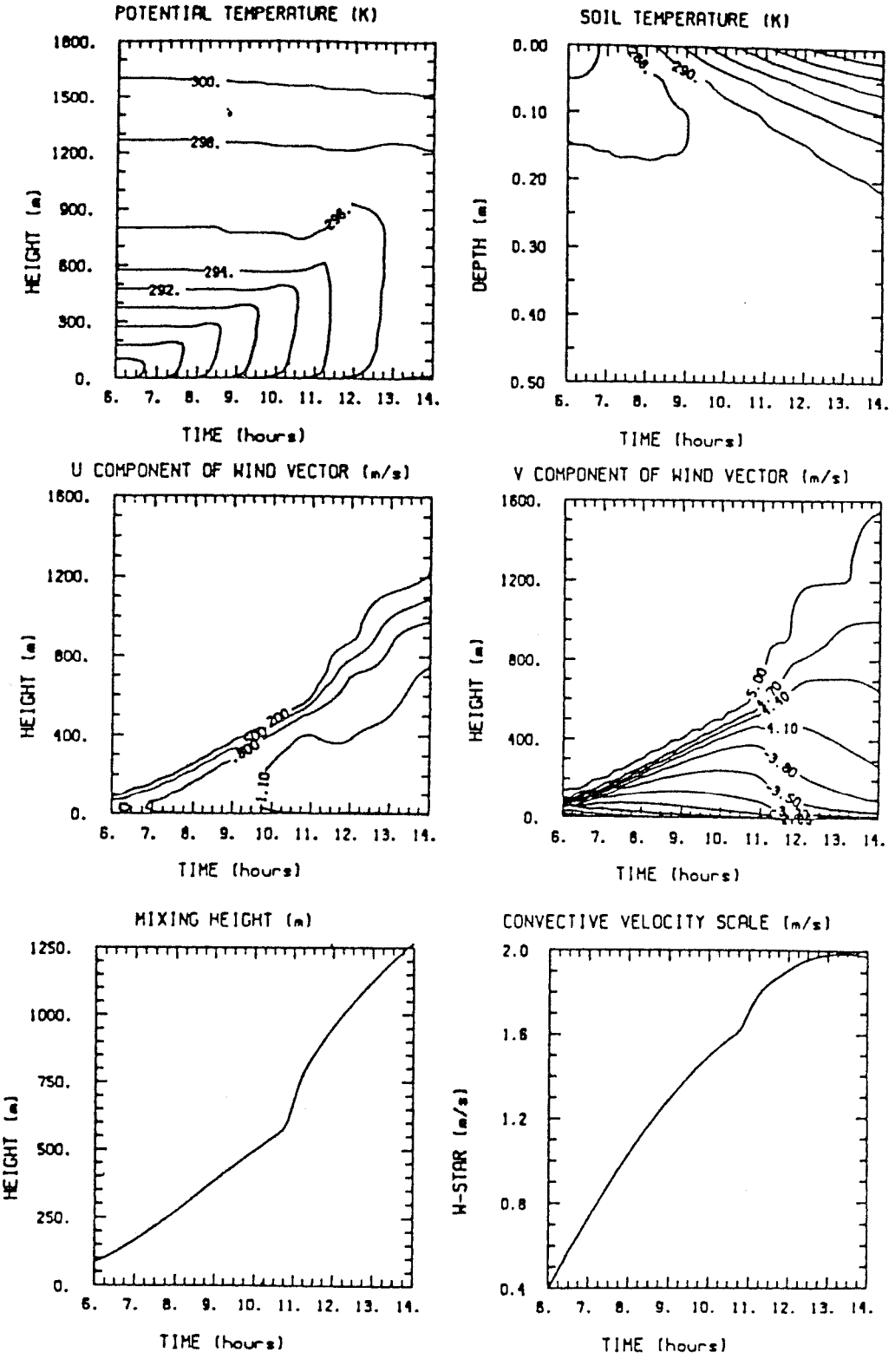

Figure 4.4: Time series of predictions from the mesoscale model.

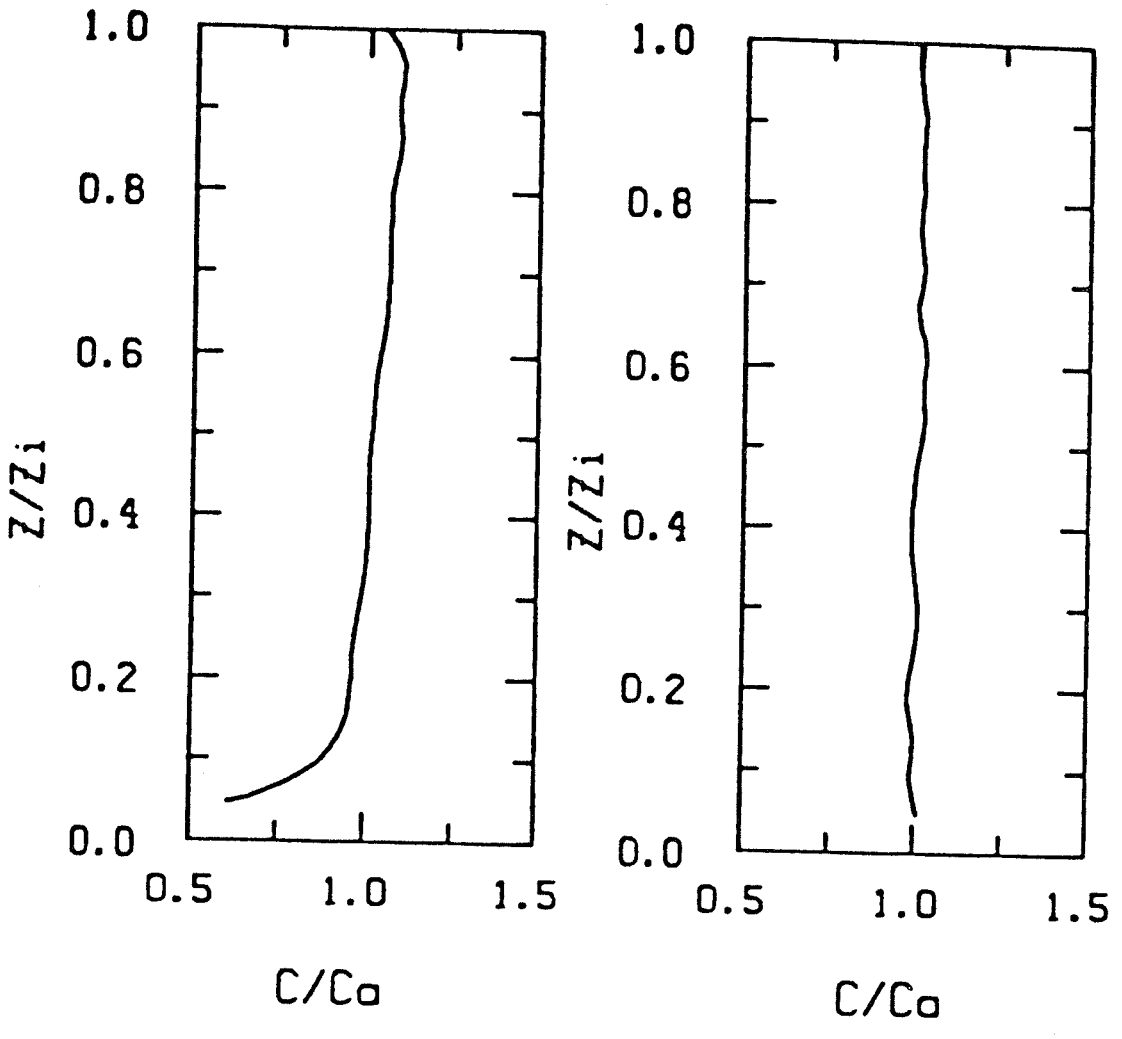

Figure 4.5: Steady-state cross-plume integrated profiles for the inhomogeneous particle model of Sawford and Guest (1987) using a 20-second timestep (left), and the homogeneous particle model used in LADM with a 60-second timestep (right). Ca is the analytic solution, implying C/Ca = 1 is the exact solution.

assertion in Section 3.2.1 that an inhomogeneous turbulence parameterisation can severely limit the size of the model timestep. When the timestep is reduced (sometimes as small as one second) so that it is always small enough to resolve the scale of turbulence near the boundaries, the profile remains well mixed (see Hurley and Physick, 1991 for the timestep criterion and further discussion).

The hourly-averaged maximum ground-level concentrations from the fumigation simulation *without* restricting the growth of the mixing layer in the final stages, are shown in Table 4.1. Results from the MDWFM, in effect reproducing the laboratory data, and the Turner model (TFM) are also shown.

HOUR	TFM	MDWFM	LPM4
0900	13	2	3
1000	51	24	23
1100	47	26	19
1200	39	19	12

Table 4.1. Hourly-averaged maximum ground-level concentrations ($\mu g\ m^{-3}$) predicted by the Turner Fumigation Model (TFM), the modified Deardorff and Willis fumigation model (MDWFM) and the Lagrangian particle model (LPM).

In comparison to the MDWFM, the TFM produces the maximum concentration at an earlier time and also predicts concentrations which are too large by about a factor of two. The results also show that our particle model (LPM) predicts the maximum to occur too early, although it should be noted that there is little difference between the 1000 hour maximum and the value at 1100 hours. Although the LPM prediction at this time is about 27% less than the MDWFM value, Deardorff and Willis state that four constants in their model are free to be altered by ±30%, leading to variations of this magnitude in the concentrations.

It should be realised that averaging concentrations over many convective timescales (note here that 1 hour is approximately 12 convective timescales) has the effect of reducing and broadening the peak concentration. According to Deardorff and Willis the time taken for fumigation of a ribbon plume is approximately 16-20 convective timescales, and here the time equivalent distance between the lowest ribbon plume and the highest ribbon plume, of the composite Gaussian plume being simulated, is approximately 24 convective

timescales. This means that the total time taken to fumigate the composite Gaussian plume is of the order of 40 convective timescales, which is approximately 3-4 hours. Therefore, although averaging can reduce the sensitivity of results, in this numerical experiment the degree of averaging still allows a meaningful comparison of fumigation models to be made.

This comparison of the dispersion component of LADM with data from laboratory experiments gives us confidence that we are able to simulate the essential processes of fumigation of an elevated plume.

4.3 Hunter Valley windfields

The results in this Section are taken from a Report to the Electricity Commission of New South Wales (Physick et al., 1991). One of the objectives of the study was "to demonstrate the suitability and value of a prognostic windfield model/Lagrangian particle model approach to ECNSW air quality assessment needs in the Upper Hunter Valley", where the commission currently operate two coal-fired power stations. For a case-study day, we chose a day on which mesoscale flows significantly perturbed the synoptic wind pattern. Our modelling system LADM is designed to handle the complex winds observed under such conditions whereas the assumptions inherent in the Gaussian plume air quality models often lead to poor results in these situations. We selected 30 November 1989, a clear-sky day of light northwesterly synoptic winds, and on which a sea breeze penetrated to over 100 km inland.

4.3.1 Analysis of observations

The data network and power station sites can be seen in Fig. 4.6. Synoptic charts prepared by the Bureau of Meteorology for mean sea-level pressure (MSLP) and the geopotential height of the 850, 700 and 500 hPa surfaces are shown in Fig.4.7 for 1000 EST on 30 November 1989. Over the Hunter Valley region (marked on the east coast of Australia in Fig.4.7b), a north to northwesterly pressure gradient exists at the surface, but at higher levels gradients suggest extremely light and variable winds.

However, when data from the region are examined, the strong influence of mesoscale terrain- and coastline- features on the windfield is evident. For example, at the coastal site of Eraring, the sea breeze changes mid-morning westerly component winds to afternoon easterlies (Fig.4.8). After sunset,

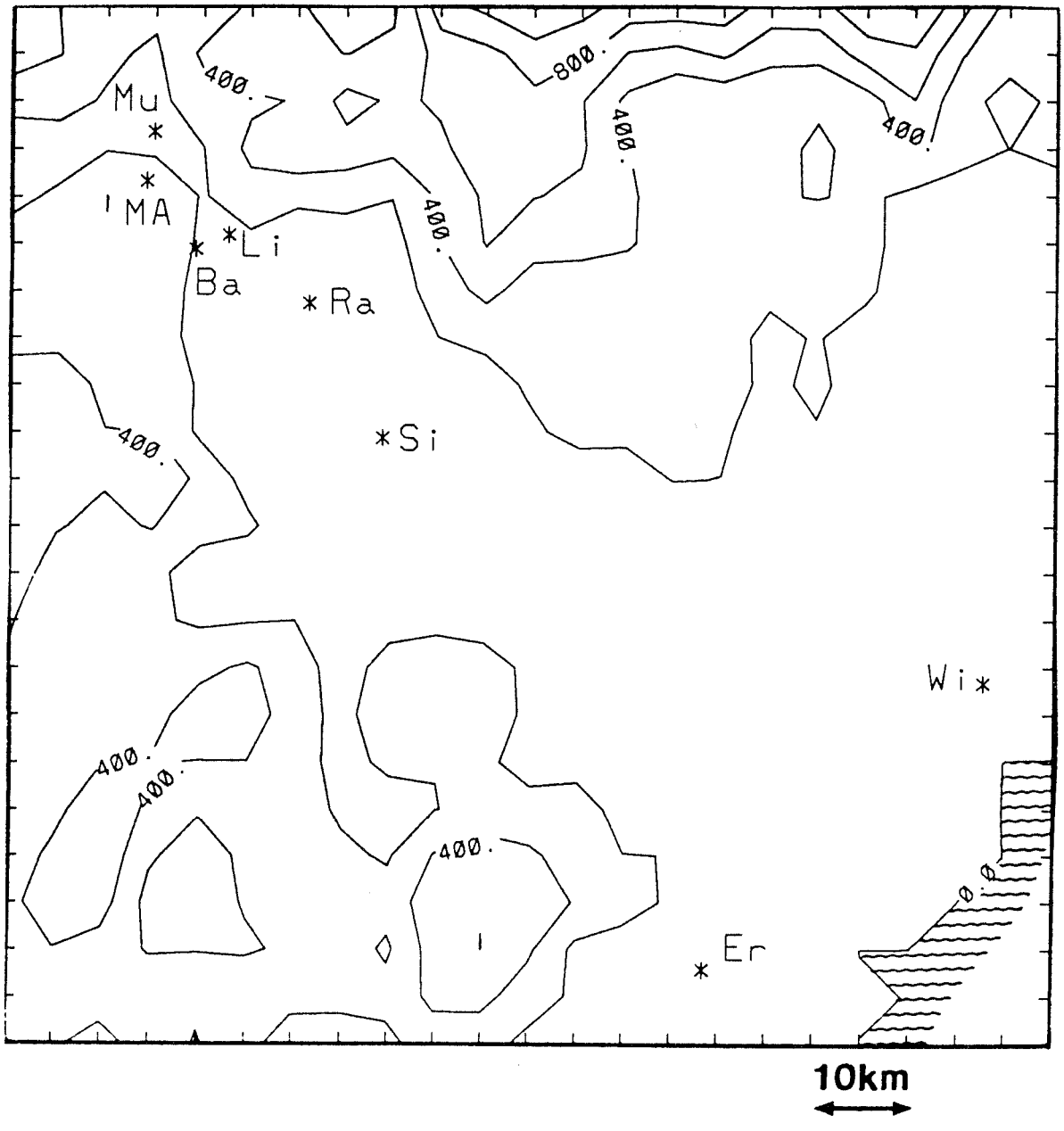

Figure 4.6: Hunter Valley region showing the power station sites, Liddell (Li) and Bayswater (Ba), and the data network. Rawinsondes and tethersondes were released from Liddell while 10 m winds were measured at Liddell and Ravensworth (Ra). Surface concentrations of SO2 were obtained from monitors at Muswellbrook (Mu), Mount Arthur North (MA), Liddell, Ravensworth and Singleton (Si). An acoustic sounder was located at Eraring (Er) and Bureau of Meteorology rawinsonde data were obtained from Williamtown Wi).

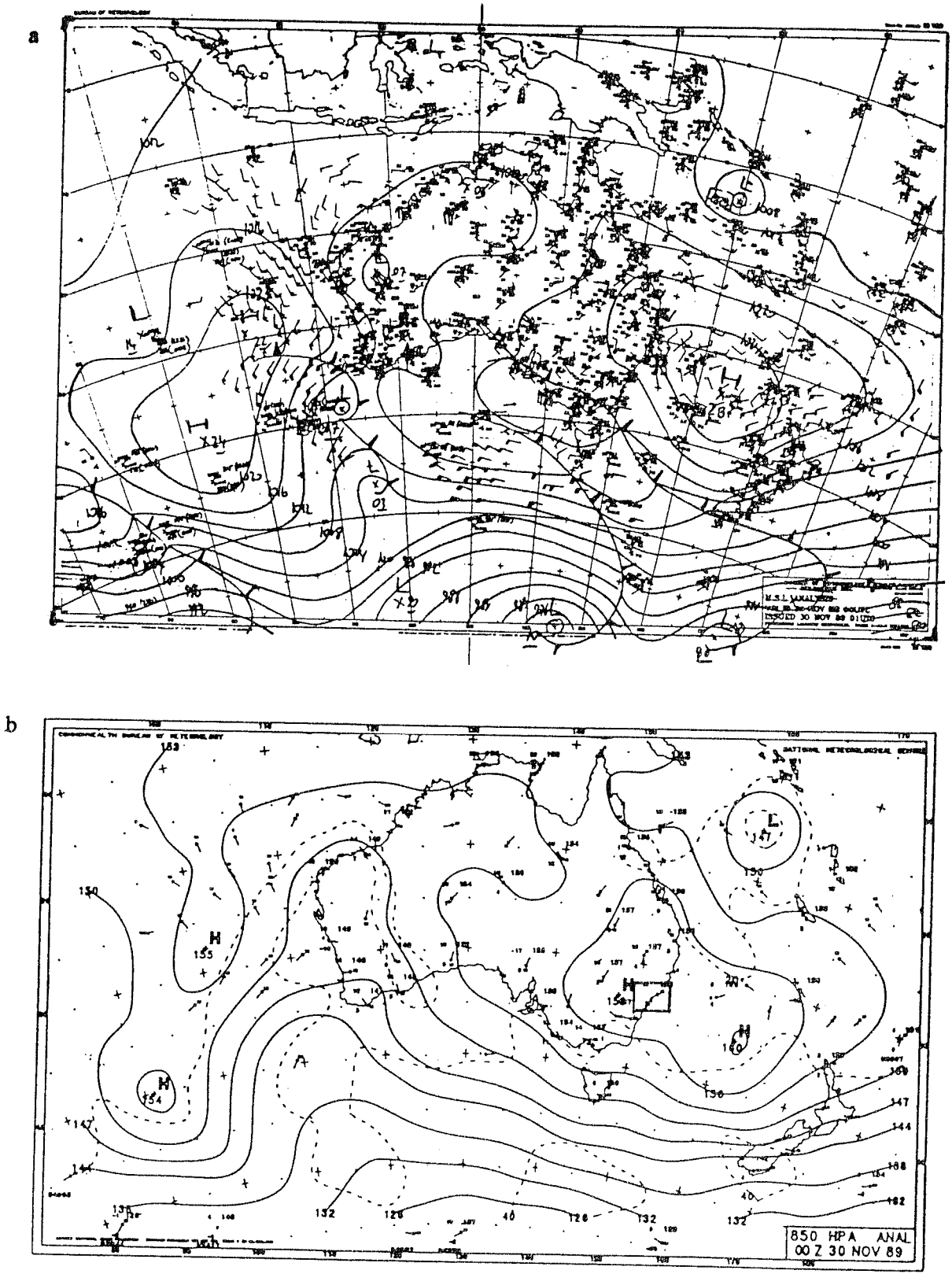

Figure 4.7: (a) Mean sea-level pressure chart and (b) 850 hPa geopotential height charts, at 1000 EST 30 November 1989. Courtesy of the Bureau of Meteorology.

c

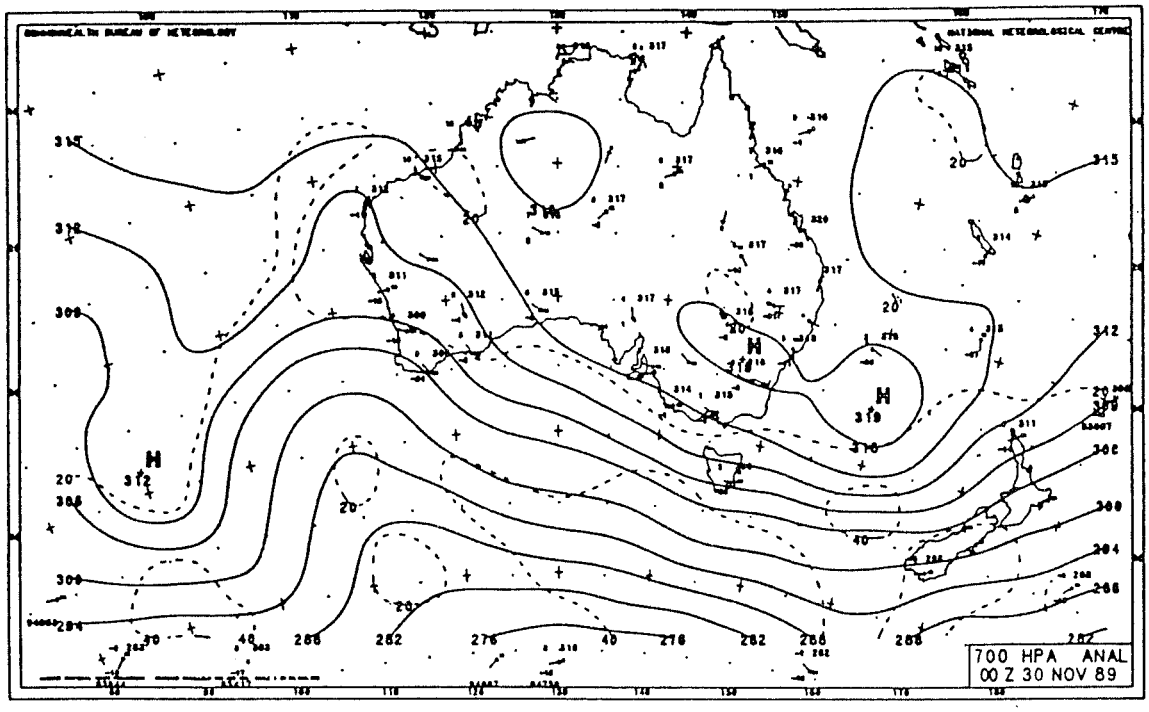

d

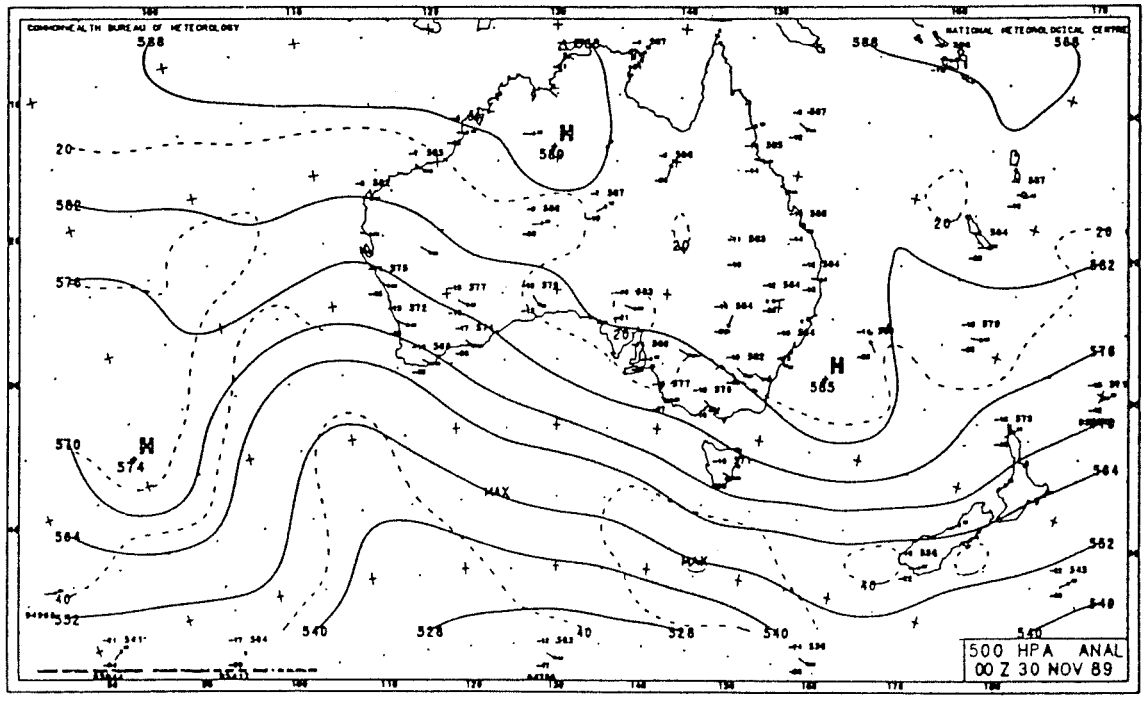

Figure 4.7: (c) 700 hPa and (d) 500 hPa geopotential height charts, at 1000 EST 30 November 1989. Courtesy of the Bureau of Meteorology.

Coriolis turning and decoupling of higher-level winds from the surface produces a strong northerly jet at 300 m (Fig.4.8).

At another coastal site, Williamtown, radiosonde data are available to heights greater than 7000 m, although the resolution is poorer than for the Eraring acoustic sounder data. These winds (Fig.4.9) show the onshore sea-breeze flow to be about 1000 m deep, with a veering of the winds above to an offshore direction. The layer of winds from the southwest quadrant between about 1500 and 3000 m is a persistent feature throughout the 24-hour period and most likely arises from the return flow of the sea breeze.

Wind and temperature data are also available from five airsonde flights between 1100 EST and 1500 EST at Liddell, about 90 km inland. At 1100 EST, light to moderate west-northwesterly winds are evident below 1500m (Fig. 4.10). Above this level, the winds switch sharply to a southeasterly direction. By the afternoon, winds up to 1500 m have become extremely light (less than or equal to 1 m s^{-1}) with a general southwesterly drift (Fig.4.10).

Anemometer data (10 m above the ground) from Liddell (Fig.4.11) show that a sea breeze reaches there soon after 1900 EST. The Ravensworth anemometer indicates sea-breeze passage at about an hour earlier. Also evident in Fig.4.11 are the west-northwesterlies found in the 1100 EST wind profile at Liddell (Fig.4.10). An onset time between 0500 and 0600 EST is suggested by Fig.4.11. These winds may be the synoptic flow re-establishing itself as local mesoscale pressure gradients weaken after sunrise, or they may be a regional drainage flow down the Hunter Valley as suggested by Hyde et al. (1981). Although the arrival time is later than those examined by Hyde et al., there have been other cases with similar onset times (Malfroy, ECNSW, personal communication, 1991).

In summary, the dominant features of the windfield in the Hunter Valley region for this day were:

A sea breeze which switches early morning offshore winds near the coast to onshore and which backs from easterly during the day to northerly by midnight.

Inland penetration by the sea breeze, to the extent that it reaches Liddell by early evening.

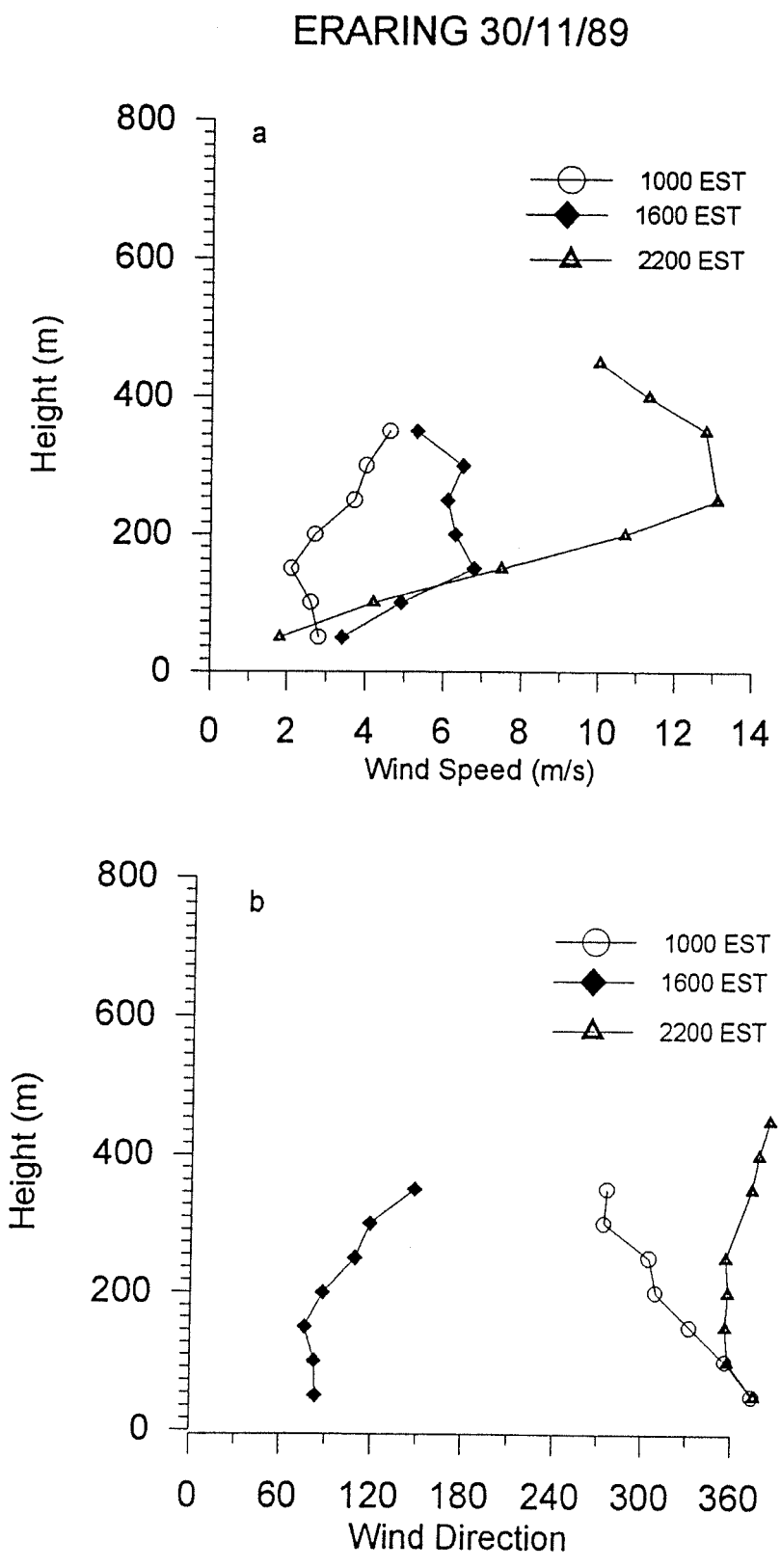

Figure 4.8: (a) Wind speed and (b) wind direction data from an acoustic sounder at Eraring on 30 November 1989.

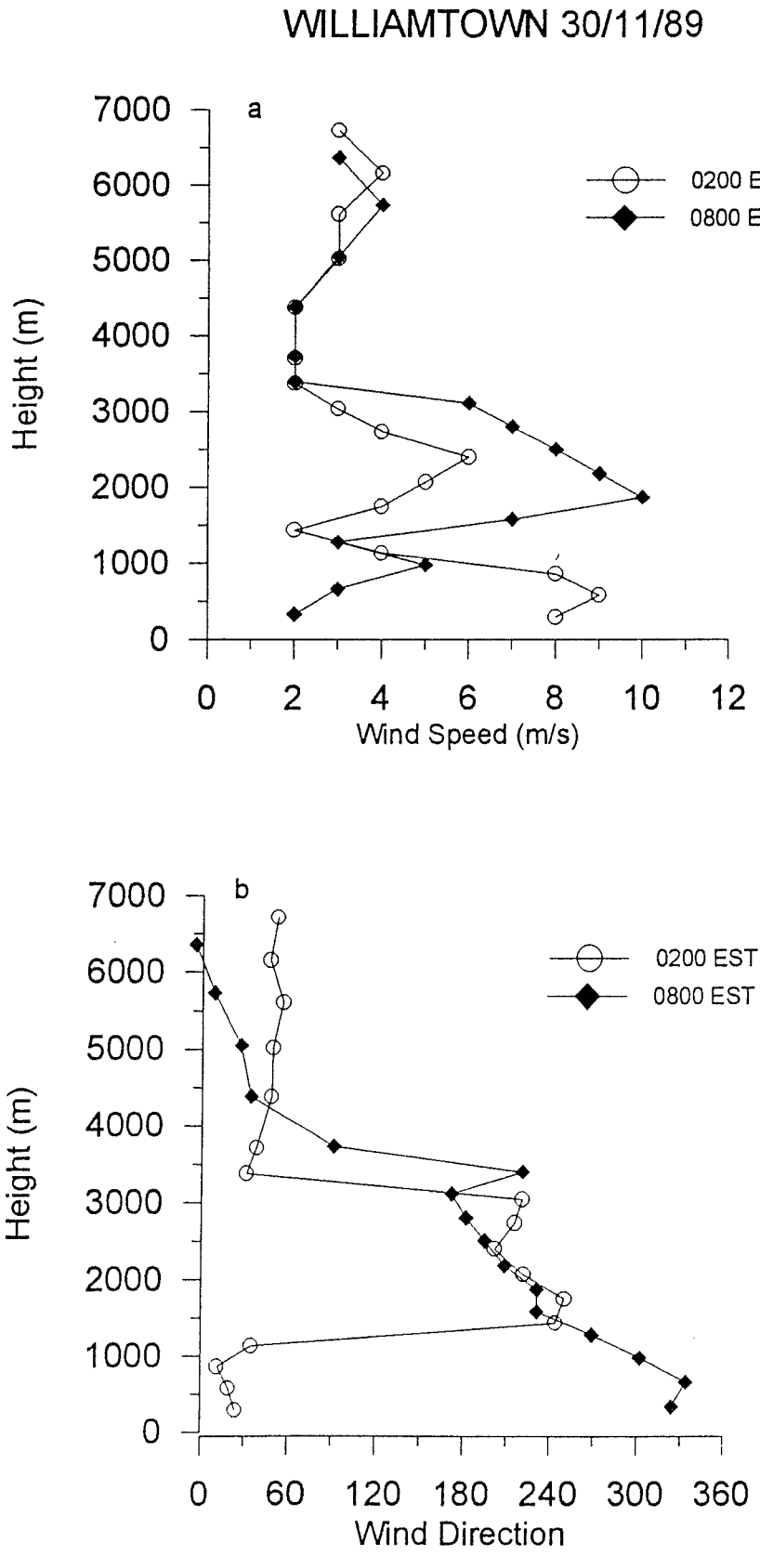

Figure 4.9 (a) and (b): Wind speed and wind direction data from rawinsonde ascents at Williamtown on 30 November 1989. Data courtesy of the Bureau of Meteorology.

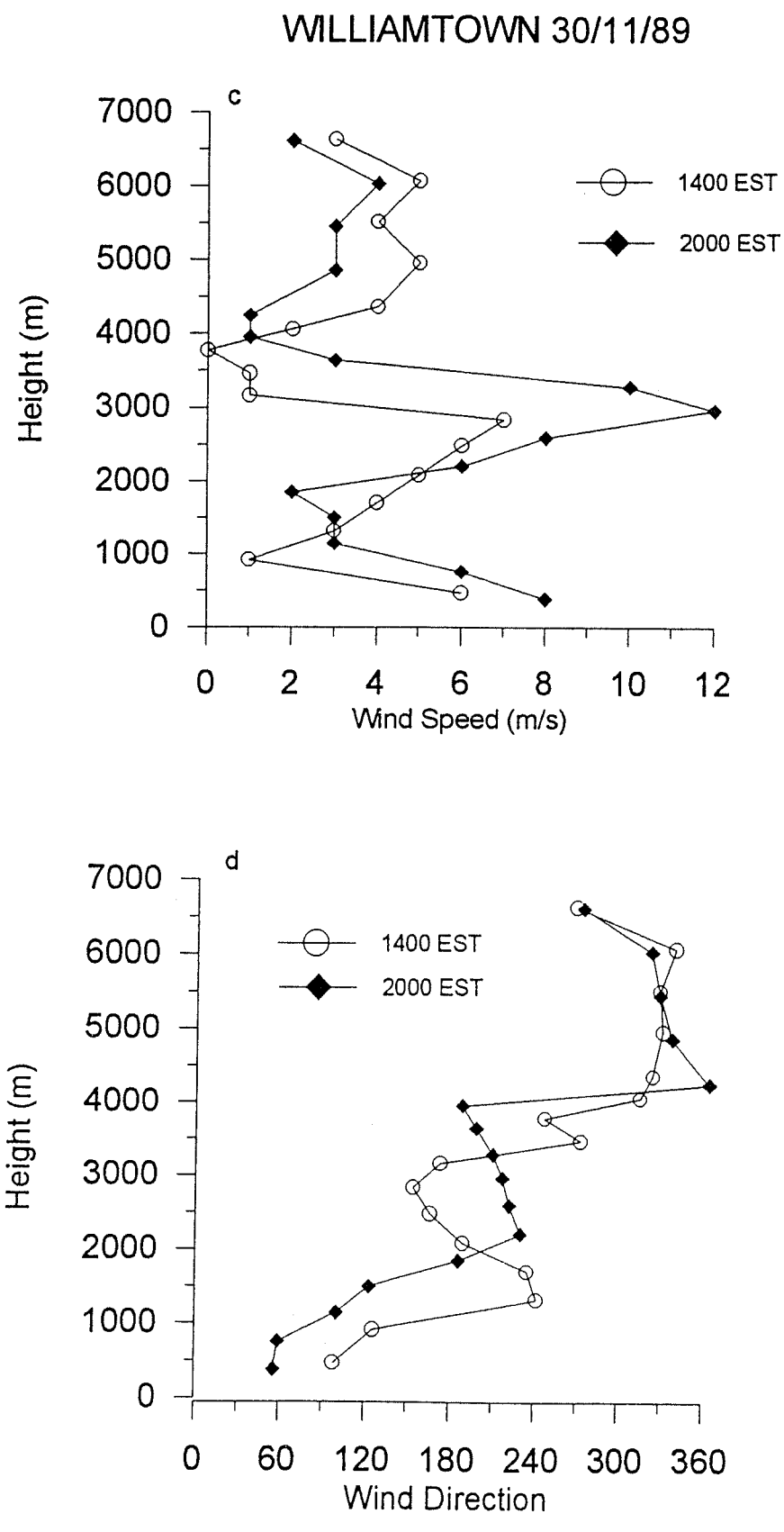

Figure 4.9 (c) and (d): Wind speed and wind direction data from rawinsonde ascents at Williamtown on 30 November 1989. Data courtesy of the Bureau of Meteorology.

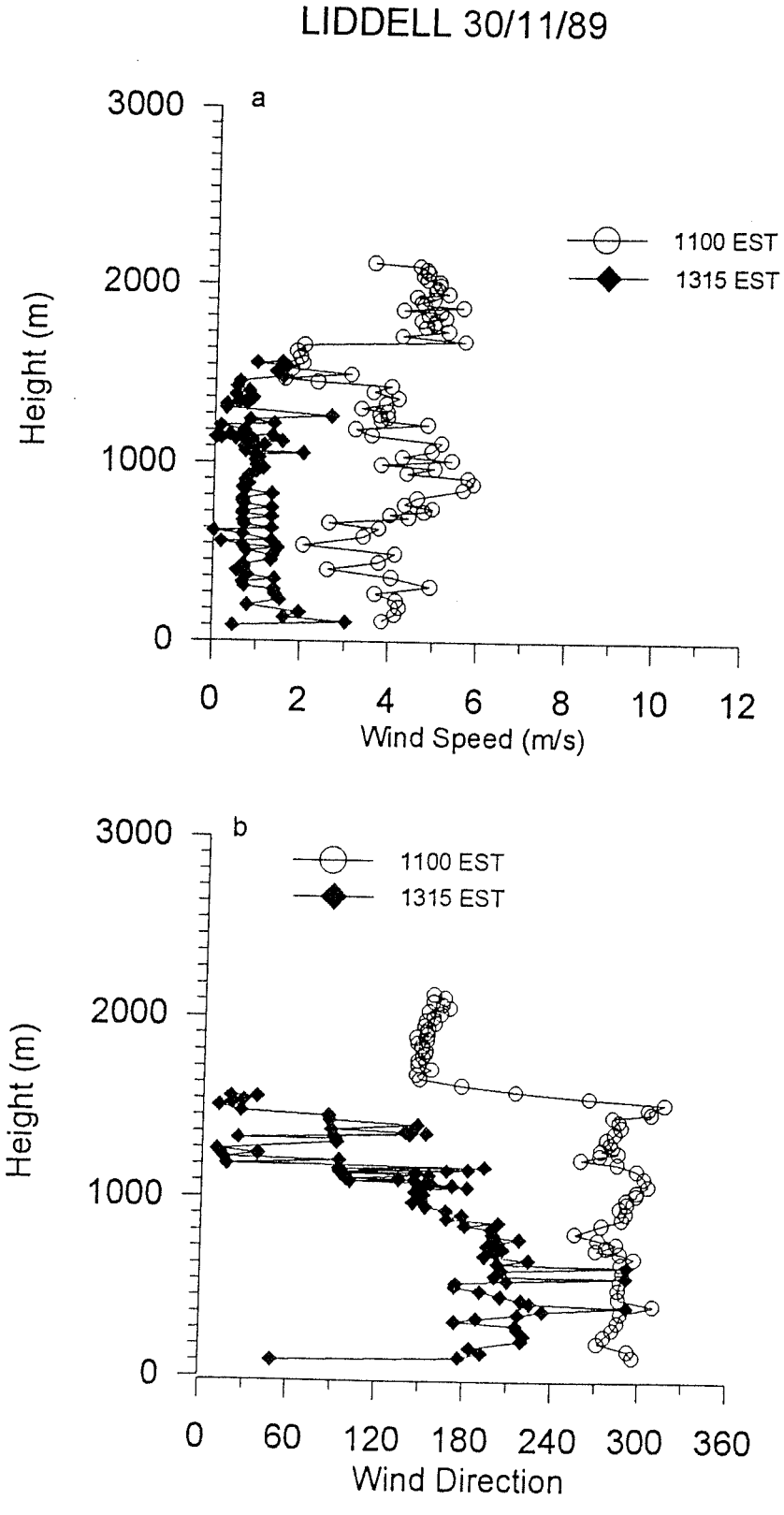

Figure 4.10: Observations of (a) wind speed and (b) wind direction profiles at Liddell on 30 November 1989.

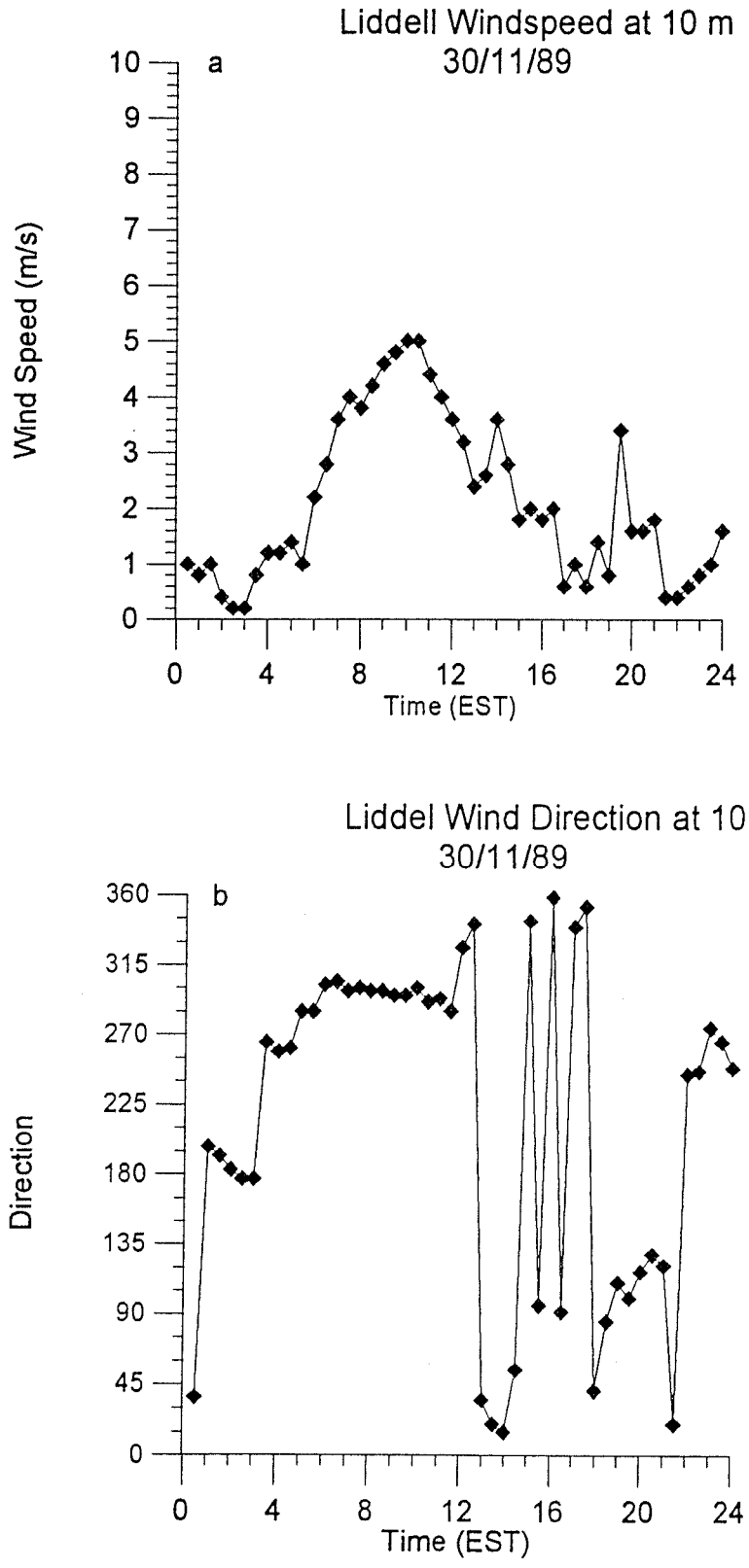

Figure 4.11: Wind speed (a) and wind direction (b) data from Liddell at 10 m above the ground on 30 November 1989.

A nocturnal jet in the coastal region at 300 m above the ground.

A persistent layer of southwesterly winds between 1500 and 3000 m at the coast.

A 4 m s^{-1} west-northwesterly drainage flow at Liddell, beginning around sunset and continuing till midday.

Extremely light winds with a southwesterly drift in the afternoon at Liddell.

4.3.2 Initial conditions for the windfield model

For this study, the mesoscale model was nested only once. Firstly it was run with a domain size of 540 by 540 km, made up of 55 gridpoints in both the north-south and east-west directions with a grid spacing of 10 km. The second run used a smaller domain (also 55 by 55 gridpoints) and a smaller grid spacing of 5 km, enabling finer resolution of topographic features. It is the wind and turbulence fields from this second run which are used to drive the particle model. The lateral boundary conditions during this run are obtained from the earlier run on the coarser grid. The inner and outer domains used in this study are shown in Fig. 4.12.

The model run begins at 0200 Local Solar Time (LST). Note that LST is always used when discussing model results, and EST when referring to observations. For comparison purposes in this Report, they can be considered equivalent. The initial temperature and humidity profiles (Table 4.2), specified at all gridpoints, are based on the 0800 EST 30/11/89 radiosonde flight from Williamtown. The temperature profile incorporates the main observed features, such as heights and strengths of inversions, and slightly stable layers. In the lower layers, the mixed layer of the 0800 EST profile has been removed and replaced by a stable gradient. However, the stability of this layer is less than would normally occur over land at night, and is specified to be more typical of a marine boundary layer with a sea-surface temperature of 20°C, the climatological mean for this time of the year. As the model run begins at 0200 LST, there is ample time before sunrise for radiational cooling to produce a nocturnal boundary layer over land. Initial surface pressure (p*) at mean sea level is set to 1024 hPa.

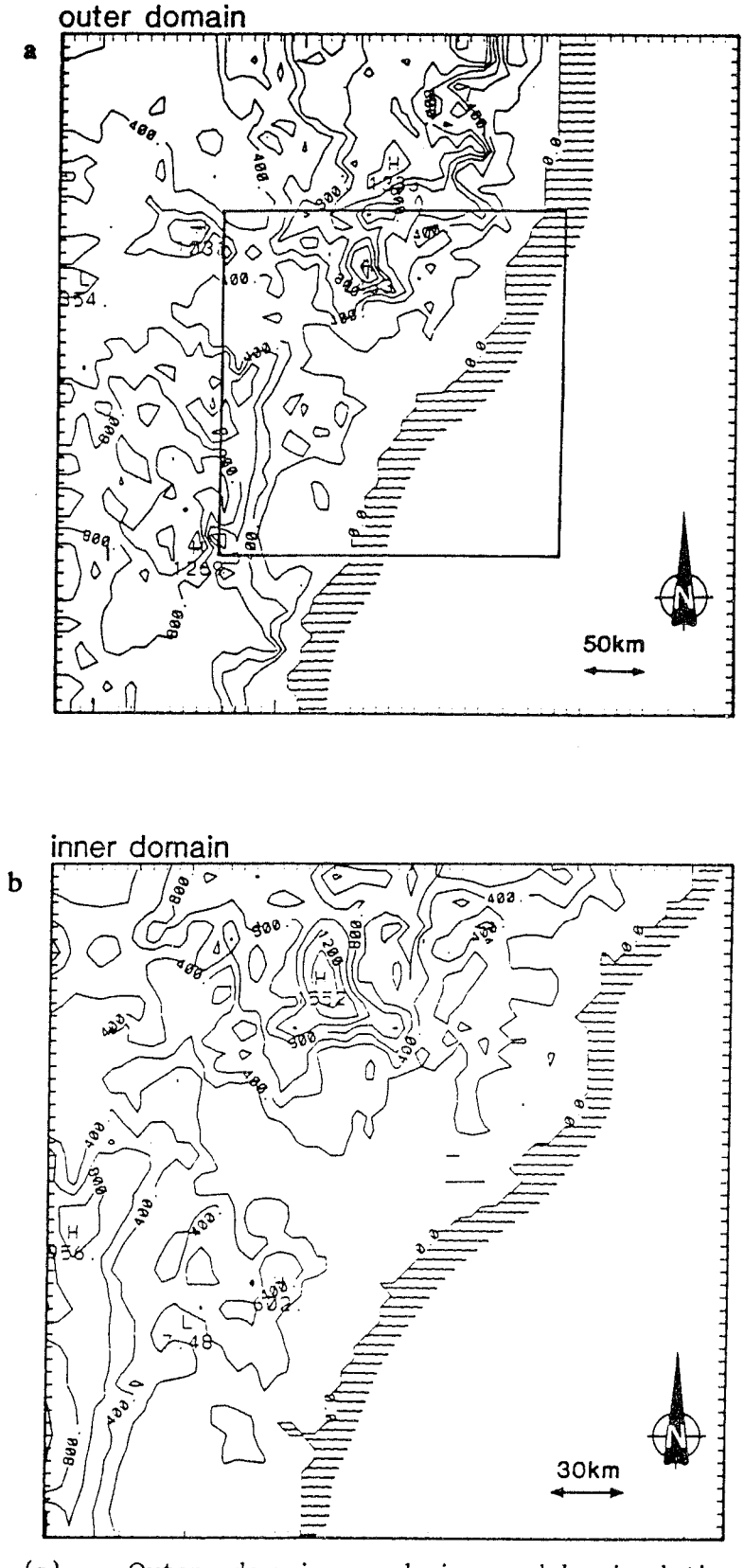

Figure 4.12 (a): Outer domain used in model simulations. Orography is resolved at 10 km resolution. Contour interval is 200 m. Location of inner grid is indicated by the square. (b). Inner domain, in which topography is resolved at 5 km resolution. Contour interval is 200 m.

$\sigma=p/p^*$	z (m)	temp. (^{o}C)	pot.temp. (K)	humidity (g kg^{-1})
.9960	33	21.30	292.65	10.32
.9880	100	23.99	296.00	9.95
.9705	250	22.81	296.34	8.90
.9535	400	21.67	296.69	7.35
.9311	600	20.11	297.14	5.30
.8987	900	17.84	297.83	5.00
.8673	1200	15.93	298.90	3.90
.8267	1600	14.42	301.45	5.20
.7875	2000	10.74	301.75	4.80
.7408	2500	6.24	302.20	4.30
.6961	3000	6.21	307.60	1.00
.6533	3500	3.06	309.70	0.70
.5745	4500	-4.32	312.70	0.60
.5036	5500	-11.77	315.70	0.50
.4551	6250	-17.42	317.95	0.50
.4106	7000	-23.08	320.20	0.30
.3697	7740	-28.76	322.45	0.30
.3321	8490	-33.94	325.45	0.20
.2975	9240	-39.21	328.45	0.20
.2659	9985	-44.53	331.45	0.10
.1800	12560	-62.30	341.75	0.10

Table 4.2. Initial temperature and humidity profiles for model simulation of 30/11/89. Approximate heights (z) of the σ-levels are also shown.

Guidance as to the windfield specified at this initial time was obtained from the synoptic pressure charts (Fig.4.7). Accordingly, we specified a 3 m s^{-1} northwesterly wind at the surface, decreasing linearly to 0.0 m s^{-1} at a height of 900 m and remaining at zero to the model top (19800 m). The model was integrated for 48 hours and results from the second 24-hour period were

compared to observations. In this way, the windfield at 0200 LST after 24 hours contains mesoscale perturbations arising from coastline and orographic influences. For example, the wind profile at this time for the gridpoint corresponding to Williamtown is shown in Fig.4.13. Comparison with the observed winds (Fig.4.9) reveals the model has been able to reproduce the directional vertical shear, including the layer of southwesterly winds between 1500 and 3000 m and the associated jet. It was not as successful in reproducing the magnitude of the low-level jet at about 600 m.

We begin releasing particles at 0400 LST (see following Sections), and windfields for this time at different heights are shown in Fig.4.14. Wind patterns inland and in the coastal region differ markedly from each other, and strong vertical wind shear is evident in all areas. At the lowest level (Fig.4.14a), local katabatic winds are predicted, especially on the slopes of the Blue Mountains, while at 600 m (Fig.4.14b) the flow is less influenced by orography. The strong southerly flow at 2400 m (Fig.4.14d) is confined to coastal regions and is associated with a mesoscale pressure gradient set up by the sea breeze, in a similar manner to that observed by Physick and Abbs (1991) in the Latrobe Valley region.

Observations near this time include the 0200 EST Williamtown upper winds, discussed previously with respect to Fig.4.13, and wind at 10 m from Liddell (Fig.4.11). The latter shows light and variable-direction winds of 1 m s^{-1} or less, in good agreement with the predictions of Fig.4.14a. Also available are the acoustic sounder data from Eraring (not shown), which indicate a weak westerly drainage flow less than 100 m deep, below a virtually northerly flow of about 5 m s^{-1} up to the sounder limit of 400 m. Model agreement in this locality is not good, where southerly winds up to more than 100 m above the surface are predicted to lie below northwesterlies (Figs.4.14a,b). One possible reason for the disagreement is that the flow in this area, especially in stable nighttime conditions, is likely to be strongly influenced by the complex lakes system. However, the small scale of these lakes is not resolved by the 5 km grid spacing of the model.

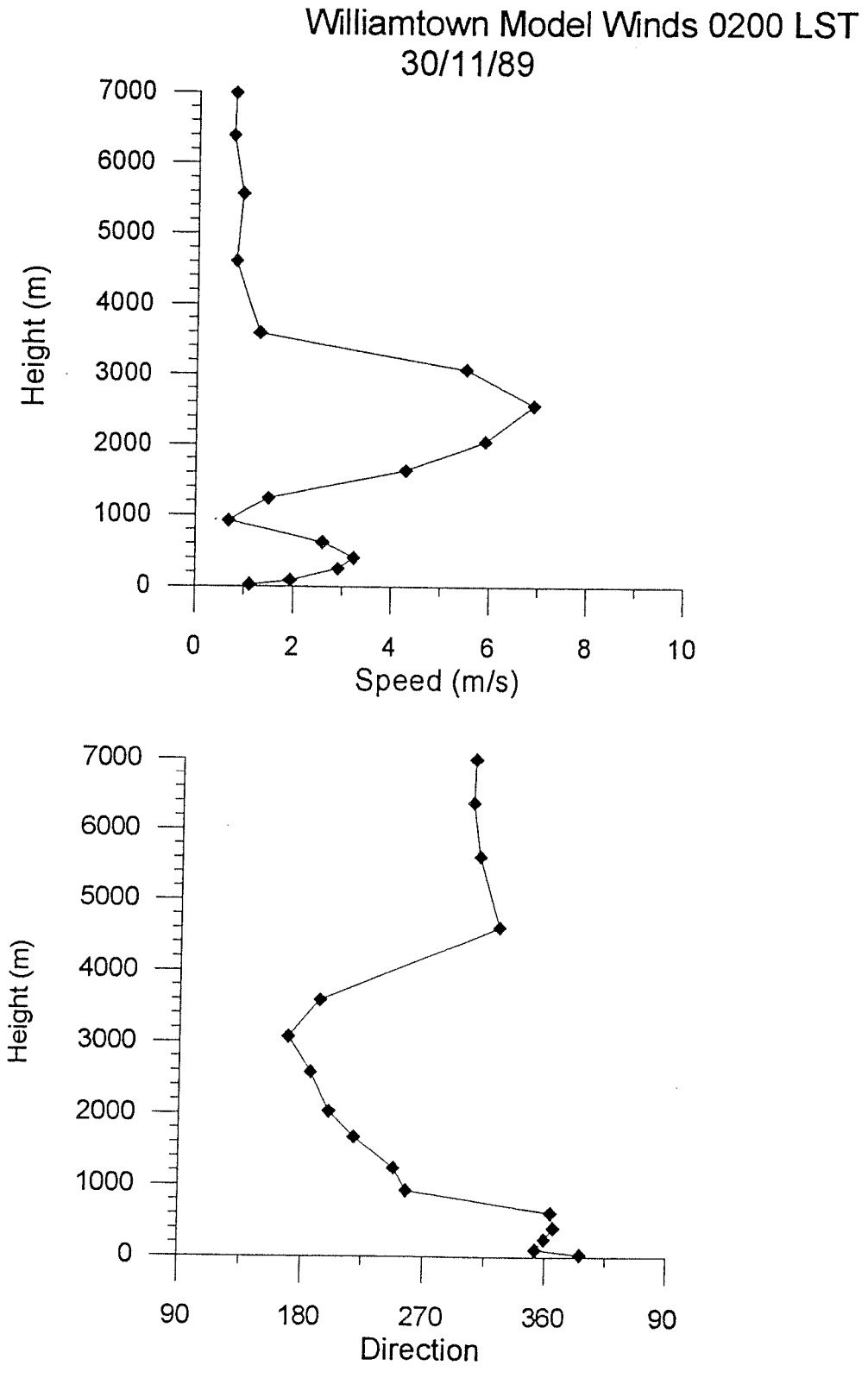

Figure 4.13: Modelled wind speed and direction profiles at 0200 LST above the gridpoint corresponding to Williamtown. Compare with observations in Fig.4.9.

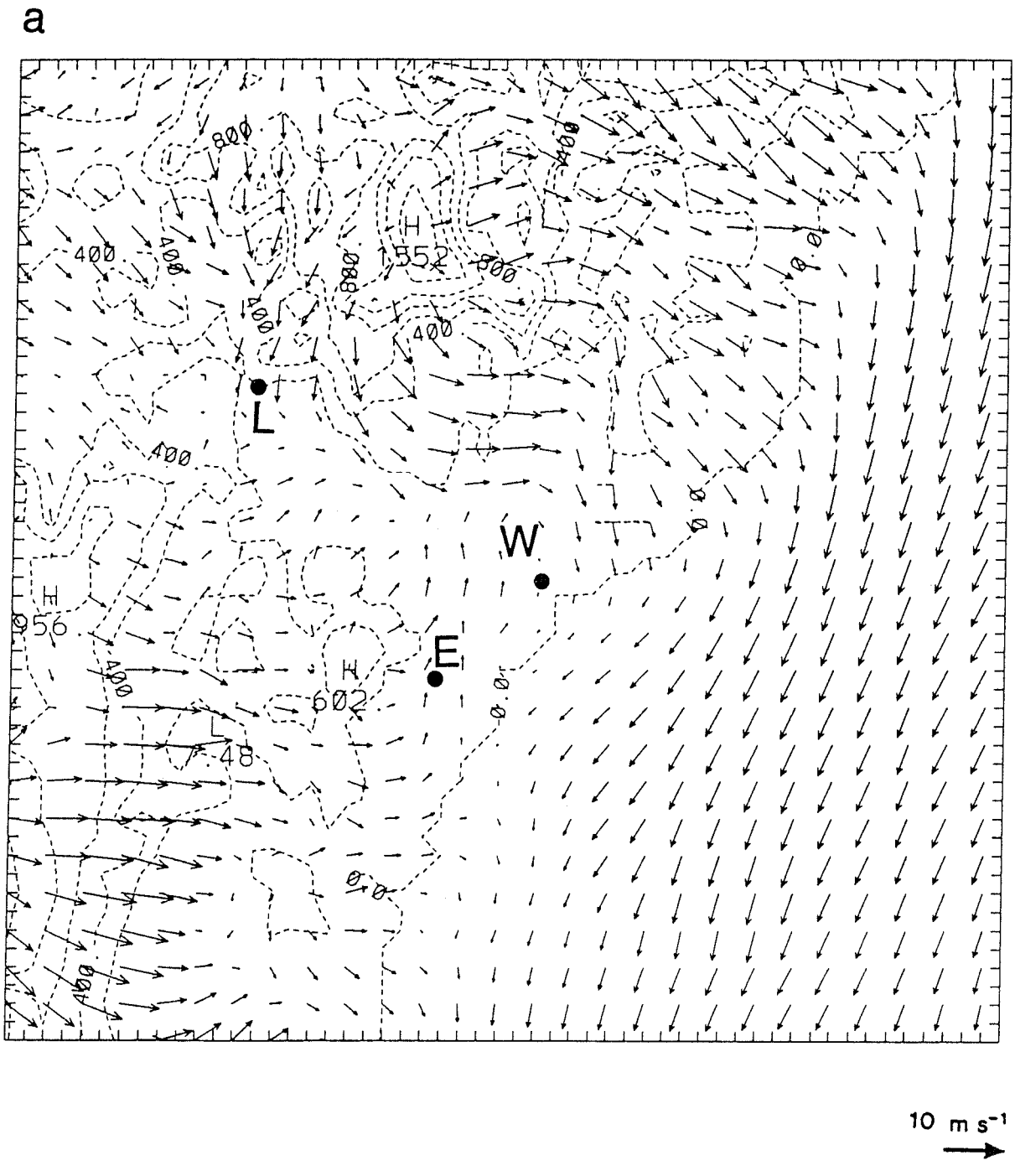

Figure 4.14 (a): Modelled windfield at 0400 LST at a height of approximately 30 m above the ground. Arrows denote strength and direction of horizontal winds. Tick mark interval represents a distance of 5 km.

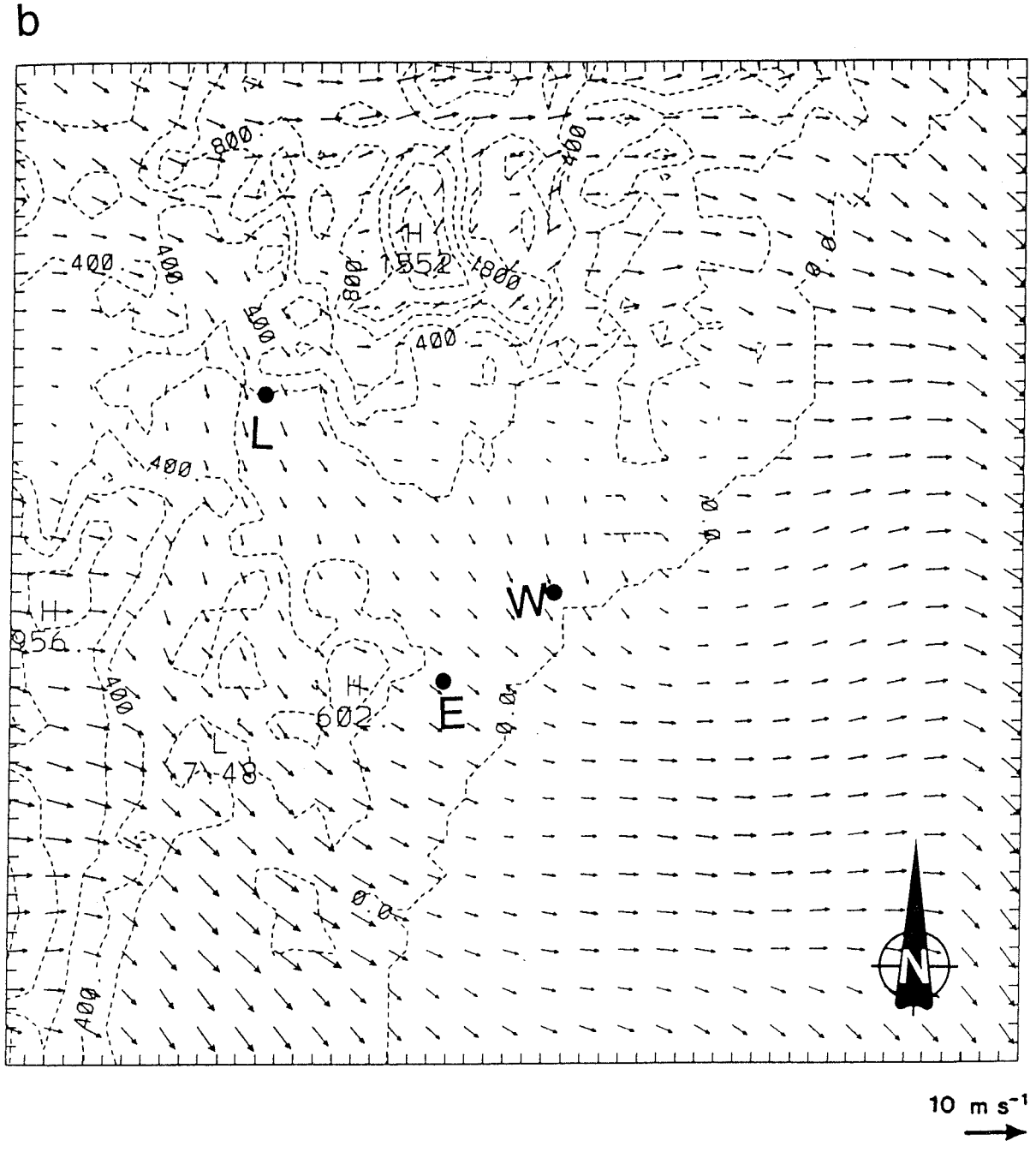

Figure 4.14 (b): Modelled windfield at 0400 LST at a height of approximately 600 m above the ground. Arrows denote strength and direction of horizontal winds. Tick mark interval represents a distance of 5 km.

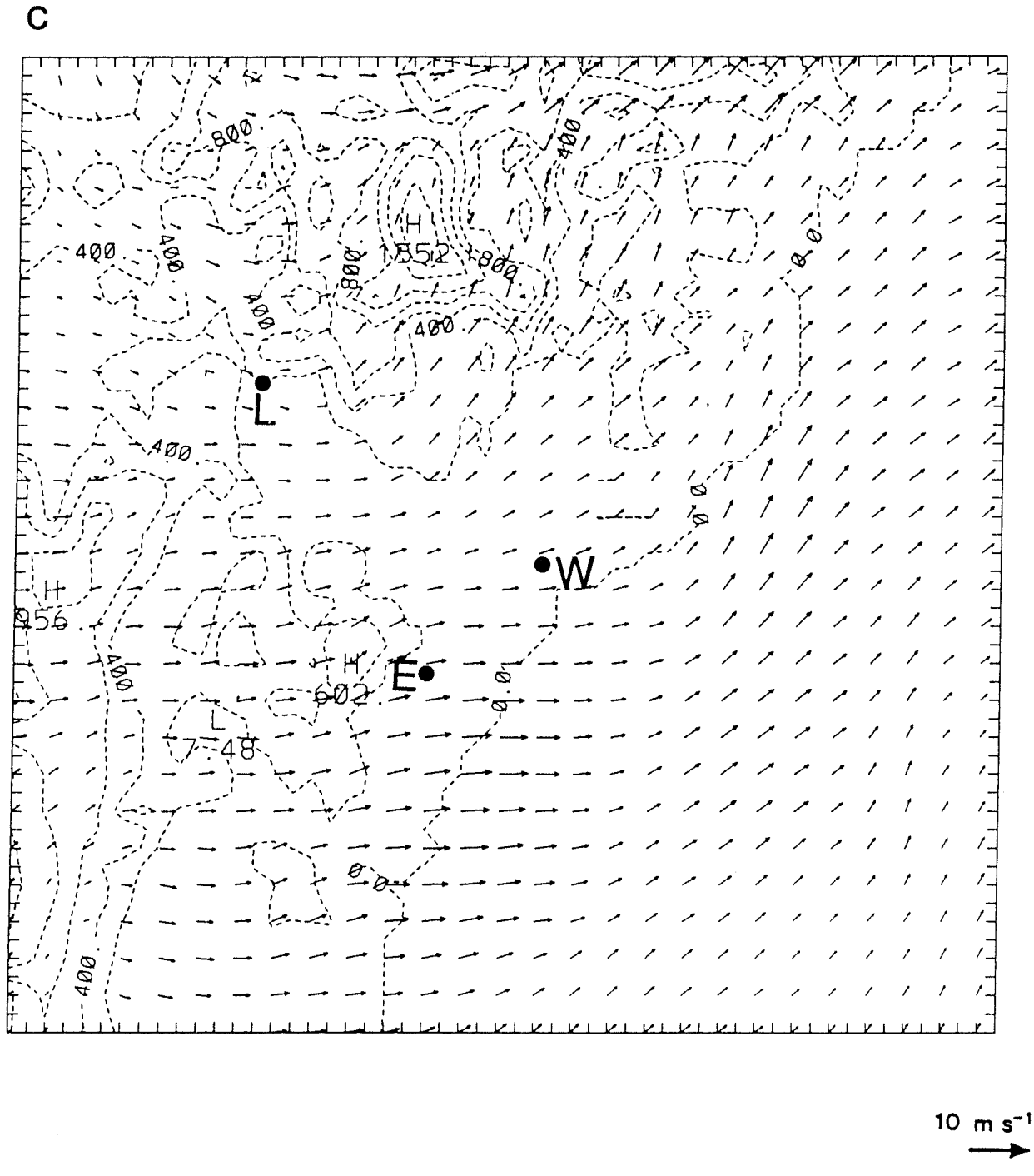

Figure 4.14 (c): Modelled windfield at 0400 LST at a height of approximately 1200 m above the ground. Arrows denote strength and direction of horizontal winds. Tick mark interval represents a distance of 5 km.

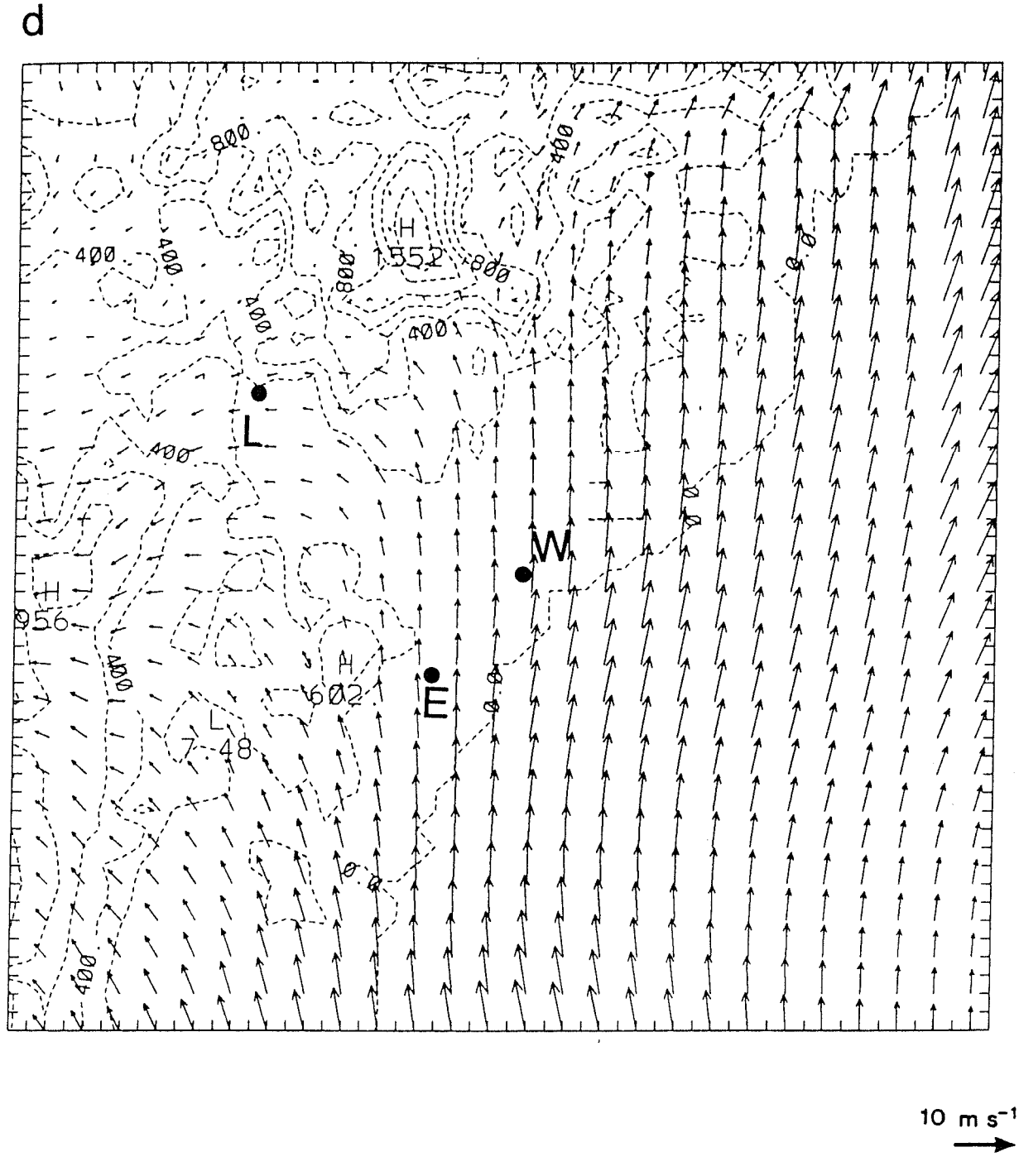

Figure 4.14 (d): Modelled windfield at 0400 LST at a height of approximately 2400 m above the ground. Arrows denote strength and direction of horizontal winds. Tick mark interval represents a distance of 5 km.

4.3.3 Predicted wind behaviour over a diurnal cycle

The light night-time winds simulated for the Liddell area become northwesterly and strengthen at about 0500 LST, in good agreement with the surface wind observations (Fig.4.11). The predicted wind profile above Liddell at 0800 and 1000 LST (Figs.4.15a,b) suggests the drainage flow is about 700 m deep with a maximum windspeed around 5 m s^{-1}. These values are consistent with profiles observed on other days at Liddell (Malfroy, ECNSW, personal communication, 1991). As the morning progresses, an up-valley pressure gradient develops, leading to a weakening of the down-valley drainage flow (Fig.4.15c) and finally to very light winds of about 1 m s^{-1} by 1300 LST (Fig.4.15d). Convective entrainment of light winds aloft also weakens the down-valley flow.

Comparison of the model results at 1100 LST (Fig.4.15c) with the observations (Fig.4.10) reveals good agreement below 1500 m, although the predicted winds are weaker than observed. The windspeed minimum and direction change at 1500 m (the top of the mixed layer) are also well simulated, but the observed south-southeasterly winds between 1500 and 2100 m are not reproduced in either strength or direction.

The 1300 LST comparison (Figs.4.15d and 4.10) shows the model has successfully simulated the very light winds throughout the boundary layer, although a west-northwesterly direction is predicted in comparison to the observed south-westerly drift. In view of the very weak winds, this is not considered a serious deficiency, especially as south-westerlies are predicted at the next gridpoint east of Liddell, where weak upslope winds are generated.

The sea breeze forms at the coast at about 1000 LST and by midday has moved approximately 30 km up the Hunter Valley (Fig.4.16a). It is 600 m deep and has a return flow which is evident at higher levels (see for example the 1200 m flow field in Fig.4.16b). This return flow is always from the southwest quadrant, rather than the northwest which is normal to the coast, due probably to the mountains parallel to the coastline. Corroboration of the sea-breeze position at this time comes from the aircraft flight of Carras and Williams, who intercepted the sea breeze while flying at 600 m near Cessnock, 30 km from the coastline (Carras, CSIRO, personal communication, 1991). Also evident in Fig.4.16a are upslope winds on both sides of the Hunter Valley and

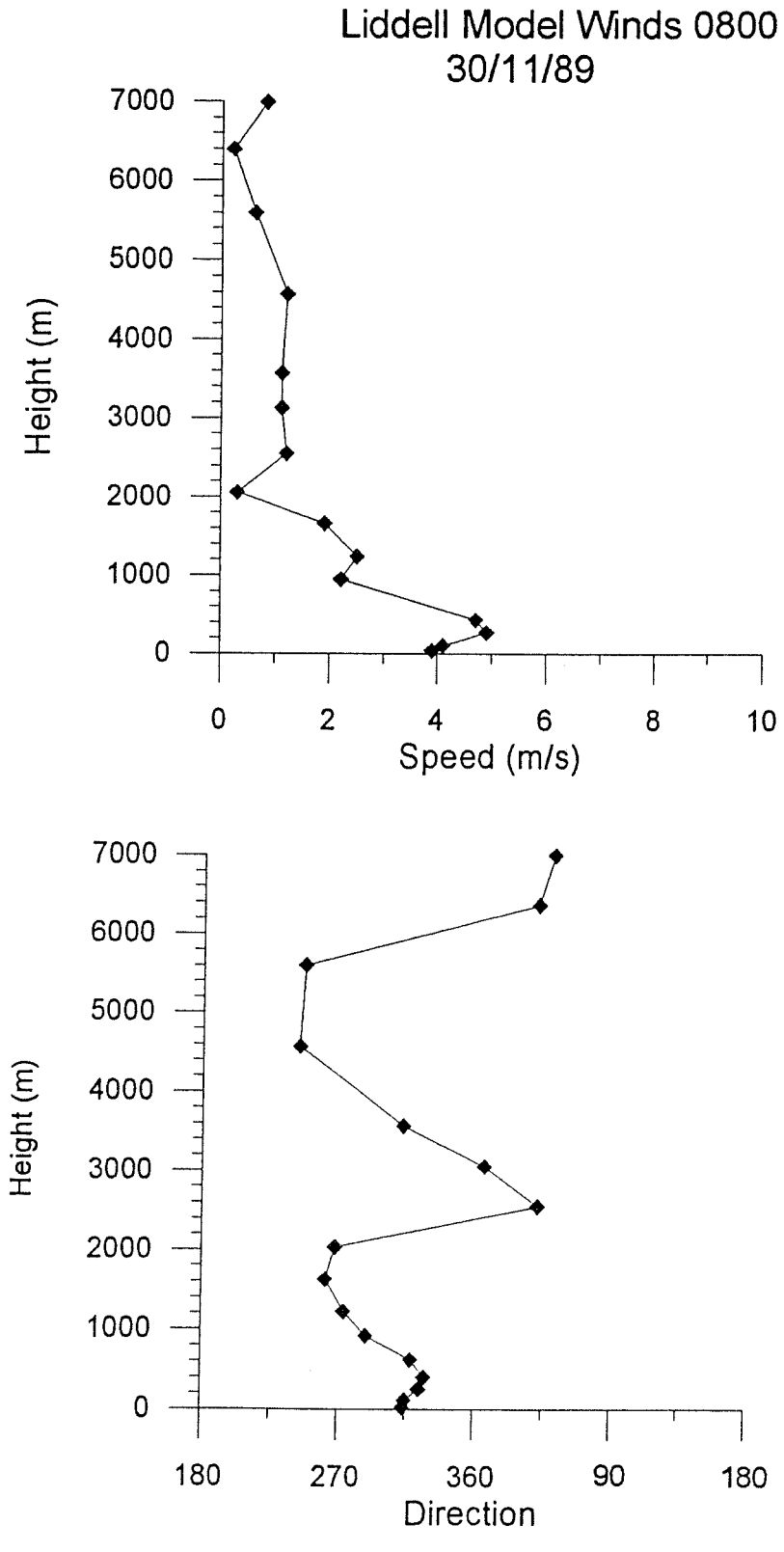

Figure 4.15 (a): Modelled windspeed and direction profile at the Liddell gridpoint at 0800 LST.

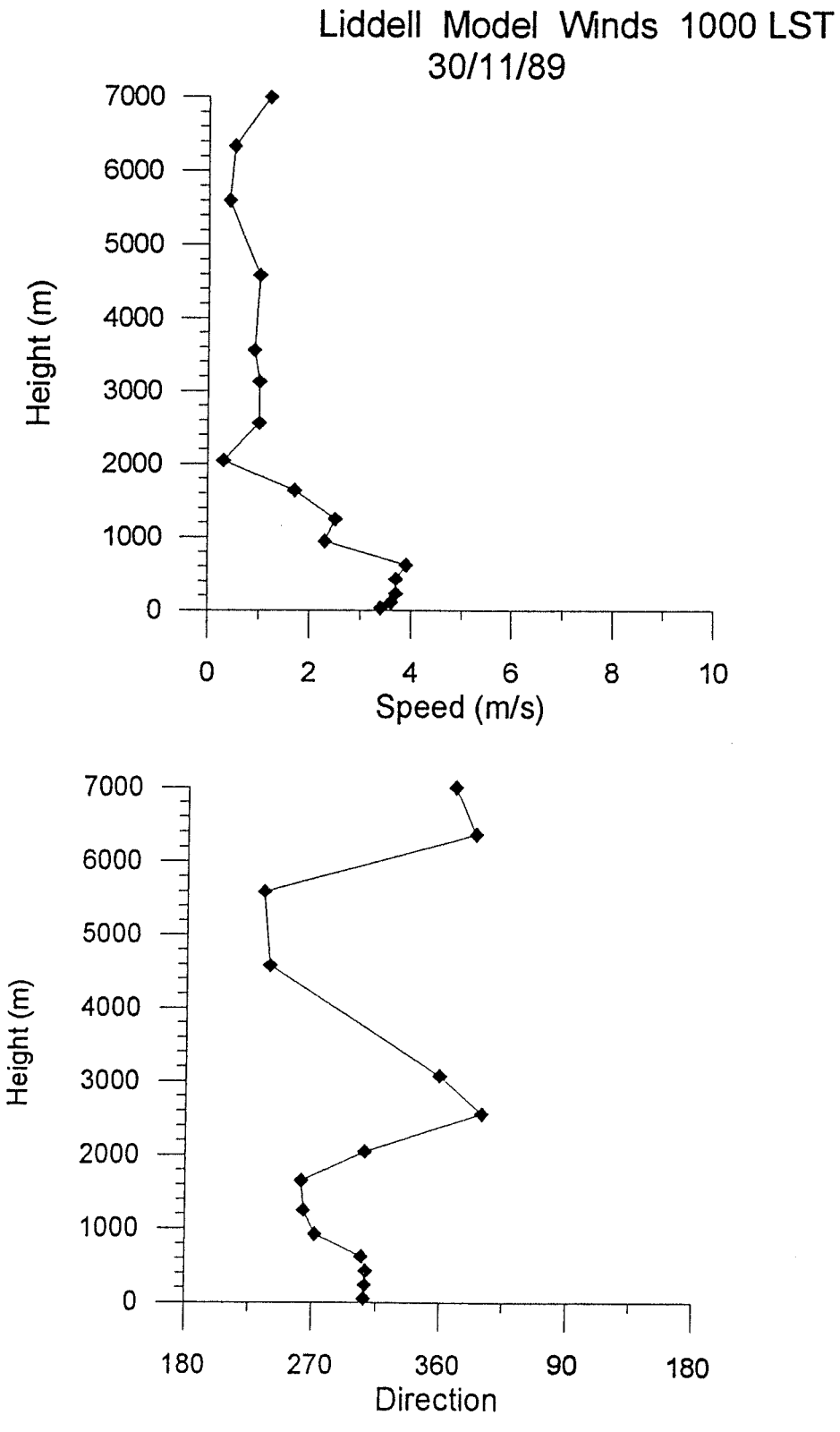

Figure 4.15 (b): Modelled windspeed and direction profile at the Liddell gridpoint at 1000 LST.

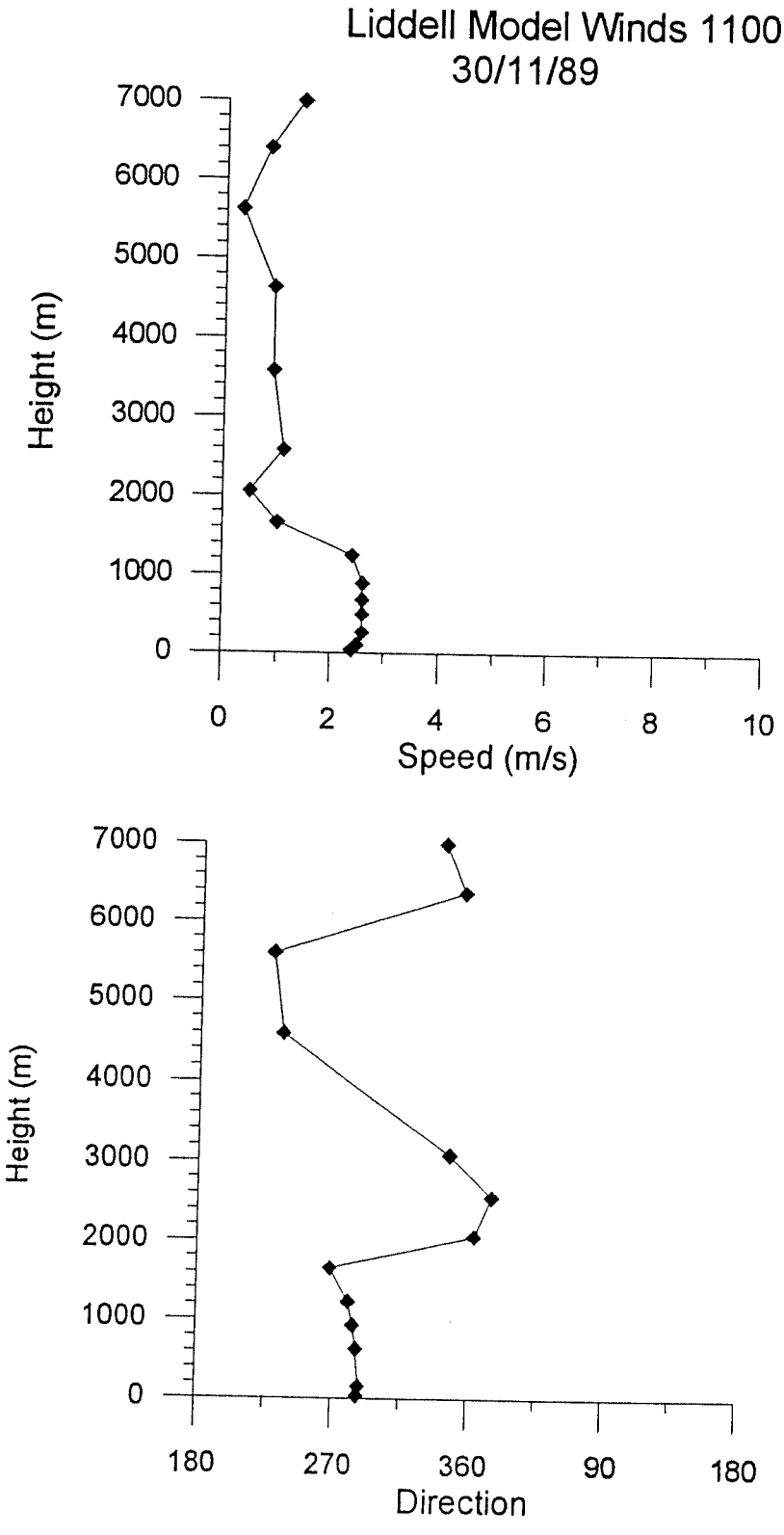

Figure 4.15 (c): Modelled windspeed and direction profile at the Liddell gridpoint at 1100 LST.

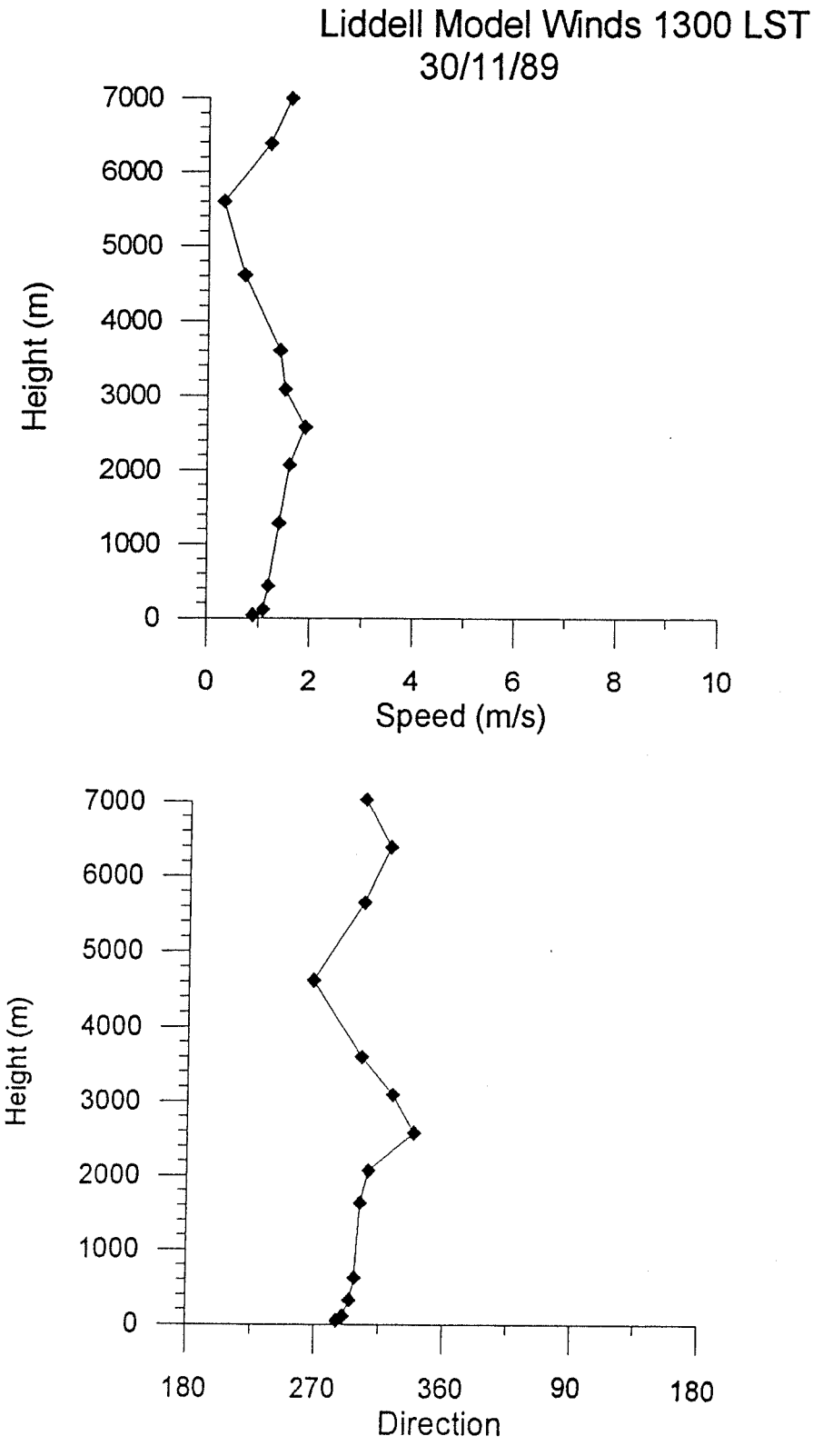

Figure 4.15 (d): Modelled windspeed and direction profile at the Liddell gridpoint at 1300 LST.

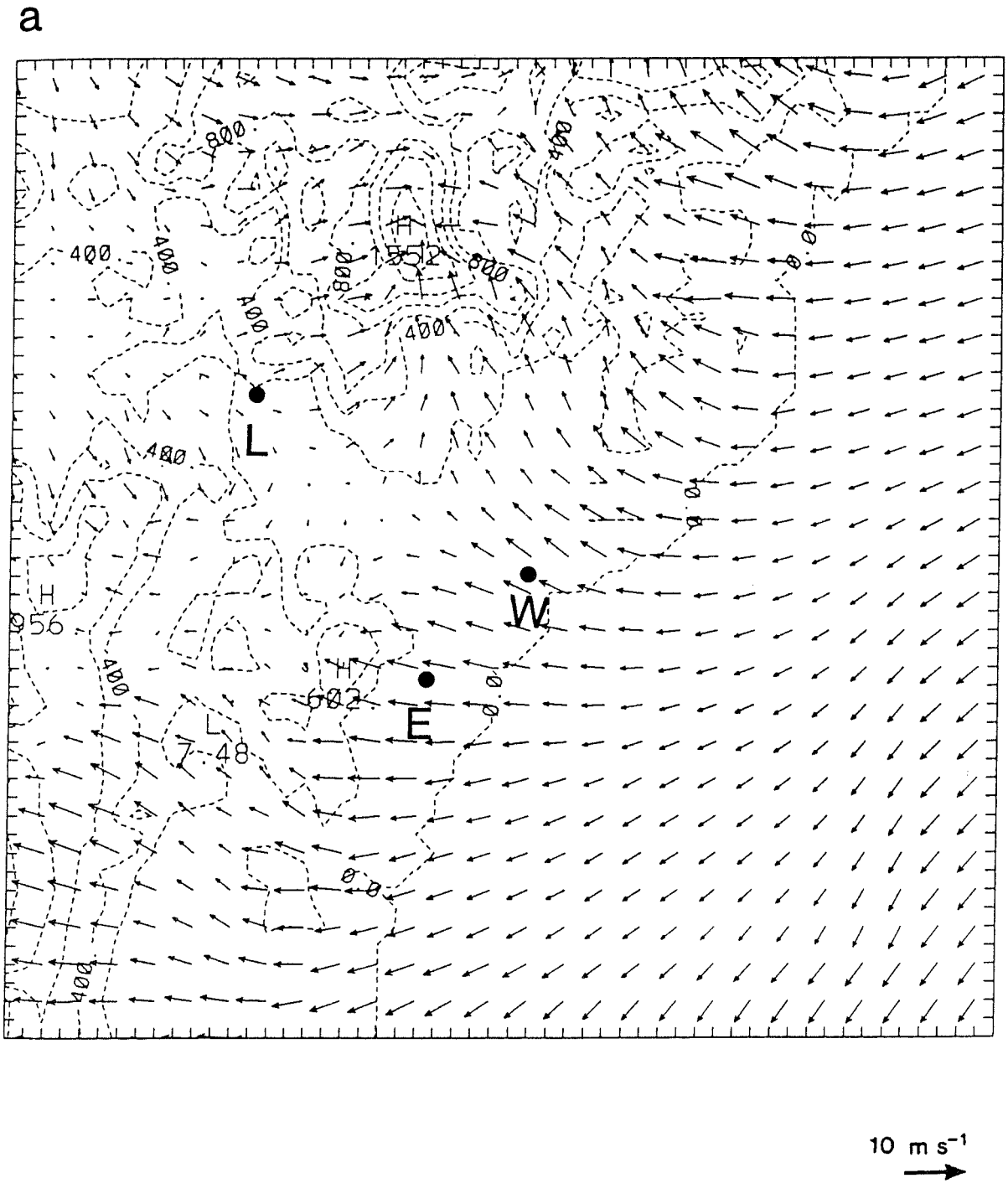

Figure 4.16 (a): Modelled windfield at 1200 LST at a height of approximately 30 m above the ground. Arrows denote strength and direction of horizontal winds. Tick mark interval represents a distance of 5 km.

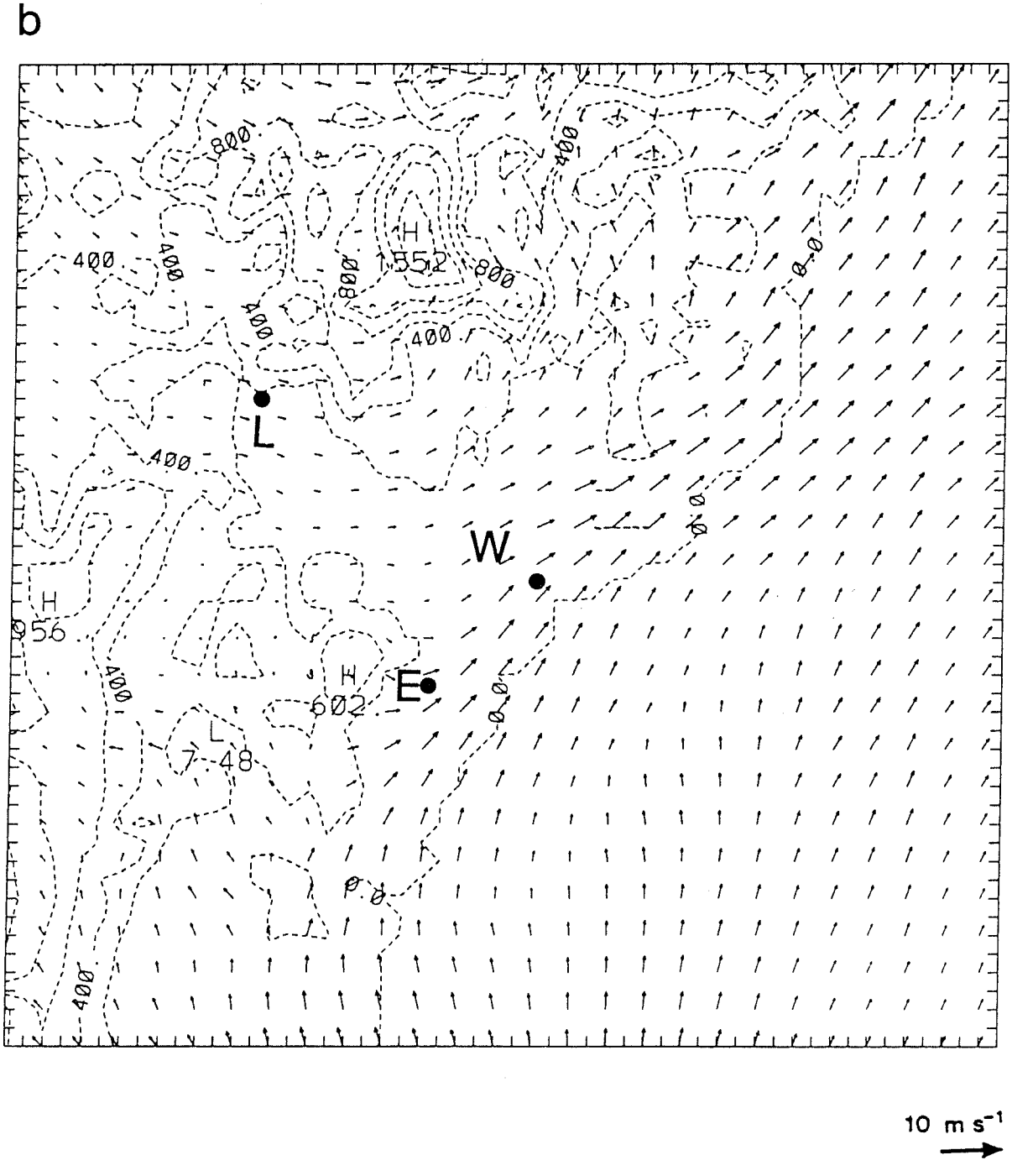

Figure 4.16 (b): Modelled windfield at 1200 LST at a height of approximately 1200 m above the ground. Arrows denote strength and direction of horizontal winds. Tick mark interval represents a distance of 5 km.

on the mountain slopes further north and south of the Valley. The strong influence of the sea breeze on the windfield in the coastal region can be seen in the modelled profile above the Williamtown gridpoint at 1400 LST (Fig.4.17), where the sea breeze inflow and return flow are evident in both windspeed and direction profiles. These values are in excellent agreement with the winds from the 1400 EST Williamtown sonde ascent (Fig.4.9c,d).

By 1600 LST, the sea breeze has moved well up the Hunter Valley where it is from the southeast quadrant, in contrast to the northeasterly direction at the coastline (Fig.4.18a). This is a well-known characteristic of the regional sea breeze (Hyde et al., 1981). It is deeper (about 900 m) than at midday and in the Blue Mountains region is indistinguishable from the upslope winds. In the lower levels, the wind direction change with height at Eraring (Figs.4.18a,b) is consistent with the acoustic sounder data (Fig.4.8b), and the predicted maximum speed of 7 m s^{-1} at 250 m agrees well with the observed speed (Fig.4.8a). The sea breeze arrives at Liddell soon after 1700 LST, about one and a half hours earlier than the observed time, although within the range of onset times tabulated by Hyde et al. (1981) for the November-December period. Winds are from east-southeast at about 5 m s^{-1} at the 30 m level, consistent with the 10 m observations (Fig.4.11).

Observations of upper winds at night are available only in the coastal region, at Williamtown. Profiles at 2000 EST (Fig.4.9c,d) show, in both arms of the circulation, a strengthening of the winds since the 1400 EST ascent. Winds below 1000 m have backed to become more northerly, while the return flow between 2000 and 3000 m has veered to a south-westerly direction. The modelled winds for Williamtown (Fig.4.19) also show these characteristics, apart from the veering at upper levels. The observed windspeed at these heights is also greater than predicted.

By 2200 LST, a stable boundary layer has developed near the ground and flow in the lower levels has largely decoupled from the winds above (Figs.4.20a,b). West of Liddell the sea breeze is still evident, but elsewhere inland the flow is responding to local orographic features. At the 600 m level (Fig.4.20c) the sea-breeze remnants can be seen as a northeast-quadrant flow over most of the domain.

In the coastal region at 2200 LST, Coriolis turning of the sea breeze has resulted in a general northerly flow at all levels below 1000 m

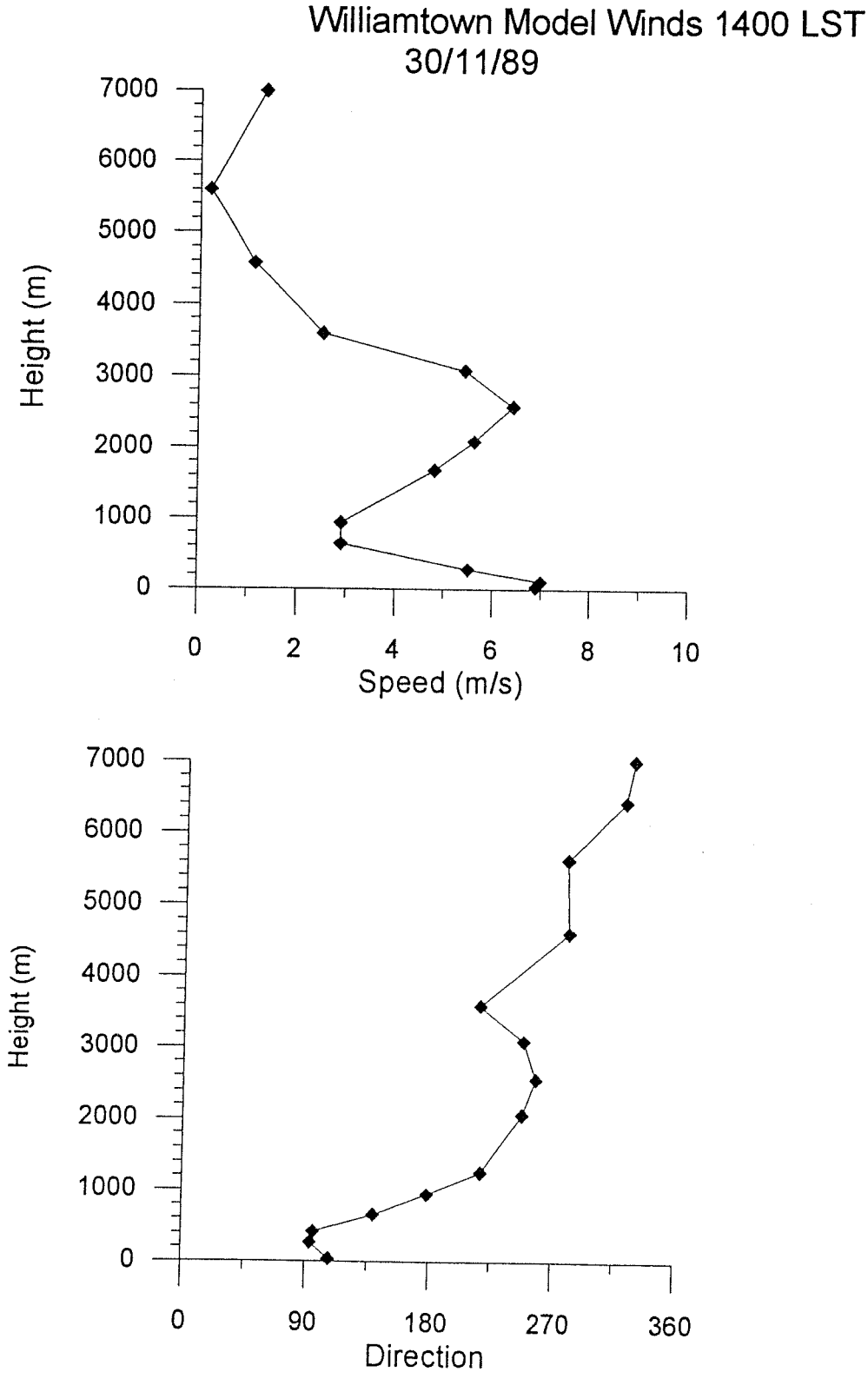

Figure 4.17: Modelled windspeed and direction profile at the Williamtown gridpoint at 1400 LST. Compare with observations in Fig.4.9.

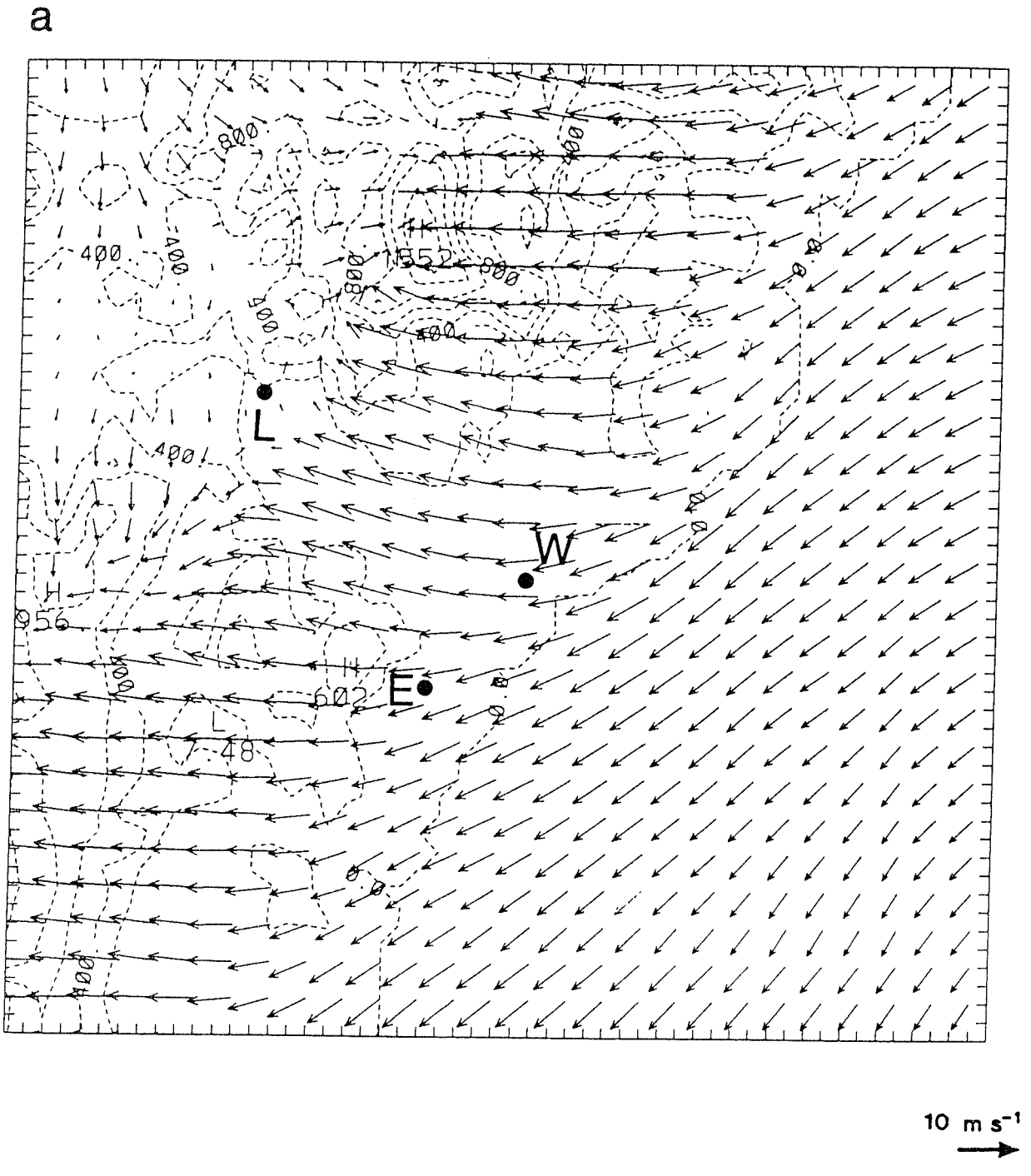

Figure 4.18 (a): Modelled windfield at 1600 LST at a height of approximately 30 m above the ground. Arrows denote strength and direction of horizontal winds. Tick mark interval represents a distance of 5 km.

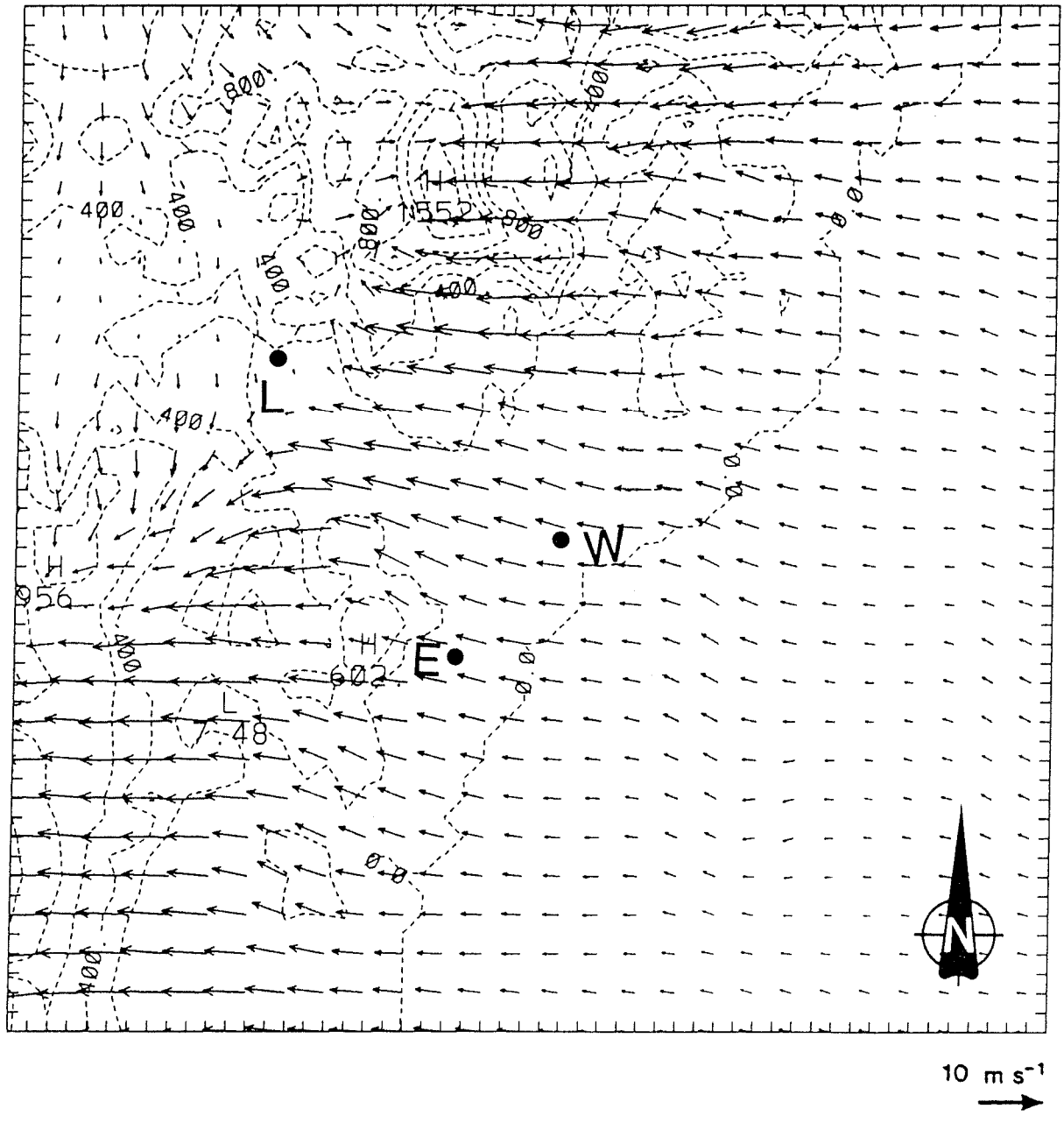

Figure 4.18 (b): Modelled windfield at 1600 LST at a height of approximately 600 m above the ground. Arrows denote strength and direction of horizontal winds. Tick mark interval represents a distance of 5 km.

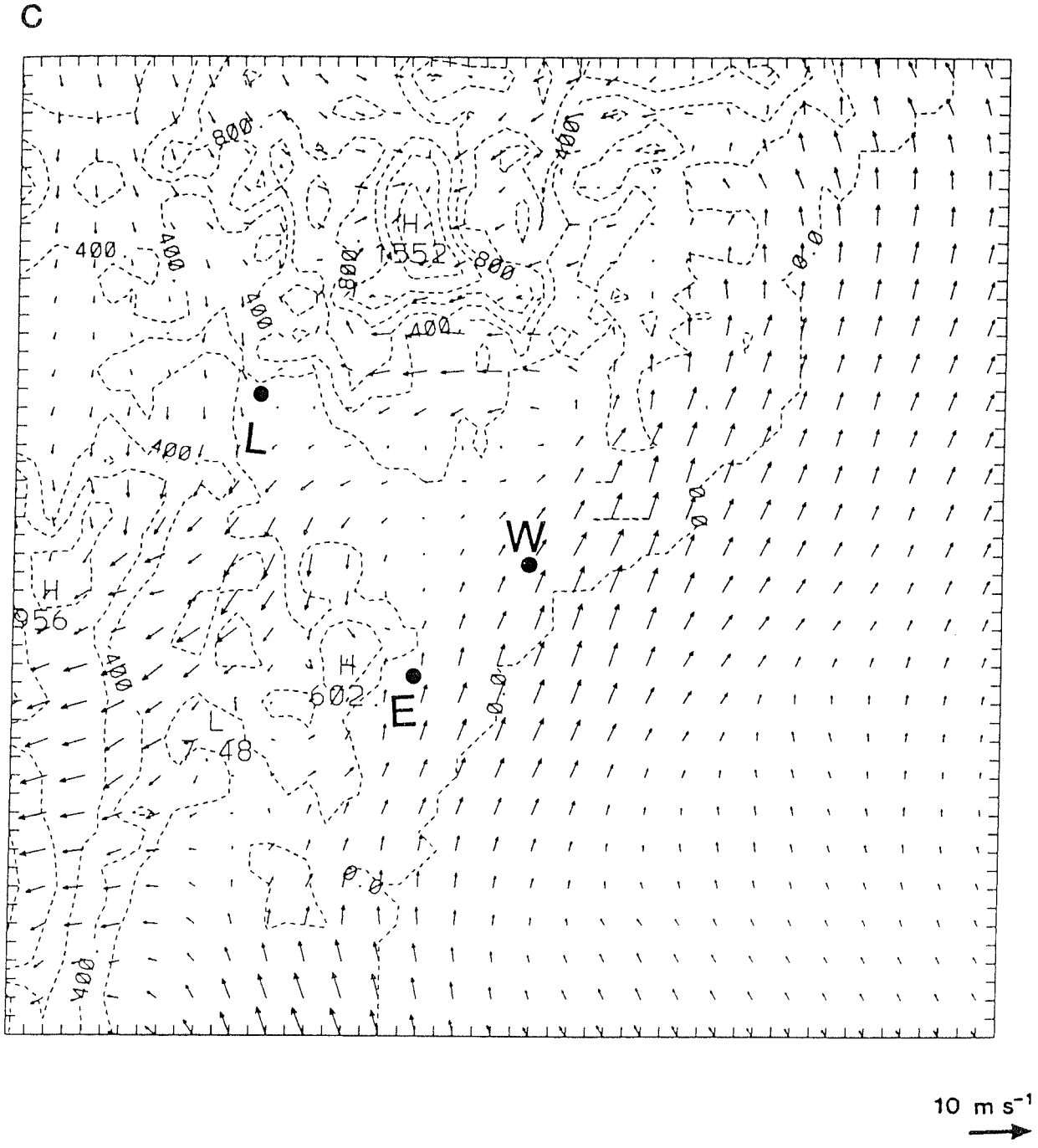

Figure 4.18 (c): Modelled windfield at 1600 LST at a height of approximately 1200 m above the ground. Arrows denote strength and direction of horizontal winds. Tick mark interval represents a distance of 5 km.

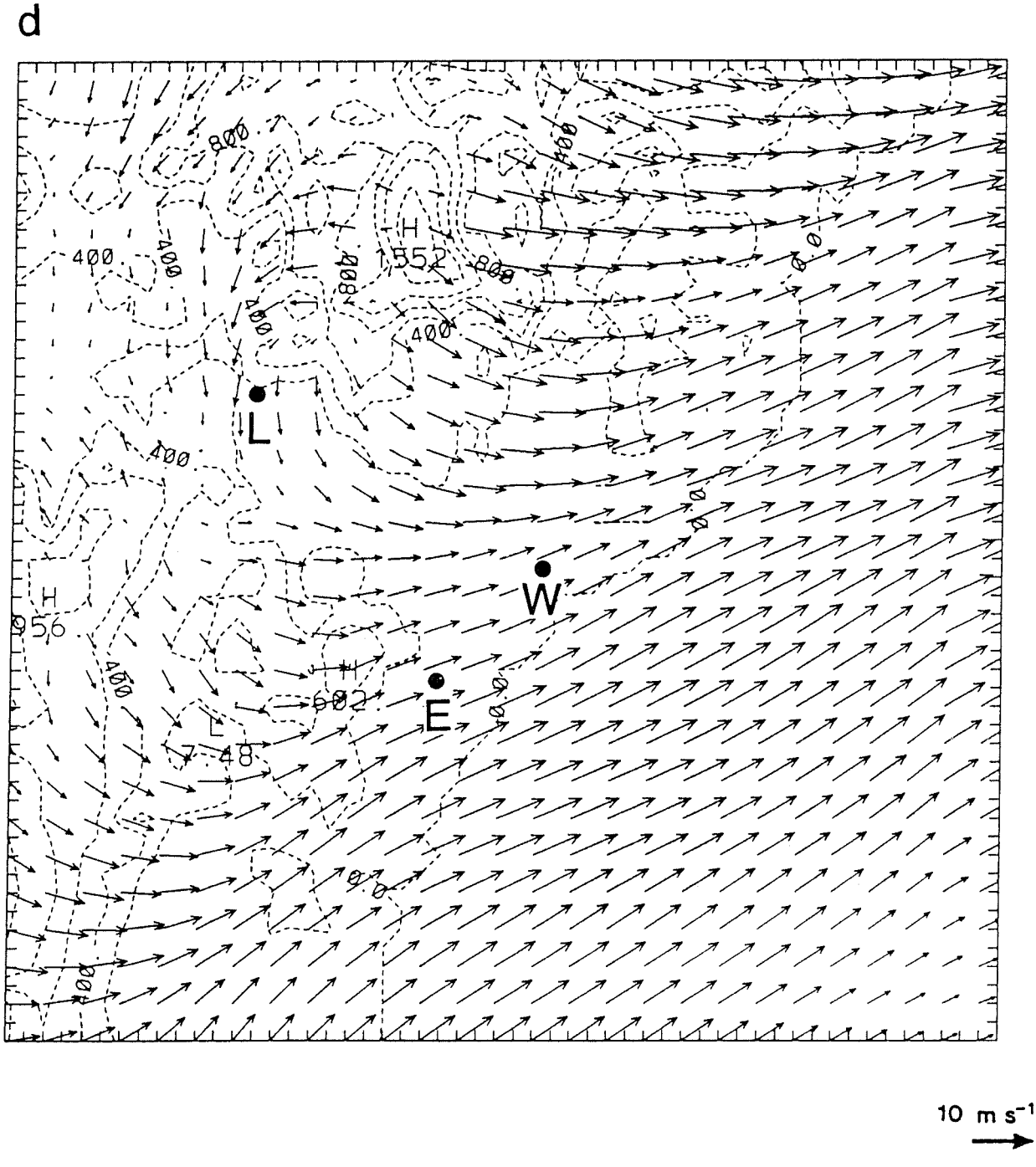

Figure 4.18 (d): Modelled windfield at 1600 LST at a height of approximately 2400 m above the ground. Arrows denote strength and direction of horizontal winds. Tick mark interval represents a distance of 5 km.

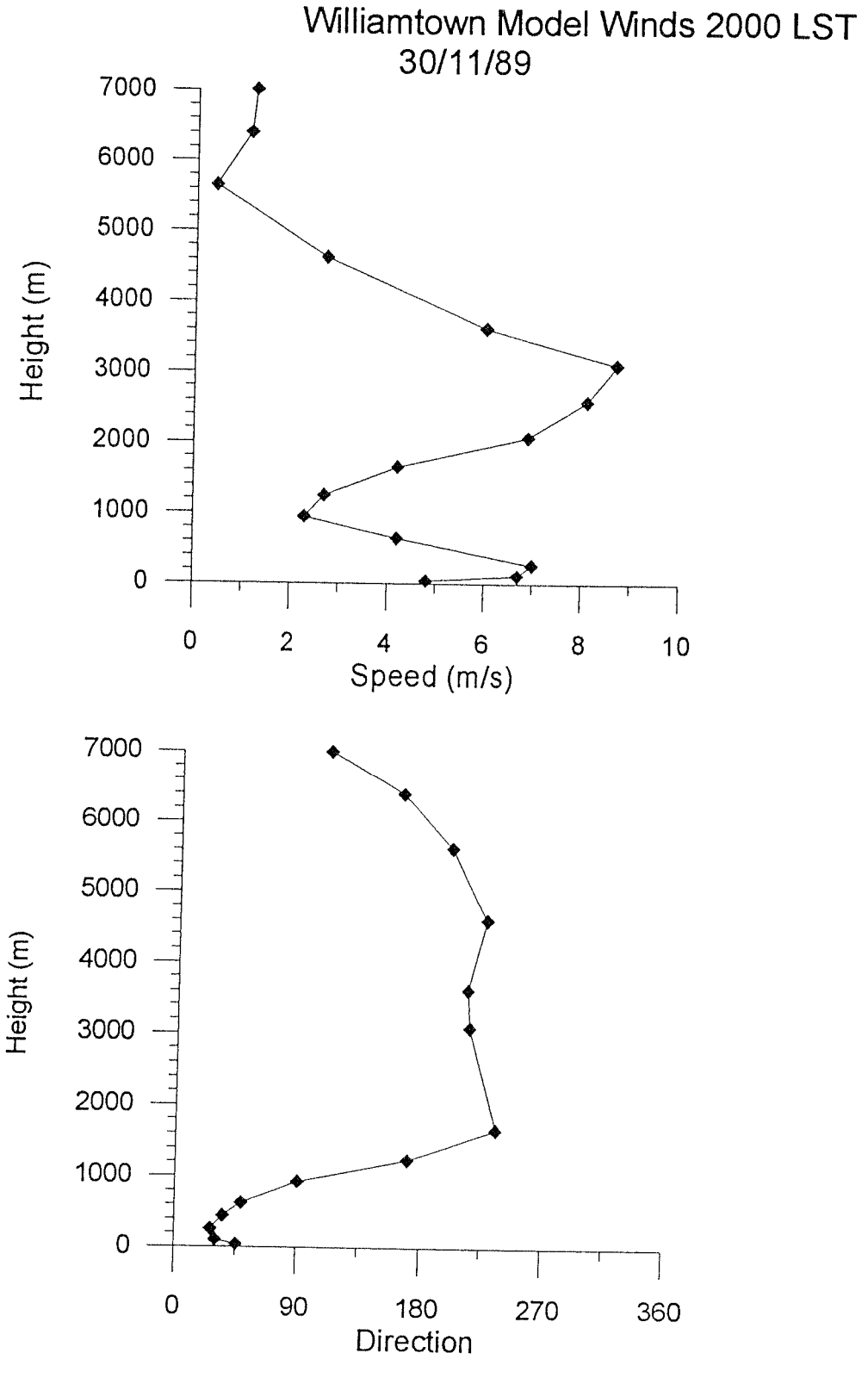

Figure 4.19: Modelled windspeed and direction profile at the Williamtown gridpoint at 2000 LST.

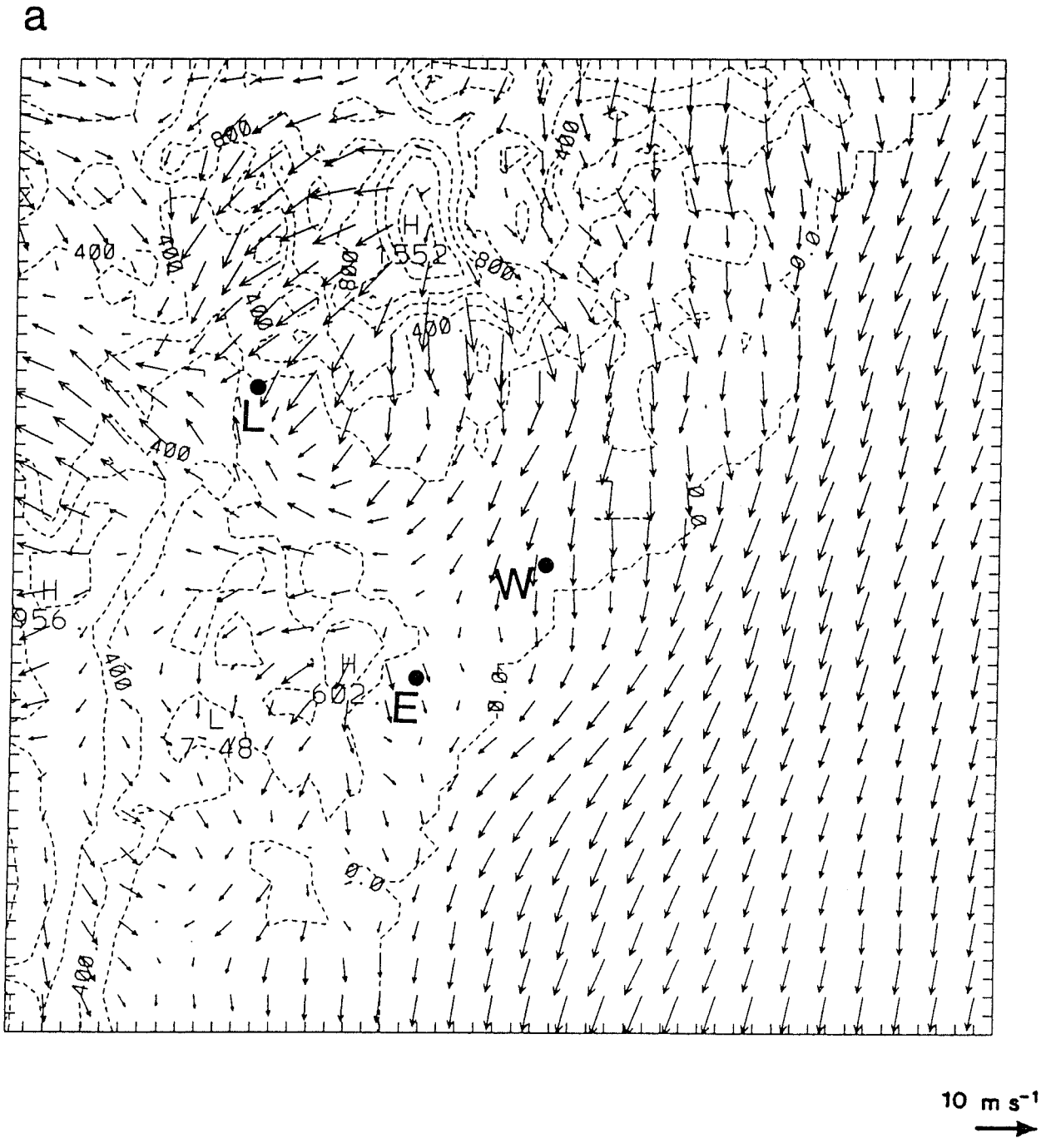

Figure 4.20 (a): Modelled windfield at 2200 LST at a height of approximately 30 m above the ground. Arrows denote strength and direction of horizontal winds. Tick mark interval represents a distance of 5 km.

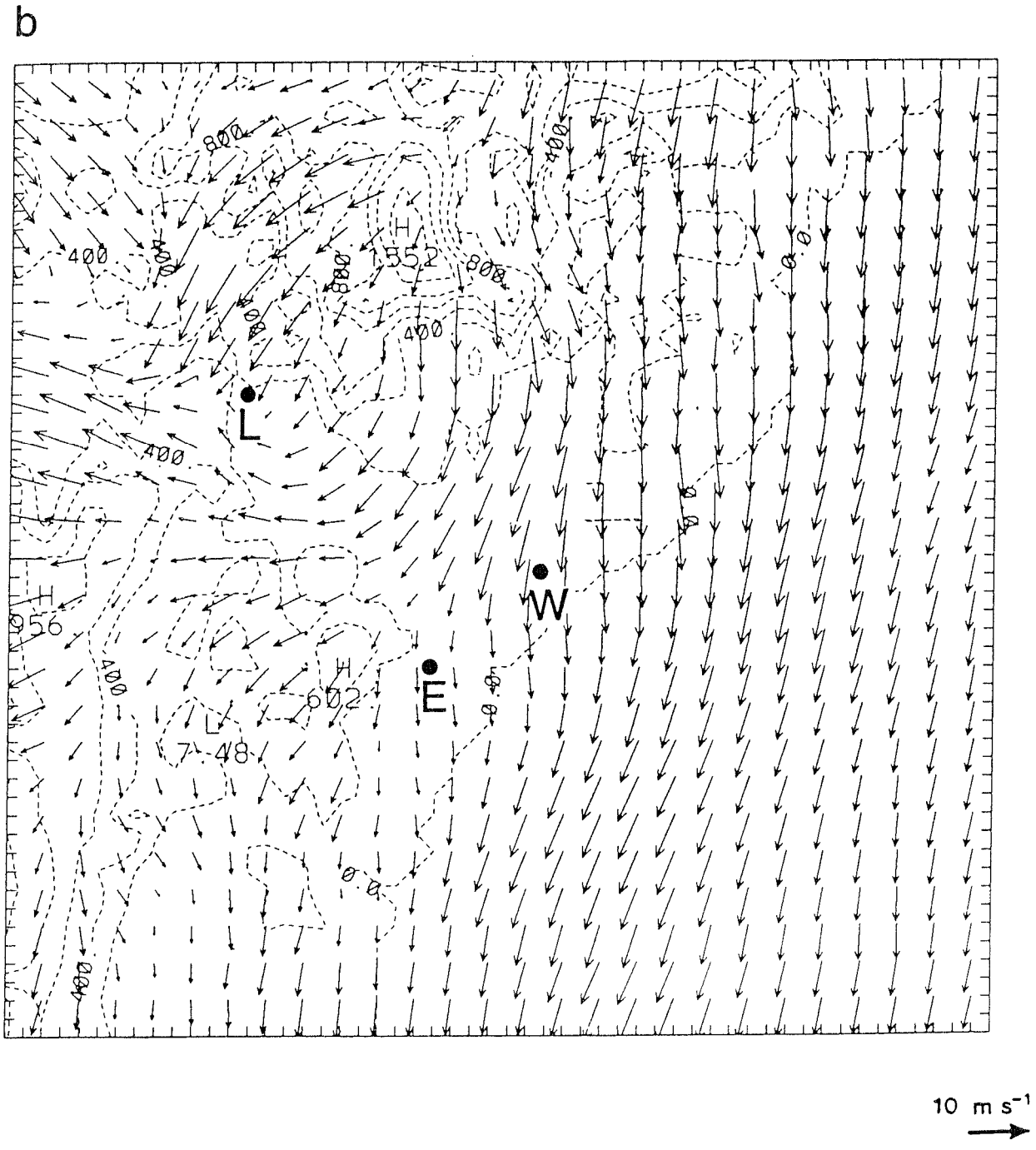

Figure 4.20 (b): Modelled windfield at 2200 LST at a height of approximately 100 m above the ground. Arrows denote strength and direction of horizontal winds. Tick mark interval represents a distance of 5 km.

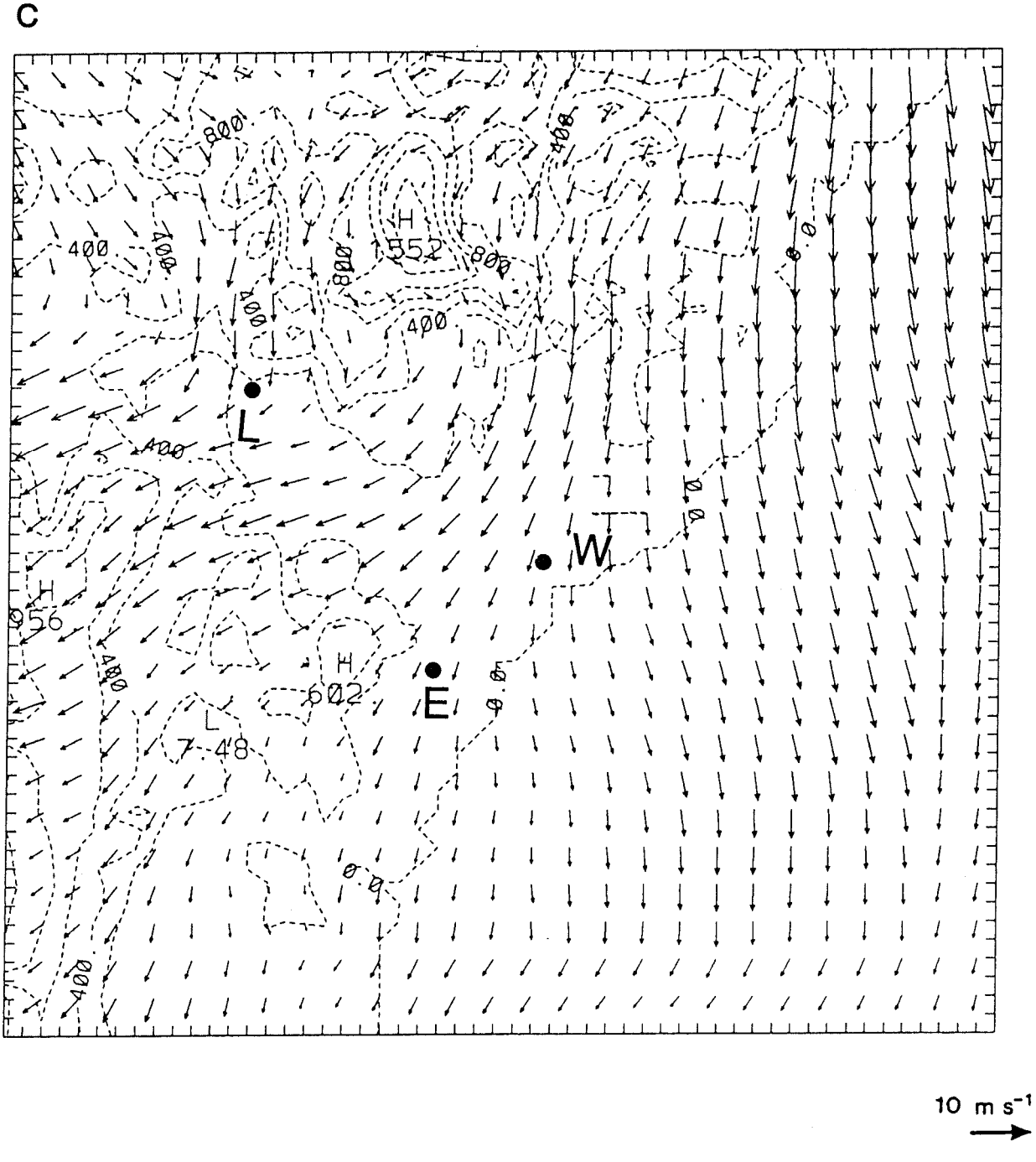

Figure 4.20 (c): Modelled windfield at 2200 LST at a height of approximately 600 m above the ground. Arrows denote strength and direction of horizontal winds. Tick mark interval represents a distance of 5 km.

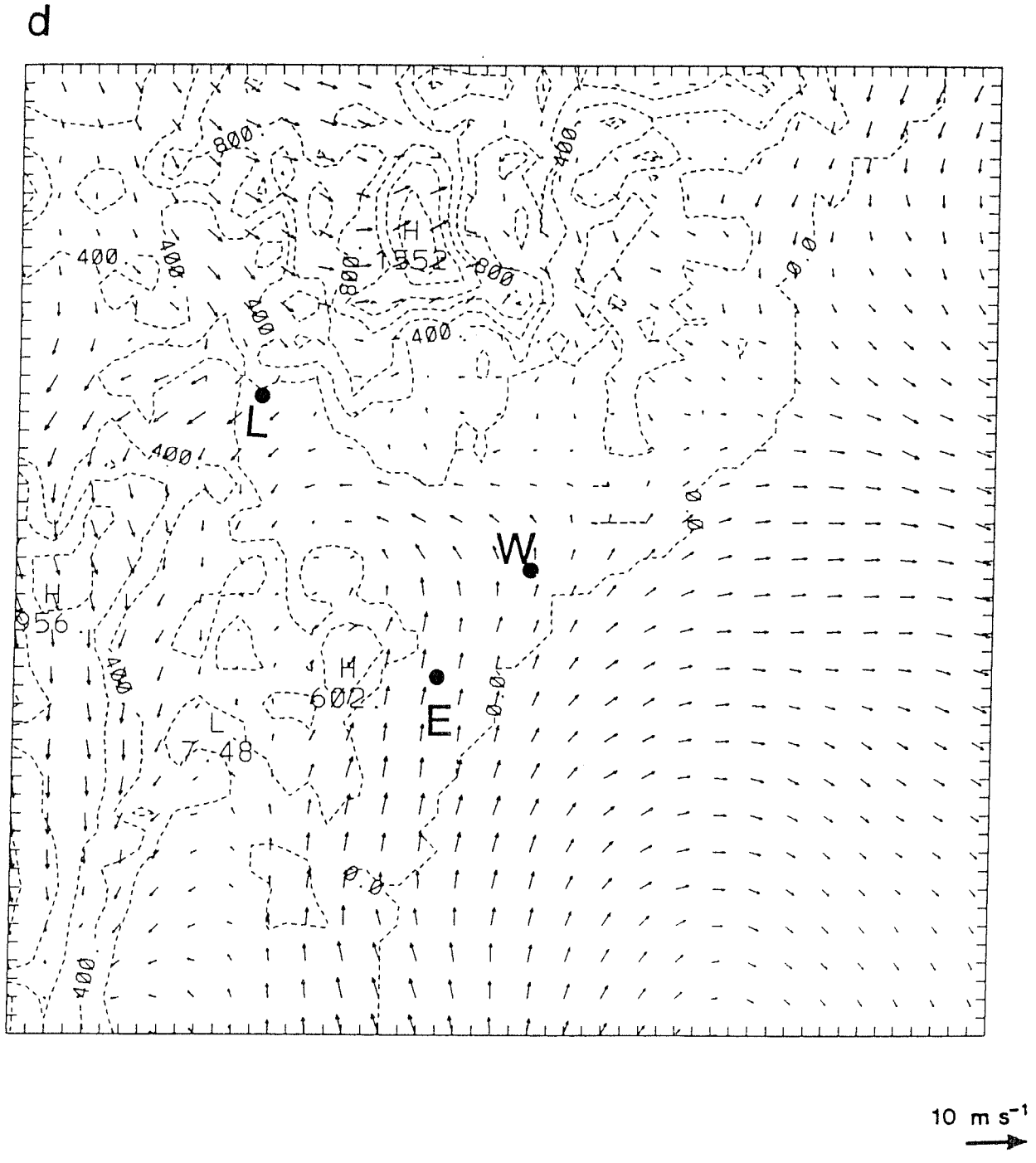

Figure 4.20 (d): Modelled windfield at 2200 LST at a height of approximately 1200 m above the ground. Arrows denote strength and direction of horizontal winds. Tick mark interval represents a distance of 5 km.

(Figs.4.20a-c). This direction agrees well with the acoustic sounder data from Eraring (Fig.4.8b), but the predicted strength of the jet is only half of the observed speed of 14 m s^{-1} (Fig.4.8a), although further north such speeds are approached. It is possible this deficiency arises from the model's inability to resolve the Lakes area, discussed earlier in Section 4.3.2.

At the 1200 m level (Fig.4.20d), complex flow patterns result from the various depths of the sea-breeze circulations in different regions. Winds between 1500 and 3500 m are southerly and reach speeds greater than 10 m s^{-1} in the coastal region (see Fig.4.19 for the Williamtown location), but become much weaker inland in a similar manner to the 0400 LST winds shown in Fig.4.14d.

4.3.4 Assessment of windfield modelling

In Sections 4.3.2 and 4.3.3, we have shown that the dominant features of the windfield on 30 November 1989 (see Section 4.3.1) have been satisfactorily reproduced by the prognostic model. However, low-level winds in stable conditions, and in particular the nocturnal jet, were not well simulated in the Lake Macquarie region and it is thought that this may be due to the small-scale features of the lakes not being resolved. This is not a serious problem for this study of emitters in the Upper Hunter Valley, and we believe the modelled winds and turbulence are sufficiently valid to apply to a study of plume dispersion on this day.

4.4 Plume dispersion modelling in the Hunter Valley region

Starting at 0400 LST, particles are released each timestep from the Bayswater and Liddell sources, at a height and distance downwind computed by the plume-rise module (Section 3.4). In accordance with the calculations of Section 3.5 for a 1000 m square sampling box, 112 particles per 20-second timestep are released from Bayswater and 40 from Liddell (no results for the near-source maxima computed with a 250 m sampling box are presented in this report). The final-rise height of the two plumes and the computed planetary boundary layer height (PBL) at each location throughout the day are shown in Fig.4.21. The only observation of mixed-layer height on 30 November is from the 1100 EST airsonde flight at Liddell, which shows a value of 1650 m, indicating a fast-growing and deep convective layer on this day. The

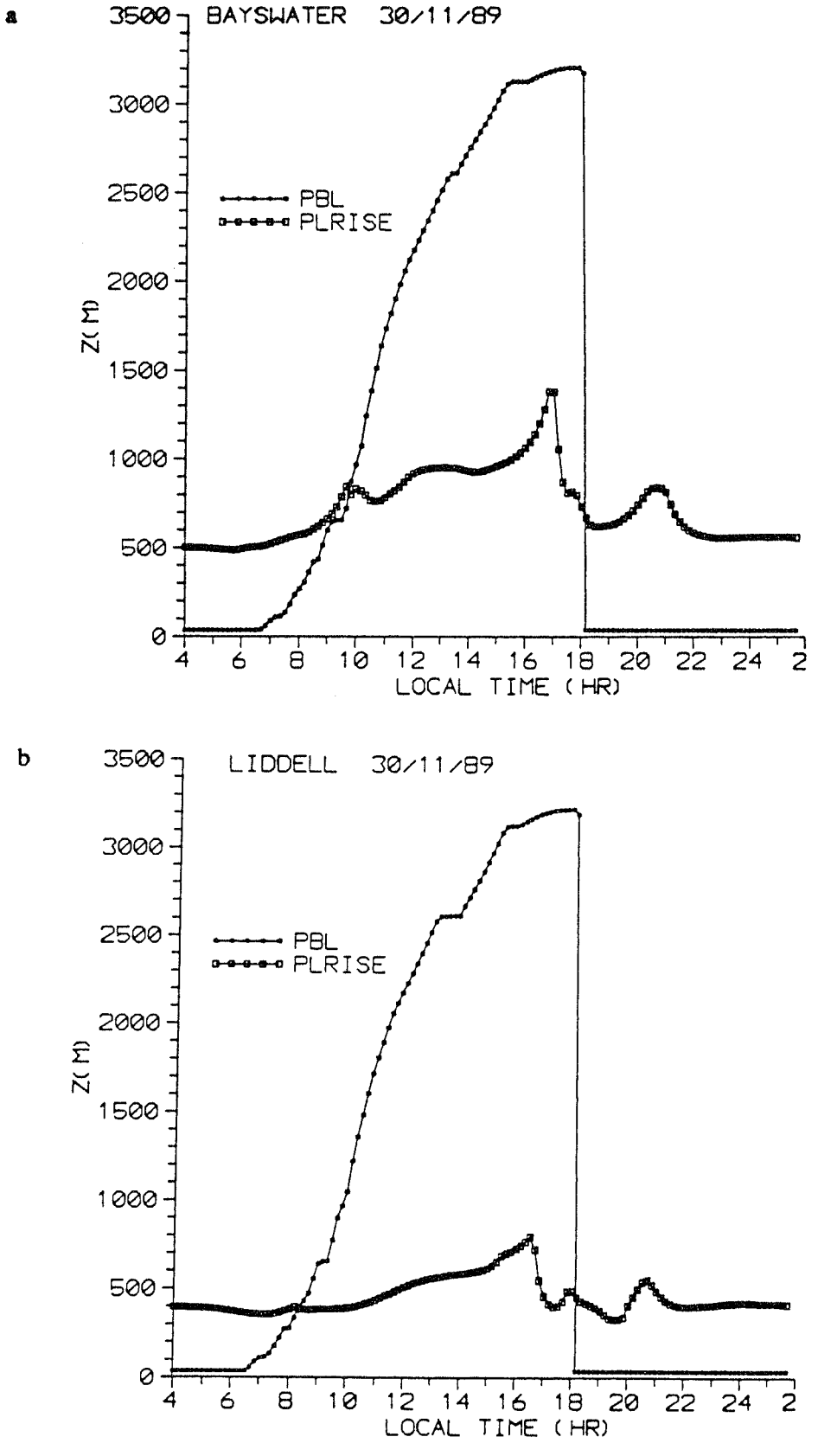

Figure 4.21: Modelled plume final-rise height and planetary boundary layer (PBL) height for 30 November 1989 at (a) Bayswater and (b) Liddell. In stable conditions, PBL height is set to 30 m, but is not used in any computations.

predicted value in Fig.4.21b is about 1750 m.

In stable conditions the Bayswater plume sits at about 500 m above the ground, while a typical value for the daytime convective conditions is around 900 m. Conceptually, this latter value is the height at which the plume is no longer recognised as an entity, having been "torn apart" by the turbulence. The lower final-rise heights above the ground for the Liddell plume reflect a shorter stack and less buoyant plume (see load curves in Fig.3.1).

The increase in final-rise height of both plumes in late afternoon is due to two factors. Firstly, winds at this time become very light (less than 1 m s^{-1}) and secondly, convective turbulence decreases as sensible heat flux at the ground weakens. The subsequent drop in plume heights near 1700 LST is a consequence of the stronger winds associated with the sea-breeze arrival. The oscillation in plume heights between 2000 and 2100 LST is due to stability fluctuations as the lower layers stabilize after sunset.

4.4.1 Plume trajectories

At 0800 LST, the drainage flow is transporting the plumes down the Hunter Valley (Fig.4.22a). The narrowness of the plumes indicates they are still in stable conditions above the convective layer. This can also be deduced from Fig.4.21. The "fuzzier" appearance of the plumes at 1000 LST (Fig.4.22b) shows that they have been entrained into the mixed layer by this time. The predicted, and observed, backing of the wind around midday brings about an overlapping of the near-stack plumes by 1300 LST (Fig.4.22c). It was at about this time that the CSIRO aircraft was flying in the Liddell region and a comparison between our predicted plumes and a preliminary analysis of the observations (Carras and Williams, CSIRO, personal communication, 1991) shows strong similarities in plume directions and widths. The predicted merging of the two plumes relatively near the stacks is also seen in the data.

During the afternoon, the very light winds below about 2000 m in the Upper Hunter region do not transport the plumes far from the stacks, but particles in the upper part of the mixed layer are transported towards the coast (Fig.4.22d). This is especially so further down the Valley where the plumes have been entrained in the return flow of the sea breeze (see for example the 1600 LST windfield at 2400 m in Fig.4.18d). The sea breeze is well inland by 1600 LST (Fig.4.18a,b) and is bringing clean air as it moves

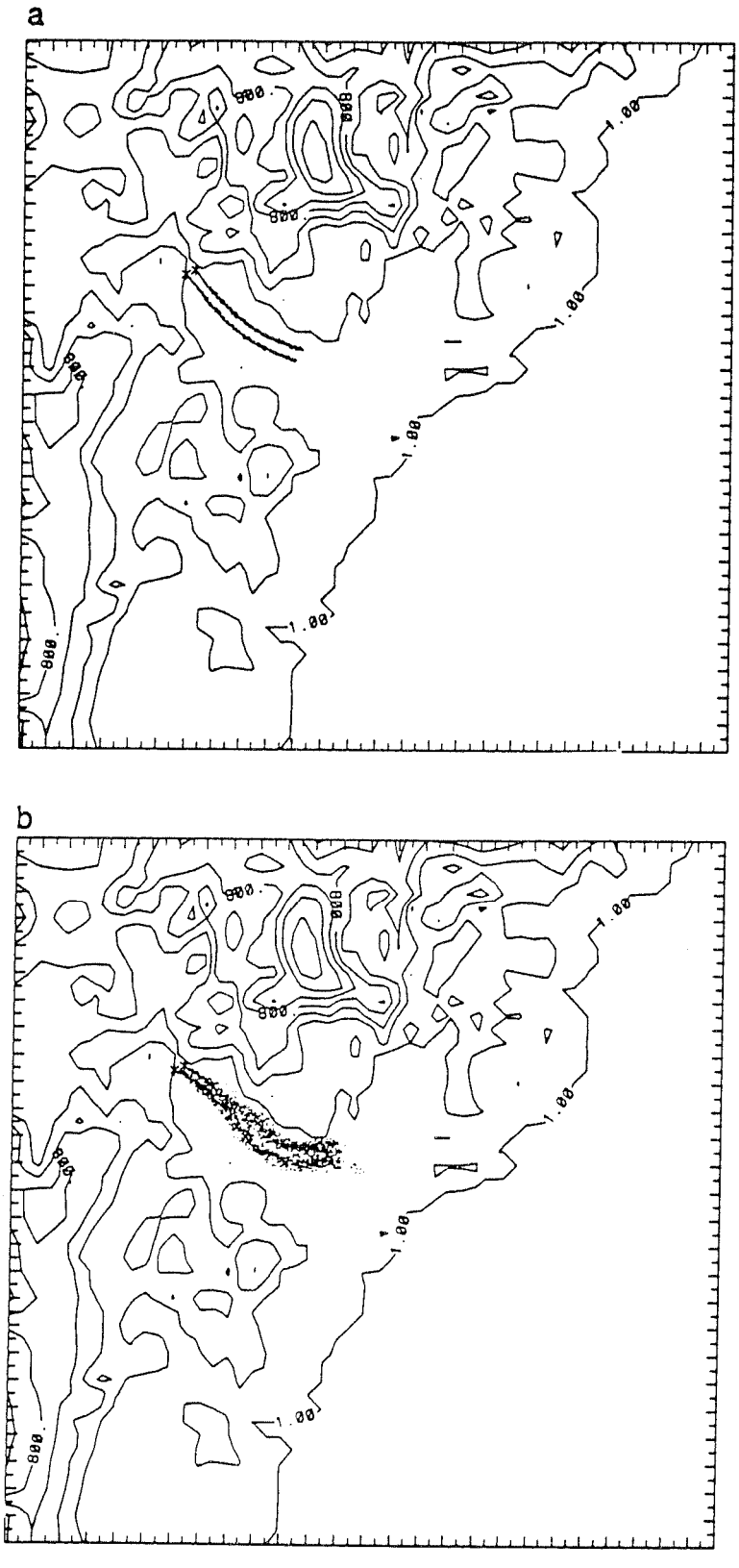

Figure 4.22: Plan view of particle distribution at (a) 0800 LST and (b) 1000 LST. Locations of Bayswater and Liddell are indicated by asterisks. Tick mark interval represents a distance of 5 km.

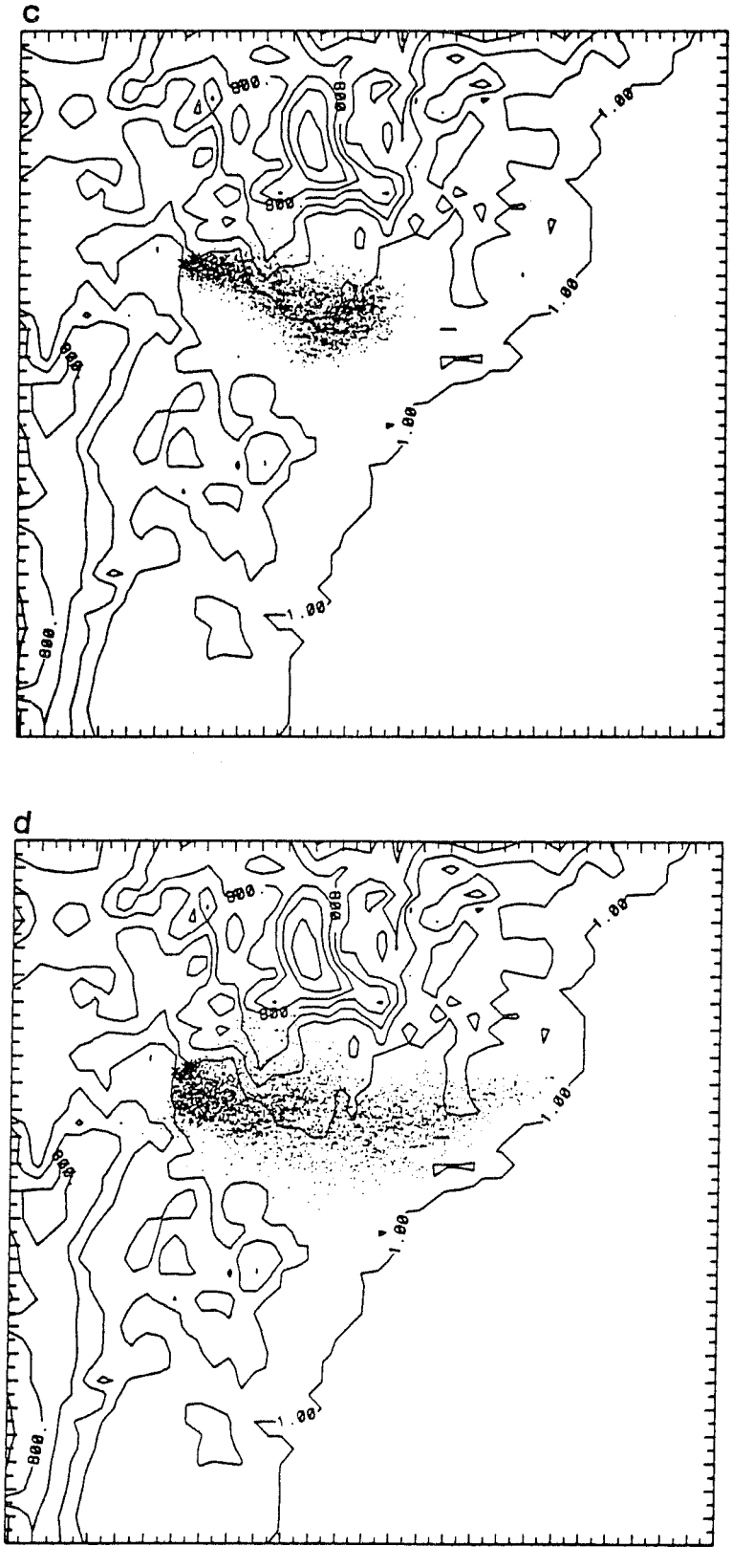

Figure 4.22: Plan view of particle distribution at (c) 1300 LST and (d) 1600 LST. Locations of Bayswater and Liddell are indicated by asterisks. Tick mark interval represents a distance of 5 km.

up the Valley. This is not obvious in the 1600 LST plan view of the particles (Fig.4.22d) in which particles in the sea-breeze return flow above about 1000 m mask the particle-free air below. However, the progression of clean air up the Valley can be seen in the surface concentration plots discussed in the next Section.

By 2000 LST, the plumes are moving westward in the sea breeze and are no longer being mixed to the ground (Fig.4.23a). Plume material is widely distributed over the region, although none of it is near the surface. The winds at plume level continue to back during the night such that by midnight they are blowing down the valley again, leaving a well-defined plume trail to the southwest (Fig.4.23b).

4.4.2 Ground-level concentrations

Half-hourly averaged ground-level concentrations (*glcs*) of SO_2 supplied by ECNSW in units of parts per hundred million (pphm) have been converted to $\mu g\ m^{-3}$ by multiplying by 30 and are shown in Table 4.3, to the nearest 30 $\mu g\ m^{-3}$. Hourly-averaged values are given, except during the morning fumigation period (0830 to 1100 EST) when half-hourly averages are tabled. The locations of the monitoring sites are shown in Fig.4.24a; the monitor at Mount Arthur was inoperable on this day.

Model predictions are also given in Table 4.3, but we discuss the observations first. The readings at Muswellbrook between 0500 and 0800 EST occur when the wind at the power stations is blowing away from Muswellbrook (Fig.4.11). This suggests the *glcs* over this period may be early-evening emissions returning from further up the Valley in the drainage wind (see discussion in Section 4.3.3). By 0800 EST, *glcs* are registering downwind from the power stations at Ravensworth, where readings continue until 1400 EST, and at Singleton where non-zero values last only to 0900 EST. The simultaneous readings at these two stations, and the large value at 0830 EST, suggest fumigation to the ground of one or both of the plumes from Liddell and Bayswater. Smaller, but significant, readings continue at Ravensworth throughout the morning convective conditions. As the wind backs to westerly around noon, the Lake Liddell monitor begins to register SO_2, continuing through until 1900 EST, after which time no *glcs* are recorded at any station.

Turning now to the model predictions, it should be noted that in Table 4.3 we are subjecting our modelling to the severest possible test, viz, a

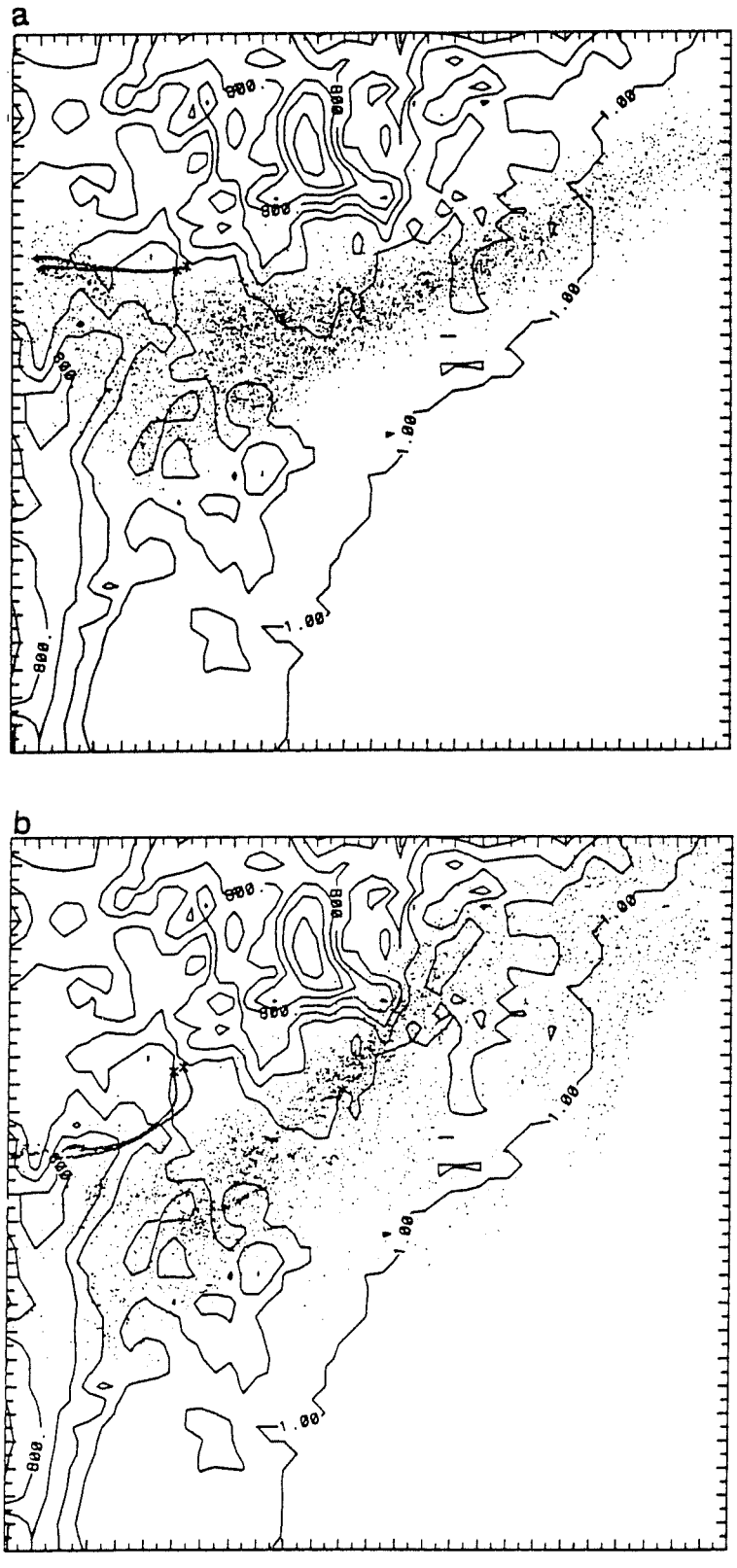

Figure 4.23: Plan view of particle distribution at (a) 2000 LST and (b) 2400 LST. Locations of Bayswater and Liddell power stations are indicated by asterisks. Tick mark interval represents a distance of 5 km.

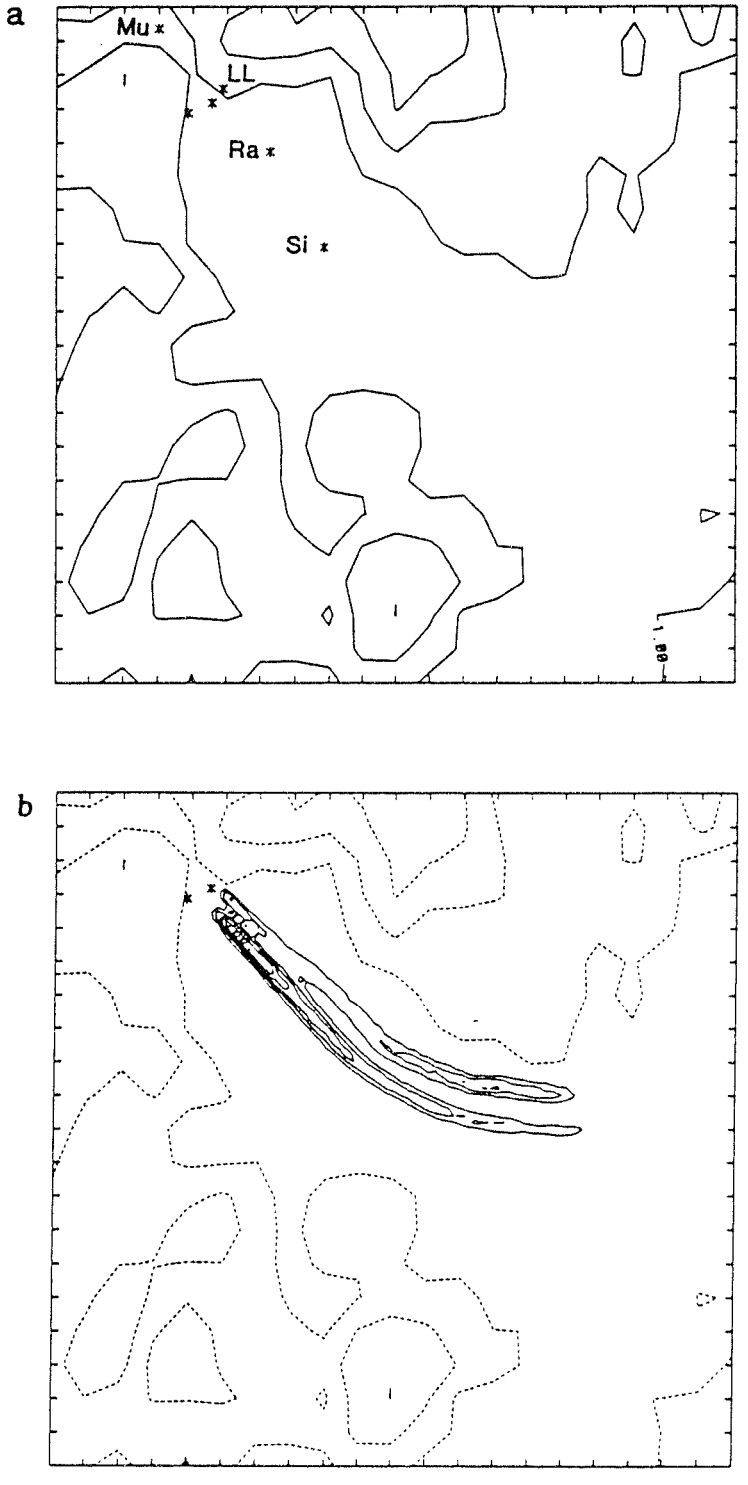

Figure 4.24: (a) Locations of SO_2 monitors, at Muswellbrook (Mu), Lake Liddell (LL), Ravensworth (Ra) and Singleton (Si), on 30 November 1989. Bayswater and Liddell power stations are also shown. (b) Predicted ground-level concentrations of SO_2 (solid lines) on 30 November 1989 for the half-hour period ending at 0930 LST. Contour interval is 50 $\mu g\ m^{-3}$. Dashed lines indicate orography contours at a spacing of 200 m. Tick mark interval is 5 km.

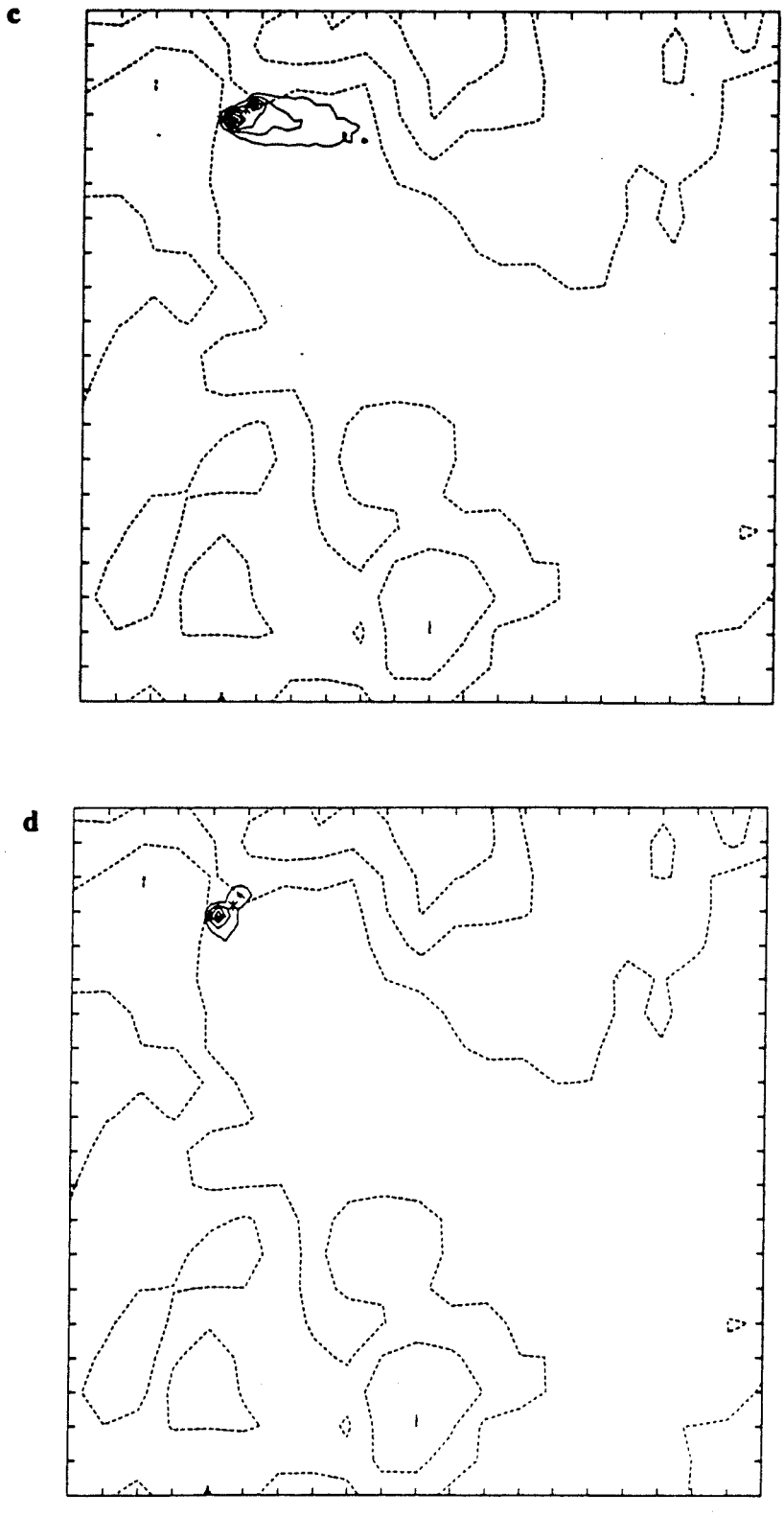

Figure 4.24: Predicted ground-level concentrations of SO_2 (solid lines) on 30 November 1989 for the hourly period ending at (c) 1300 and (d) 1700 LST. Contour interval is 50 $\mu g \ m^{-3}$. Dashed lines indicate orography contours at a spacing of 200 m. Tick mark interval is 5 km.

comparison of data with the predicted values at specified times at the point location of each monitor. With this in mind, it can be said that agreement at these isolated receptors is good. We note that the early-morning Muswellbrook readings could not be predicted as particles were only released from 0400 LST onwards. The large concentration of 330 $\mu g\ m^{-3}$ observed at Ravensworth at 0830 EST (when only the Liddell plume had fumigated in the model) was not predicted at that time, but an hour later when the Bayswater plume had also fumigated, a value of 300 $\mu g\ m^{-3}$ was predicted 3 km from the location of the Ravensworth monitor. Similarly, the discrepancies between the Singleton readings and predictions can be improved by a small lateral displacement of the predicted plume.

Time (EST)	Lake Liddell Obs	Mod	Muswellbrook Obs	Mod	Ravensworth Obs	Mod	Singleton Obs	Mod
0100	0	-	0	-	30	-	0	-
0200	0	-	0	-	0	-	0	-
0300	0	-	0	-	0	-	0	-
0400	0	-	0	-	0	-	0	-
0500	0	0	30	0	0	0	0	0
0600	0	0	75	0	0	0	0	0
0700	0	0	90	0	0	0	0	0
0800	0	0	15	0	105	0	15	0
0830	0	0	0	0	330	20	60	0
0900	0	0	0	0	120	100	60	0
0930	0	0	0	0	120	100	0	150
1000	0	0	0	0	150	100	0	40
1030	0	0	0	0	120	120	0	0
1100	0	0	0	0	120	30	0	0
1200	0	50	0	0	60	20	0	0
1300	30	50	0	0	45	30	0	0
1400	120	80	0	0	15	50	0	0
1500	120	80	0	0	0	70	0	0
1600	60	50	0	0	0	40	0	0
1700	105	70	0	0	0	0	0	0
1800	30	0	0	0	0	0	0	0
1900	30	0	0	0	0	0	0	0
2000	0	0	0	0	0	0	0	0
2100	0	0	0	0	0	0	0	0
2200	0	0	N/A	0	0	0	N/A	0
2300	0	0	N/A	0	N/A	0	N/A	0
2400	0	0	0	0	30	0	0	0

Table 4.3. Observed and predicted ground-level concentrations of SO2 in $\mu g\ m^{-3}$ at various locations for 30 November 1989. Values are hourly averages, except between 0830 and 1100 EST when half-hourly averages are shown. Observations are to the nearest 30 $\mu g\ m^{-3}$ and predictions to the nearest 20 $\mu g\ m^{-3}$.

By 0930 LST, the Bayswater plume has been brought to ground (Fig.4.24b) and the predicted concentrations at Ravensworth agree well with the observations. Note that some of the largest *glcs* (around 150 $\mu g\ m^{-3}$) associated with the Liddell plume during this fumigation period are found 50 km downwind near Branxton. Although 150 $\mu g\ m^{-3}$ is predicted at this time for Singleton, whereas a reading of zero is observed, it should be noted that the plume is so narrow that a zero reading is predicted a mere 2 km across the plume from the Singleton site. Zero *glcs* are observed and predicted at

Singleton after 1000 EST and good agreement continues at Ravensworth throughout the day.

During the afternoon, the model predicts non-zero concentrations at Lake Liddell as the wind becomes more westerly. The magnitudes agree well with the observations, especially considering the strong horizontal *glc* gradient in that area (Fig.4.24c). Due to the weaker winds in the afternoon, the maximum *glcs* from each emitter are located closer to the source than earlier in the day. The model predicts zero *glcs* at Lake Liddell from 1800 LST onwards, after the sea breeze has changed the winds to east-southeasterly. Small readings only were observed during this time.

As the sea breeze moves up the Hunter Valley, it replaces polluted air with clean air, as is evident in a comparison of the 1300 and 1700 LST *glc* distributions (Figs.4.24c,d). A clearer illustration of this process can be seen in the *glc* plots at 2-hourly intervals when a contour spacing of 20 $\mu g\ m^{-3}$ is used (Fig.4.25). After 1900 EST, non-zero readings are neither predicted nor observed at any station.

4.4.3 Assessment of Lagrangian plume dispersion modelling

In the early 1980s, the United States EPA evaluated a variety of Gaussian air quality models in both urban and complex terrain situations. In summarising the results of these evaluations, Hanna (1988) says: "...the model predictions are poorly correlated with hourly observations paired in time and space, the predicted absolute maximum is typically accurate within a factor of two, and the observed and predicted values are within a factor of two of each other only about 30-50 percent of the time." Although we consider only one case study in this report, we find that the equivalent statistics of our air quality model are superior to those quoted by Hanna.

Taking into consideration the four monitoring sites, there exist 14 occasions on which non-zero *glcs* are both predicted and observed. On 11 out of these 14 occasions, predicted values are within a factor of two of the observations when the error bars of each are taken into account. There are a further 11 occasions when an observation or a prediction, but not both, is zero. However, most of these can be attributed to either a small displacement (up to 3 km) of the predicted plume from a monitoring site or to the late fumigation prediction of the plumes. On 5 of these 11 occasions, values are

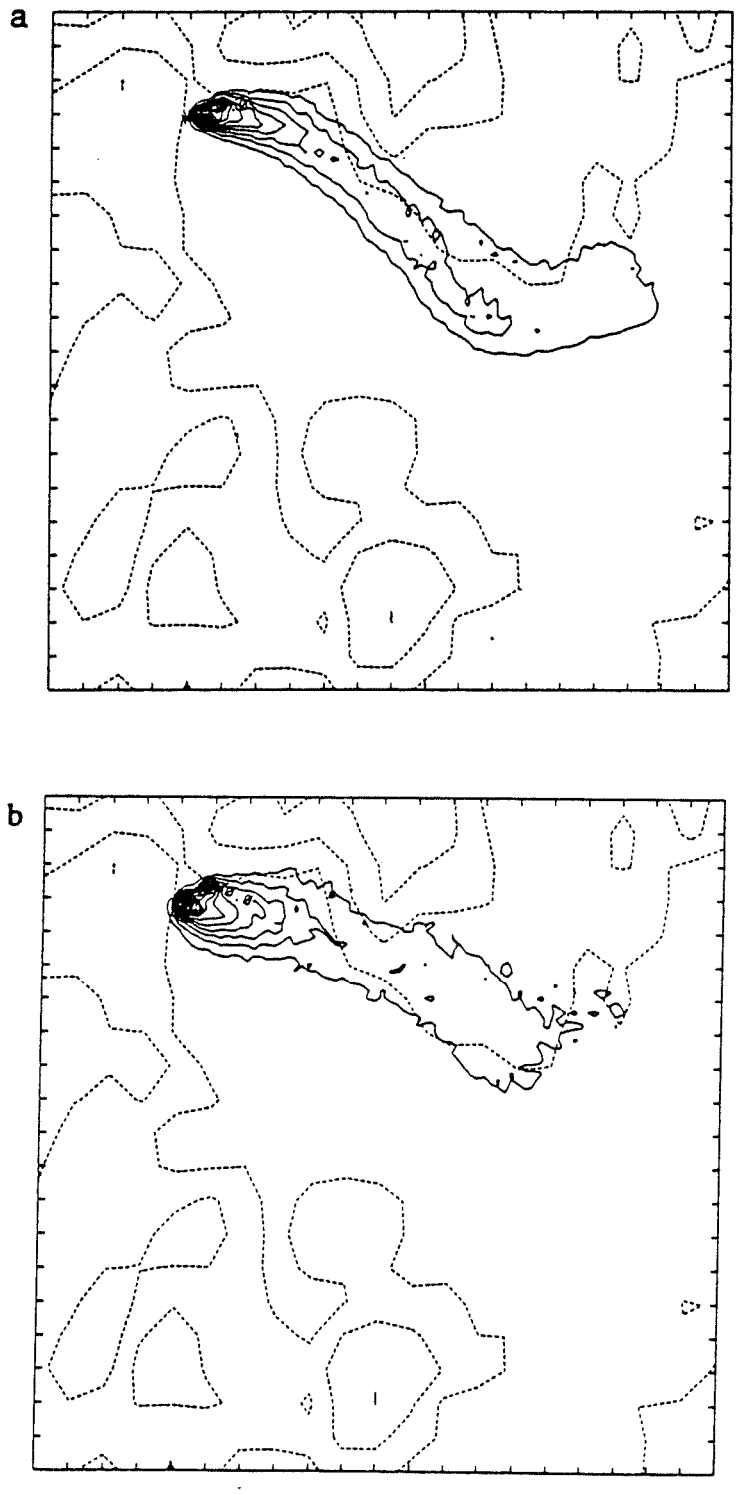

Figure 4.25: Predicted ground-level concentrations of SO_2 (solid lines) on 30 November 1989 for the hourly period ending at (a) 1200 and (b) 1400 LST. Contour interval is 20 $\mu g \ m^{-3}$. Dashed lines indicate orography contours at a spacing of 200 m. Tick mark interval is 5 km.

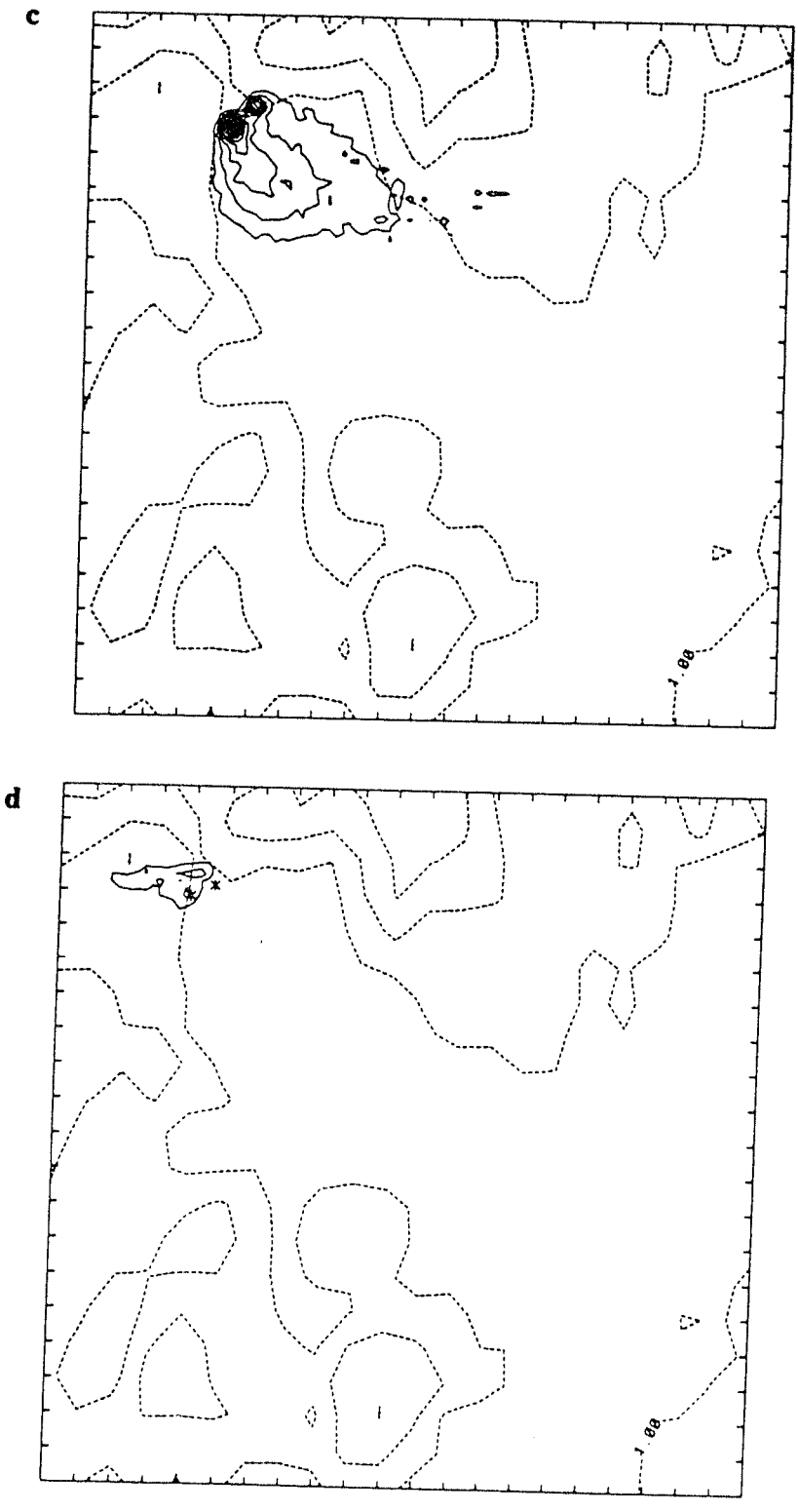

Figure 4.25: Predicted ground-level concentrations of SO_2 (solid lines) on 30 November 1989 for the hourly period ending at (c) 1600 and (d) 1800 LST. Contour interval is 20 $\mu g \ m^{-3}$. Dashed lines indicate orography contours at a spacing of 200 m. Tick mark interval is 5 km.

so small that error allowance brings them within a factor of 2 of each other. Therefore our model gives a total of 17 out of 25 pairings (i.e. 68 percent) in which the predicted values are within a factor of two of the observations.

A further evaluation of the model's performance can be obtained by using the model in a "real-time" (or regulatory?) mode to predict events in the vicinity of the monitors. At the "end of the day", we compare the predictions to information from the monitors. We have attempted to choose events which should be of interest to ECNSW and residents of the Hunter Valley. In making our predictions we have allowed for a lateral displacement of the modelled plume 3 km either side of each monitor. Below we list our predictions and corresponding observations for various events.

1. Early-morning fumigation will occur at considerable distances to the south-east of the emitters.

	Predicted	Observed
Time	0930 EST	0830 EST
Max. *glc* at Ravensworth	300 $\mu g\ m^{-3}$	330 $\mu g\ m^{-3}$
Max. *glc* at Singleton	180 $\mu g\ m^{-3}$	60 $\mu g\ m^{-3}$

2. After fumigation, *glcs* at all monitors will be lower for the rest of the day.

	Predicted	Observed
Max. *glc* for rest of day at Ravensworth	170 $\mu g\ m^{-3}$	150 $\mu g\ m^{-3}$
Max. *glc* for rest of day at Singleton	120 $\mu g\ m^{-3}$	0 $\mu g\ m^{-3}$

3. Zero readings will be recorded at Ravensworth and Singleton for part of the day.

	Predicted	Observed
Zero readings at Ravensworth after	1600 EST	1400 EST
Zero readings at Singleton after	1000 EST	0900 EST

4. Lake Liddell will record zero readings throughout the morning.

	Predicted	Observed
First non-zero reading for LL at	1200 EST	1300 EST
Maximum at LL during afternoon	150 $\mu g\ m^{-3}$	120 $\mu g\ m^{-3}$

5. Muswellbrook monitor will not record any *glcs* on this day. This was also observed.

Once again we note that the predicted *glcs* are derived from predicted winds and turbulence. Bearing this in mind and noting the success of the above five predictions (most of which arise from the non-steady nature of the winds), it is possible the modelling system can be used as a regulatory tool on occasions when high *glcs* can be expected. However, testing on further case studies is necessary, in order to expose the system to a wider range of conditions. At this stage of model development though, computing requirements (on the order of 6 hours on a supercomputer) would prevent any real-time runs.

Overall, the performance of the dispersion modelling system must be rated as very good, especially when it is borne in mind that the dispersion results discussed in this Section are dependent only on predicted winds and turbulence, apart from an initial specification of a representative large-scale wind and temperature profile for the region. Much of the success can be attributed to the excellent predictions of the windfield component, but the good agreement between the magnitudes of the observed and predicted *glcs* also gives us confidence in the techniques employed in the dispersion component. Such techniques include the mixing formulations, the plume-rise module, the assignment of a mass to each particle, and the space averaging of particle distributions to obtain *glcs*.

4.4.4 Sensitivity of results to input parameters

Results from the windfield model are predominantly sensitive to the initial values of four parameters: vertical temperature profile, soil wetness, wind speed and wind direction.

The initial temperature profile determines the rate at which the mixed layer grows and its ultimate depth by late afternoon. It also determines the final-rise height of plumes from the power stations. For our case-study day, the initial stability of the atmosphere below 2500m was not great and the mixed layer grew quickly. Stronger initial stability would result in a shallower mixed layer, which would then lead to higher ground-level concentrations, with an inverse linear relationship applying during convective conditions. Morning fumigation of the plume to the ground also occurs later with a stronger initial stability profile.

Soil wetness is also a parameter which determines the rise rate and ultimate depth of the mixed layer. A moister soil leads to shallower mixed layers because a greater proportion of available energy at the surface is partitioned into latent heat of evaporation rather than into sensible heat. Thus, all other parameters being the same, a moister soil should lead to higher *glcs*. Since the model predictions for mixed-layer depth and ground-level concentrations on the case-study day agree well with observations, we can assume that the chosen values for the initial temperature profile (as observed at Williamtown) and the soil wetness are quite reasonable.

While the model has used synoptic wind speed and direction values from

the Bureau of Meteorology analysis charts (3 m s^{-1} from the northwest at the surface, decreasing linearly to 0 m s^{-1} at 900 m and above), and has predicted winds in close agreement with observations, it is of interest to examine the model's response to alternative initial winds.

For a run carried out with a northwesterly synoptic wind of 2 m s^{-1} at all levels (no shear), the northwesterly winds still develop in the morning in the Upper Hunter region, but unlike for the case study run, they do not weaken at any stage during the day. Consequently, the sea breeze does not penetrate inland as quickly and decays before reaching the power stations at Lake Liddell. Although a particle run was not done, the predicted *glcs* from such a run would compare much less favourably with the observations than did the case study run.

A run was also done with zero synoptic wind at all levels. The predicted windfields compared very poorly with the case study data: weak southeasterly winds were predicted in the Upper Hunter Valley for the morning period, casting doubt on the Hyde et al. (1981) interpretation of the observed northwesterlies as drainage winds. Furthermore, these winds strengthened in the afternoon as a general upslope/sea breeze flow from a southeasterly direction established itself over the whole model domain.

This brief sensitivity study has illustrated the importance of accurate specification of the synoptic windfield at all heights above the ground. In particular, the negligible winds aloft in the initial profile of the case-study run have been shown to be an important factor in producing the weak afternoon winds in the boundary layer.

5. ONGOING MODEL DEVELOPMENT

5.1 Vegetative canopy

In the latest version of the model, a simple, but realistic, soil/canopy scheme based on the work of Deardorff (1977, 1978) and Noilhan and Planton (1989) is employed at the lower boundary, enabling surface fluxes to be written in a resistance formulation. In particular, evaporation is a function of leaf stomatal resistance which in turn depends on a number of other variables. Parameter values which need to be specified over the modelling domain include roughness length, minimum stomatal resistance, leaf area index

and the fraction of vegetation (compared to bare soil) in each grid square. Soil moisture values in a shallow near-surface and a deeper layer are also needed. Details of the canopy scheme can be found in Kowalczyk et al. (1991).

5.2 Parameterizing the spread of a rising plume

An improvement to the parameterization of buoyant plume dispersion as the plume ascends to its final-rise height has recently been incorporated into the particle model. Particles at release time are distributed in a Gaussian manner about the effective stack height (*esh*), in contrast to the previous method of placing them all at the *esh*. Comparison to aircraft measurements of plume width from power stations on the central New South Wales coast indicates a significant improvement in predictions using the new technique.

Rather than assuming a plume cross-section is circular with concentration distributed in a Gaussian manner laterally and vertically, we assume the ratio of width to height is 2:1 (as is generally observed) while still keeping the Gaussian assumption for each direction. The radius of the circular cross-section at any time during plume rise has been shown by Briggs (1975) to be

$$R = \beta(z_p - z_s) = \beta z_r$$

where β is an entrainment constant usually taken to be 0.6, z_p is the plume height above ground, z_s is the stack height and z_r is the plume-rise height above the stack top. Assuming that the mean radius of the elliptical plume is also = R and that $\sigma = R/\sqrt{2}$, it can be shown that $\sigma_y = R$ and $\sigma_z = R/2$, i.e.

$$\sigma_y = 0.6 z_r \quad \text{and} \quad \sigma_z = 0.3 z_r .$$

In the formulation of this plume spread in the model, each particle is simply positioned at the effective stack height (x_e, y_e, z_e) plus a random distance which is proportional to the plume dimension in each direction. The equations used are

$$x = x_e + 0.6 z_r r_u$$
$$y = y_e + 0.6 z_r r_v$$
$$z = z_e + 0.3 z_r r_w$$

where r_u, r_v, r_w are random numbers from a (0,1) Gaussian distribution.

Unlike the previous method of positioning all particles at the effective stack height, this method allows plume partial penetration through the mixed-layer top to occur in a simple manner.

References

Andre, J-C., DeMoor, G., Lacarrere, P., Therry, G. and R. du Vachat, 1978: Modeling the 24-hour evolution of the mean and turbulent structures of the planetary boundary layer. J. Atmos. Sci., 35, 1862-1883.

Anthes, R.A., 1978: The height of the planetary boundary layer and the production of circulation in a sea breeze model. J. Atmos. Sci., 35, 1231-1239.

Atwater, M.A. and P.S. Brown, Jr., 1974: Numerical calculation of the latitudinal variation of solar radiation for an atmosphere of varying opacity. J. Appl. Meteorol., 13, 289-297.

Blackadar, A.K., 1979: High resolution models of the planetary boundary layer. Adv. Environ. Sci. Eng., I, 50-85.

Blackadar, A.K., 1962: The vertical distribution of wind and turbulent exchange in a neutral atmosphere. J. Geophys. Res., 67, 3095-3102.

Briggs, G.A., 1975: Plume-rise predictions. In Lectures on air pollution and environmental impact. Workshop Proceedings, Boston, Mass. 29 Sep.-3 Oct. 1975. American Meteorol. Soc., 59-111.

Briggs, G.A., 1984: Plume rise and buoyancy effects. In Atmospheric science and power production, edited by D. Randerson. United States Department of Energy. DOE/TIC-27061. Ch.8, 327-366.

Charnock, H., 1955: Wind stress on a water surface. Quart. J. Roy. Meteorol. Soc., 81, 639-640.

Davies, H., 1976: A lateral boundary formulation for multi-level prediction models. Quart. J. Roy. Meteorol. Soc., 102, 405-418.

Deardorff, J.W., 1974: Three-dimensional numerical study of the height and mean structure of a heated planetary boundary layer. Bound. Layer Meteorol., 7, 81-106.

Deardorff, J.W., 1977: A parameterization of ground-surface moisture content for use in atmospheric prediction models. J. Appl. Meteorol., 16, 1182-1185.

Deardorff, J.W., 1978: Efficient prediction of ground surface temperature and moisture, with inclusion of a layer of vegetation. J. Geophys. Res., 83 (C4), 1889-1903.

Deardorff, J.W. and G.E. Willis, 1982: Ground level concentrations due to fumigation into an entraining mixed layer. Atmospheric Environment, 16, 1159-1170.

Durran, D.R. and J.B. Klemp, 1983: A compressible model for the simulation of moist mountain waves. Mon. Weather Rev., 111, 2341-2361.

Hanna, S.R., 1988: Air quality model evaluation and uncertainty. JAPCA, 38, 406-412.

Hurley, P.J. and W.L. Physick, 1991: A Lagrangian particle model of fumigation by breakdown of the nocturnal inversion. Atmos. Environ. 25A,1313-1325.

Hurley, P.J. and W.L. Physick, 1993: A skewed homogeneous Lagrangian particle model for convective conditions. Atmos. Environment 27A, 619-624.

Hyde, R., Malfroy, H., Watt, G.N. and J. Maynard, 1981: The Hunter Valley meteorological study. Interim Report to the New South Wales State Pollution Control Commission on mesoscale meteorology in the Hunter Valley. June 1981. School of Earth Sciences, Macquarie University, New South Wales.

Kikuchi, Y., Arakawa, S., Kimura, F., Shirasaki, K. and Y. Nagano, 1981: Numerical study on the effects of mountains on the land and sea breeze circulation in the Kanto district. J. Meteorol. Soc. Jpn., 59, 723-738.

Kowalczyk, E.A., Garratt, J.R. and P.B. Krummel, 1991: A soil-canopy scheme for use in a numerical model of the atmosphere - 1D stand-alone model. CSIRO Division of Atmospheric Research, Technical Paper No. 23.

Legg, B.J. and M.R. Raupach, 1982: Markov-chain simulation of particle dispersion in inhomogeneous flows: the mean drift velocity induced by a gradient in Eulerian velocity variance. Bound. Layer Meteorol., 24, 3-13.

Louis, J-F., 1979: A parametric model of vertical eddy fluxes in the atmosphere. Bound. Layer Meteorol., 17, 187-202.

Luhar, A.K. and R.E. Britter, 1989: A random walk model for dispersion in inhomogeneous turbulence in a convective boundary layer. Atmospheric Environment, 23, 1911-1924.

McGregor, J.L., 1993: Economical determination of departure points for semi-Lagrangian models. Mon. Weather Rev., 121, 221-230.

McNider, R.T., 1981: Investigation of the impact of topographic circulations on the transport and dispersion of air pollutants. PhD Dissertation. Department of Environmental Sciences, University of Virginia, Charlottesville.

McNider, R.T. and R.A. Pielke, 1981: Diurnal boundary-layer development over sloping terrain. J. Atmos. Sci., 38, 2198-2212.

McNider, R.T., Moran, M.D. and R.A. Pielke, 1988: Influence of diurnal and inertial boundary layer oscillations on long-range dispersion. Atmospheric Environment, 22, 2445-2462.

Mahfouf, J.F., Richard, E., Mascart, P.,Nickerson, E.C. and R. Rosset, 1987: A comparative study of various parameterizations of the planetary boundary layer in a numerical model. J. Clim. Appl. Meteorol., 26, 1671-1695.

Mahrer, Y. and R.A. Pielke, 1977: A numerical study of the airflow over irregular terrain. Beitr. Phys. Atmos., 50, 98-113.

Manins P.C., 1977: Fumigation and a laboratory experiment. Weather, 32, 221-228.

Manins, P.C., 1987: Plume rise in the Latrobe Valley. Victoria State Electricity Commission Research and Development Report No. LO/87/940.

Noilhan, J. and S. Planton, 1989: A simple parameterization of land surface processes for meteorological models. Mon. Weather. Rev., 117, 536-549.

Overcamp, T.J. and T. Ku, 1980: A wind tunnel study of plume rise from two stacks. Presented at AUS/APCA Second Joint Conference on Applications of Air Pollution Meteorology, New Orleans, La USA 24-27 Mar. 1980.

Panofsky, H.A., Lenschow, D.H. and J.C. Wyngaard, 1977: The characteristics of turbulent velocity components in the surface layer under convective conditions. Bound. Layer Meteorol., 11, 355-361.

Pasquill, F., 1974: Atmospheric Diffusion, John Wiley and Sons.

Physick, W.L., Abbs, D.J., and R.A. Pielke, 1989: Formulation of the thermal internal boundary layer in a mesoscale model. Bound. Layer Meteorol., 49, 99-111.

Physick, W.L., Noonan, J. A., and P.C. Manins, 1991: Air quality modelling study of the Hunter Valley. Phase I: Emitters in the Upper Hunter. CSIRO Division of Atmospheric Research. A Report to the Electricity Commission of New South Wales. 145pp May 1991.

Physick, W.L. and D.J. Abbs, 1991: Modelling of summertime flow and dispersion in the coastal terrain of south-eastern Australia. Mon. Weather. Rev., 119, 1014-1030.

Sawford, B.L., 1985: Lagrangian statistical simulation of concentration mean and fluctuation fields. J. Clim. Appl. Met. 24, 1152-1166.

Sawford, B.L. and F.M. Guest, 1987: Lagrangian stochastic analysis of flux-gradient relationships in the convective boundary layer. J. Atmos. Sci., 44, 1152-1165.

Temperton, C. and A. Staniforth, 1987: An efficient two-time-level semi-Lagrangian semi-explicit integration scheme. Quart. J. Roy. Meteorol. Soc., 113, 1025-1039.

Thomson, D.J., 1987: Criteria for the selection of stochastic models of particle trajectories in turbulent flows. J. Fluid Mech., 180, 529-556.

Turner D.B., 1970: Workbook of atmospheric dispersion estimates. U.S. Environment Protection Agency. Office of Air Programs Publications. No. AP-26, pp. 35-36.

Yamada, T. and G. Mellor, 1975: A simulation of the Wangara atmospheric boundary layer data. J. Atmos. Sci., 32, 2309-2329.

APPENDIX A

Transformation of equations from an (x,y,z) to an (x,y,σ) coordinate system

LADM solves five prognostic equations in an (x,y,σ) coordinate system where $\sigma = p/p_s$ and p_s is the surface pressure. The (x,y,σ) equations can be derived from the (x,y,z) equations using the appropriate coordinate transformations. The equations of motion in an (x,y,z) coordinate system are

$$\frac{D\underline{v}}{Dt} + 2\,\underline{\Omega} \times \underline{v} = -\frac{1}{\rho}\underline{\nabla}p - g\underline{k} + (\underline{\nabla}\cdot K_m \underline{\nabla})\underline{v} \; .$$

Expanding and making the hydrostatic assumption, we obtain

$$\frac{\partial u}{\partial t} + u\frac{\partial u}{\partial x} + v\frac{\partial u}{\partial y} + w\frac{\partial u}{\partial z} - fv = -\frac{1}{\rho}\frac{\partial p}{\partial x} + \frac{\partial}{\partial x}K_m^H\frac{\partial u}{\partial x} + \frac{\partial}{\partial y}K_m^H\frac{\partial u}{\partial y} + \frac{1}{\rho}\frac{\partial \tau_{zx}}{\partial z} \qquad (A.1)$$

$$\frac{\partial v}{\partial t} + u\frac{\partial v}{\partial x} + v\frac{\partial v}{\partial y} + w\frac{\partial v}{\partial z} + fu = -\frac{1}{\rho}\frac{\partial p}{\partial y} + \frac{\partial}{\partial x}K_m^H\frac{\partial v}{\partial x} + \frac{\partial}{\partial y}K_m^H\frac{\partial v}{\partial y} + \frac{1}{\rho}\frac{\partial \tau_{zy}}{\partial z} \qquad (A.2)$$

$$0 = -\frac{1}{\rho}\frac{\partial p}{\partial z} + g. \qquad (A.3)$$

The continuity equation is $\quad \frac{1}{\rho}\frac{D\rho}{Dt} + (\underline{\nabla} \cdot \underline{v}) = 0$

$$\frac{1}{\rho}\frac{\partial \rho}{\partial t} + \frac{u}{\rho}\frac{\partial \rho}{\partial x} + \frac{v}{\rho}\frac{\partial \rho}{\partial y} + \frac{w}{\rho}\frac{\partial \rho}{\partial z} + \rho\frac{\partial u}{\partial x} + \rho\frac{\partial v}{\partial y} + \rho\frac{\partial w}{\partial z} = 0 \qquad (A.4)$$

The thermodynamic equation is $\dfrac{D\Theta}{Dt} = (\underline{\nabla}\cdot K_H \underline{\nabla})\Theta + \left(\dfrac{\partial\Theta}{\partial t}\right)_{rad}$

$$\frac{\partial\Theta}{\partial t} + u\frac{\partial\Theta}{\partial x} + v\frac{\partial\Theta}{\partial y} + w\frac{\partial\Theta}{\partial z} = \frac{\partial}{\partial x}K_H^H\frac{\partial\Theta}{\partial x} + \frac{\partial}{\partial y}K_H^H\frac{\partial\Theta}{\partial y} + \frac{\partial}{\partial z}K_H^Z\frac{\partial\Theta}{\partial z} + \left(\frac{\partial\Theta}{\partial t}\right)_{rad} \tag{A.5}$$

where $(\partial\Theta/\partial t)_{rad}$ represents the source-sink term (radiative cooling, latent heat of condensation etc.)

and the equation for specific humidity is $\dfrac{Dq}{Dt} = (\underline{\nabla}\cdot K_q \underline{\nabla})q.$

$$\frac{\partial q}{\partial t} + u\frac{\partial q}{\partial x} + v\frac{\partial q}{\partial y} + w\frac{\partial q}{\partial z} = \frac{\partial}{\partial x}K_q^H\frac{\partial q}{\partial x} + \frac{\partial}{\partial y}K_q^H\frac{\partial q}{\partial y} + \frac{\partial}{\partial z}K_q^Z\frac{\partial q}{\partial z}. \tag{A.6}$$

The transformation from this z-coordinate system (x_1, y_1, z, t_1) to a σ-coordinate system (x_2, y_2, σ, t_2) where $x_1 = x_2$, $y_1 = y_2$ and $t_1 = t_2$ is detailed below. The derivative with respect to x $(\partial/\partial x)$ in a σ-coordinate system can be derived from the z-coordinate system as follows:

$$\frac{\partial}{\partial x_2} = \frac{\partial x_1}{\partial x_2}\frac{\partial}{\partial x_1} + \frac{\partial y_1}{\partial x_2}\frac{\partial}{\partial y_1} + \frac{\partial z}{\partial x_2}\frac{\partial}{\partial z} + \frac{\partial t_1}{\partial x_2}\frac{\partial}{\partial t_1}$$

which reduces to

$$\frac{\partial}{\partial x_2} = \frac{\partial}{\partial x_1} + \frac{\partial z}{\partial x_2}\frac{\partial}{\partial z}.$$

The above equation can also be written as

$$\frac{\partial}{\partial x_2} = \frac{\partial}{\partial x_1} + \frac{1}{g}\frac{\partial(gz)}{\partial x_2}\left(\frac{\partial\sigma}{\partial z}\frac{\partial}{\partial\sigma}\right). \tag{A.7}$$

Now $\sigma = \dfrac{p}{p_s}$, and taking the z-derivative gives

$$\frac{\partial \sigma}{\partial z} = \frac{1}{p_s}\frac{\partial p}{\partial z}$$

$$= \frac{1}{p_s}(-\rho g), \quad \text{using the hydrostatic equation}$$

$$= -\frac{g}{p_s}\frac{p}{RT}, \quad \text{using the perfect gas law,} \quad p = \rho RT.$$

Therefore
$$\frac{\partial \sigma}{\partial z} = -\frac{g\sigma}{RT}. \tag{A.8}$$

Substituting (A.8) into (A.7) and rearranging gives

$$\frac{\partial}{\partial x_1} = \frac{\partial}{\partial x_2} + \frac{1}{g}\frac{\partial (gz)}{\partial x_2}\left(\frac{g\sigma}{RT}\frac{\partial}{\partial \sigma}\right).$$

Dropping the subscripts for the (x,y,σ,t) coordinate system, the transformation becomes

$$\frac{\partial}{\partial x_1} = \frac{\partial}{\partial x} + \frac{\sigma}{RT}\frac{\partial \phi}{\partial x}\frac{\partial}{\partial \sigma}, \qquad \text{where} \quad \phi = gz. \tag{A.9}$$

In a similar manner the transformations with respect to y, σ and t reduce to

$$\frac{\partial}{\partial y_1} = \frac{\partial}{\partial y} + \frac{\sigma}{RT}\frac{\partial \phi}{\partial y}\frac{\partial}{\partial \sigma}, \tag{A.10}$$

$$\frac{\partial}{\partial t_1} = \frac{\partial}{\partial t} + \frac{\sigma}{RT}\frac{\partial \phi}{\partial t}\frac{\partial}{\partial \sigma}, \tag{A.11}$$

$$\frac{\partial}{\partial z} = -\frac{g\sigma}{RT}\frac{\partial}{\partial \sigma}. \tag{A.12}$$

Using these coordinate transformations (eqns. A.9, A.10, A.11 and A.12) the Cartesian total derivative becomes in σ-coordinates

$$\frac{D}{Dt} = \frac{\partial}{\partial t} + u\frac{\partial}{\partial x} + v\frac{\partial}{\partial y} + \dot{\sigma}\frac{\partial}{\partial \sigma}$$

$$\text{where} \quad \dot{\sigma} = \frac{\sigma}{RT}\left\{\frac{\partial \phi}{\partial t} + u\frac{\partial \phi}{\partial x} + v\frac{\partial \phi}{\partial y} - wg\right\}. \tag{A.13}$$

Equations (A.1) to (A.6) can also be transformed using eqns. (A.9) to (A.12). For example the u-momentum equation can be written as

$$\frac{\partial u}{\partial t} + u\frac{\partial u}{\partial x} + v\frac{\partial u}{\partial y} + \dot{\sigma}\frac{\partial u}{\partial \sigma} - fv = -\frac{1}{\rho}\left\{\frac{\partial p}{\partial x} + \frac{\sigma}{RT}\frac{\partial \phi}{\partial x}\frac{\partial p}{\partial \sigma}\right\}$$

$$+\left\{\frac{\partial}{\partial x} + \frac{\sigma}{RT}\frac{\partial \phi}{\partial x}\frac{\partial}{\partial \sigma}\right\}\left[K_m^H\left\{\frac{\partial u}{\partial x} + \frac{\sigma}{RT}\frac{\partial \phi}{\partial x}\frac{\partial u}{\partial \sigma}\right\}\right]$$

$$+\left\{\frac{\partial}{\partial y} + \frac{\sigma}{RT}\frac{\partial \phi}{\partial y}\frac{\partial}{\partial \sigma}\right\}\left[K_m^H\left\{\frac{\partial u}{\partial y} + \frac{\sigma}{RT}\frac{\partial \phi}{\partial y}\frac{\partial u}{\partial \sigma}\right\}\right]$$

$$+\frac{RT}{p}\left\{-\frac{g\sigma}{RT}\frac{\partial \tau_{\sigma x}}{\partial \sigma}\right\},$$

and since $\dfrac{\partial p}{\partial x} = \sigma\dfrac{\partial p_s}{\partial x}$ and $\dfrac{\partial p}{\partial \sigma} = p_s$,

the term $$\frac{1}{\rho}\left\{\frac{\partial p}{\partial x} + \frac{\sigma}{RT}\frac{\partial \phi}{\partial x}\frac{\partial p}{\partial \sigma}\right\} = \frac{1}{\rho}\left\{\sigma\frac{\partial p_s}{\partial x} + \frac{\sigma}{RT}\frac{\partial \phi}{\partial x}p_s\right\}$$

$$= \frac{RT}{p}\left\{\frac{p}{p_s}\frac{\partial p_s}{\partial x} + \frac{p}{p_s}\frac{1}{RT}\frac{\partial \phi}{\partial x}p_s\right\}$$

$$= \frac{RT}{p_s}\frac{\partial p_s}{\partial x} + \frac{\partial \phi}{\partial x}$$

$$= RT \frac{\partial(\ln p_s)}{\partial x} + \frac{\partial \phi}{\partial x} .$$

Substituting back into the u-equation of motion and neglecting the usually smaller terms involving K_m^H gives

$$\frac{\partial u}{\partial t} + u \frac{\partial u}{\partial x} + v \frac{\partial u}{\partial y} + \dot{\sigma} \frac{\partial u}{\partial \sigma} - fv = - RT \frac{\partial(\ln p_s)}{\partial x} - \frac{\partial \phi}{\partial x}$$

$$+ \frac{\partial}{\partial x} \left[K_m^H \frac{\partial u}{\partial x} \right] + \frac{\partial}{\partial y} \left[K_m^H \frac{\partial u}{\partial y} \right] - \frac{g}{p_s} \frac{\partial \tau_{\sigma x}}{\partial \sigma} .$$

(A.14)

Similarly the v-equation of motion in a sigma coordinate system is

$$\frac{\partial v}{\partial t} + u \frac{\partial v}{\partial x} + v \frac{\partial v}{\partial y} + \dot{\sigma} \frac{\partial v}{\partial \sigma} + fu = - RT \frac{\partial(\ln p_s)}{\partial y} - \frac{\partial \phi}{\partial y}$$

$$+ \frac{\partial}{\partial x} \left[K_m^H \frac{\partial v}{\partial x} \right] + \frac{\partial}{\partial y} \left[K_m^H \frac{\partial v}{\partial y} \right] - \frac{g}{p_s} \frac{\partial \tau_{\sigma y}}{\partial \sigma} .$$

(A.15)

The hydrostatic equation (eq. A.3) can be written as

$$\frac{\partial p}{\partial z} = \frac{\partial p}{\partial \sigma} \frac{\partial \sigma}{\partial z} = -\rho g$$

which reduces to $$p_s \frac{\partial \sigma}{\partial z} = - \frac{p}{RT} g$$

and further to $$p_s \frac{\partial \sigma}{\partial \phi} = - \frac{\sigma p_s}{RT} .$$

Finally, in σ-coordinates the hydrostatic equation becomes

$$\frac{\partial \phi}{\partial \sigma} = -\frac{RT}{\sigma} . \tag{A.16}$$

The continuity equation (eq. A.4) can be written as

$$\frac{1}{\rho}\frac{D\rho}{Dt} + \underset{\sim}{\nabla}_H \cdot \underset{\sim}{v}_H + \frac{\partial w}{\partial z} = 0 \tag{A.17}$$

where $\underset{\sim}{\nabla}_H$ is the horizontal gradient operator $\left(\frac{\partial}{\partial x} , \frac{\partial}{\partial y} \right)$ and $\underset{\sim}{v}_H$ is the horizontal velocity (u,v) vector.

Rearranging the first term of equation (A.17) gives

$$\frac{1}{\rho}\frac{D\rho}{Dt} = \frac{RT}{p}\frac{D\,(p/RT)}{Dt}$$

$$= \frac{RT}{\sigma p_s}\frac{D\,(\sigma p_s \,/\, RT)}{Dt}$$

$$= \frac{T}{\sigma p_s}\left\{ \frac{\sigma}{T}\frac{Dp_s}{Dt} + \frac{p_s}{T}\frac{D\sigma}{Dt} + \sigma p_s \frac{D(1/T)}{Dt} \right\}$$

$$= \frac{1}{p_s}\frac{Dp_s}{Dt} + \frac{1}{\sigma}\frac{D\sigma}{Dt} + T\left\{ -\frac{1}{T^2}\frac{DT}{Dt} \right\}$$

$$= \frac{D(\ln p_s)}{Dt} + \frac{1}{\sigma}\frac{D\sigma}{Dt} - \frac{D(\ln T)}{Dt} \tag{A.18}$$

where D/Dt is now the total derivative in sigma coordinates. The final term of equation (A.17) $\partial w/\partial z$ can be transformed to the σ-coordinate system as follows. Rearranging eq. (A.13) gives

$$w = -\frac{RT}{\sigma g}\dot{\sigma} + \frac{1}{g}\left\{\frac{\partial \phi}{\partial t} + u\frac{\partial \phi}{\partial x} + v\frac{\partial \phi}{\partial y}\right\}$$

and using the sigma-coordinate transformations,

$$\frac{\partial w}{\partial z} = -\frac{g\sigma}{RT}\frac{\partial w}{\partial \sigma}$$

$$= -\frac{g\sigma}{RT}\left\{-\frac{R}{g}\frac{\partial(T\dot{\sigma}/\sigma)}{\partial \sigma} + \frac{1}{g}\left\{\frac{\partial^2 \phi}{\partial \sigma \partial t} + \frac{\partial u}{\partial \sigma}\frac{\partial \phi}{\partial x} + u\frac{\partial^2 \phi}{\partial \sigma \partial x} + \frac{\partial v}{\partial \sigma}\frac{\partial \phi}{\partial y} + v\frac{\partial^2 \phi}{\partial \sigma \partial y}\right\}\right\}$$

$$= -\frac{\sigma}{RT}\left\{-\frac{R\dot{\sigma}}{\sigma}\frac{\partial T}{\partial \sigma} - \frac{RT}{\sigma}\frac{\partial \dot{\sigma}}{\partial \sigma} + \frac{RT\dot{\sigma}}{\sigma^2}\right.$$

$$\left. + \left\{\frac{\partial^2 \phi}{\partial \sigma \partial t} + \frac{\partial u}{\partial \sigma}\frac{\partial \phi}{\partial x} + u\frac{\partial^2 \phi}{\partial \sigma \partial x} + \frac{\partial v}{\partial \sigma}\frac{\partial \phi}{\partial y} + v\frac{\partial^2 \phi}{\partial \sigma \partial y}\right\}\right\}. \qquad \text{(A.19)}$$

Substituting equations (A.18) and (A.19) back into the continuity equation (A.17) and transforming the remaining term gives in the σ-coordinate system

$$\frac{D(\ln p_s)}{Dt} + \frac{1}{\sigma}\frac{D\sigma}{Dt} - \frac{D(\ln T)}{Dt} + \left\{\underset{\sim H}{\nabla} \cdot \underset{\sim H}{v} + \frac{\sigma}{RT}\frac{\partial \phi}{\partial x}\frac{\partial u}{\partial \sigma} + \frac{\sigma}{RT}\frac{\partial \phi}{\partial y}\frac{\partial v}{\partial \sigma}\right\}$$

$$-\frac{\sigma}{RT}\left\{-\frac{R\dot{\sigma}}{\sigma}\frac{\partial T}{\partial \sigma} - \frac{RT}{\sigma}\frac{\partial \dot{\sigma}}{\partial \sigma} + \frac{RT\dot{\sigma}}{\sigma^2} + \left\{\frac{\partial^2 \phi}{\partial \sigma \partial t} + \frac{\partial u}{\partial \sigma}\frac{\partial \phi}{\partial x} + u\frac{\partial^2 \phi}{\partial \sigma \partial x}\right.\right.$$

$$\left.\left. + \frac{\partial v}{\partial \sigma}\frac{\partial \phi}{\partial y} + v\frac{\partial^2 \phi}{\partial \sigma \partial y}\right\}\right\} = 0.$$

Expanding and rearranging the above equation gives

$$\frac{D(\ln p_s)}{Dt} + \frac{\dot{\sigma}}{\sigma} - \frac{\partial(\ln T)}{\partial t} - u\frac{\partial(\ln T)}{\partial x} - v\frac{\partial(\ln T)}{\partial y} - \dot{\sigma}\frac{\partial(\ln T)}{\partial \sigma}$$

$$+ \left\{ \nabla_H \cdot \underset{-H}{v} + \frac{\sigma}{RT}\frac{\partial\phi}{\partial x}\frac{\partial u}{\partial \sigma} + \frac{\sigma}{RT}\frac{\partial\phi}{\partial y}\frac{\partial v}{\partial \sigma} \right\} + \frac{\dot{\sigma}}{T}\frac{\partial T}{\partial \sigma} + \frac{\partial\dot{\sigma}}{\partial\sigma} - \frac{\dot{\sigma}}{\sigma}$$

$$- \frac{\sigma}{RT}\left\{ \frac{\partial^2\phi}{\partial\sigma\partial t} + \frac{\partial u}{\partial\sigma}\frac{\partial\phi}{\partial x} + u\frac{\partial^2\phi}{\partial\sigma\partial x} + \frac{\partial v}{\partial\sigma}\frac{\partial\phi}{\partial y} + v\frac{\partial^2\phi}{\partial\sigma\partial y} \right\} = 0 ,$$

which reduces to

$$\frac{D(\ln p_s)}{Dt} - \frac{\partial(\ln T)}{\partial t} - u\frac{\partial(\ln T)}{\partial x} - v\frac{\partial(\ln T)}{\partial y}$$

$$+ \nabla_H \cdot \underset{-H}{v} + \frac{\partial\dot{\sigma}}{\partial\sigma} - \frac{\sigma}{RT}\left\{ \frac{\partial}{\partial t}\frac{\partial\phi}{\partial\sigma} + u\frac{\partial}{\partial x}\frac{\partial\phi}{\partial\sigma} + v\frac{\partial}{\partial y}\frac{\partial\phi}{\partial\sigma} \right\} = 0.$$

Using the hydrostatic equation this becomes

$$\frac{D(\ln p_s)}{Dt} - \frac{\partial(\ln T)}{\partial t} - u\frac{\partial(\ln T)}{\partial x} - v\frac{\partial(\ln T)}{\partial y}$$

$$+ \nabla_H \cdot \underset{-H}{v} + \frac{\partial\dot{\sigma}}{\partial\sigma} + \frac{\sigma}{RT}\left\{ \frac{\partial}{\partial t} + u\frac{\partial}{\partial x} + v\frac{\partial}{\partial y} \right\}\frac{RT}{\sigma} = 0.$$

Finally, the continuity equation becomes

$$\frac{D(\ln p_s)}{Dt} + \nabla_H \cdot \underset{-H}{v} + \frac{\partial\dot{\sigma}}{\partial\sigma} = 0. \qquad \text{(A.20)}$$

The thermodynamic equation (eq. (A.5)) can be written in terms of temperature T, using the following expression for potential temperature

$$\Theta = T \left(\frac{p_0}{p} \right)^{R/C_P} = T \left(\frac{p_0}{\sigma p_s} \right)^{R/C_P}$$

Substituting this into the first term of equation (A.5) gives

$$\frac{D\Theta}{Dt} = \left(\frac{p_0}{\sigma p_s} \right)^{R/C_P} \frac{DT}{Dt} + \frac{TR}{C_P} \left(\frac{p_0}{\sigma p_s} \right)^{(R/C_P - 1)} \frac{p_0}{\sigma} \left(- \frac{1}{p_s^2} \right) \frac{Dp_s}{Dt}$$

$$+ \frac{TR}{C_P} \left(\frac{p_0}{\sigma p_s} \right)^{(R/C_P - 1)} \frac{p_0}{p_s} \left(- \frac{1}{\sigma^2} \right) \frac{D\sigma}{Dt}$$

and in a σ-coordinate system the thermodynamic equation becomes

$$\left(\frac{p_0}{\sigma p_s} \right)^{R/C_P} \frac{DT}{Dt} - \frac{TR}{C_P} \left(\frac{p_0}{\sigma p_s} \right)^{(R/C_P - 1)} \frac{p_0}{\sigma} \left(\frac{1}{p_s^2} \right) \frac{Dp_s}{Dt}$$

$$- \frac{TR}{C_P} \left(\frac{p_0}{\sigma p_s} \right)^{(R/C_P - 1)} \frac{p_0}{p_s} \left(\frac{1}{\sigma^2} \right) \dot{\sigma}$$

$$= (\underline{\nabla} \cdot K_H \underline{\nabla}) T \left(\frac{p_0}{\sigma p_s} \right)^{R/C_P} + \left(\frac{\partial T}{\partial t} \right)_{rad} \left(\frac{p_0}{\sigma p_s} \right)^{R/C_P}$$

which reduces to

$$\frac{DT}{Dt} - \frac{TR}{C_P} \left(\frac{\sigma p_s}{p_0} \right) \frac{p_0}{\sigma} \left(\frac{1}{p_s^2} \right) \frac{Dp_s}{Dt} - \frac{TR}{C_P} \left(\frac{\sigma p_s}{p_0} \right) \frac{p_0}{p_s} \left(\frac{1}{\sigma^2} \right) \dot{\sigma}$$

$$= (\underline{\nabla} \cdot K_H \underline{\nabla}) T + \left(\frac{\partial T}{\partial t} \right)_{rad}$$

and further to

$$\frac{DT}{Dt} - \frac{TR}{C_p}\left(\frac{1}{p_s}\right)\frac{Dp_s}{Dt} - \frac{TR}{C_p}\left(\frac{\dot{\sigma}}{\sigma}\right) = (\underline{\nabla} \cdot K_H \underline{\nabla})\, T + \left(\frac{\partial T}{\partial t}\right)_{rad} .$$

Finally the thermodynamic equation in σ-coordinates becomes

$$\frac{DT}{Dt} = \frac{TR}{C_p}\left\{\frac{D(\ln p_s)}{Dt} + \frac{\dot{\sigma}}{\sigma}\right\} + (\underline{\nabla} \cdot K_H \underline{\nabla})\, T + \left(\frac{\partial T}{\partial t}\right)_{rad} \qquad (A.21)$$

The last model equation, the specific humidity equation (eq. (A.6)), becomes in σ-coordinates

$$\frac{Dq}{Dt} = (\underline{\nabla} \cdot K_q \underline{\nabla})\, q . \qquad (A.22)$$

To allow for simpler initialization of the model when simulating a situation with vertical wind shear, we partition p_s, T and ϕ into a basic state plus synoptic and mesoscale perturbations. Let α represent p_s, T or ϕ. We can write

$$\alpha = \alpha_0 + \hat{\alpha}' + \tilde{\alpha}'$$

where $\alpha_0(\sigma)$ is the constant base value, $\hat{\alpha}'(x,y,\sigma)$ is the synoptic perturbation and $\tilde{\alpha}'(x,y,\sigma)$ is the mesoscale perturbation. We now define the synoptic part of α as $\hat{\alpha} = \alpha_0 + \hat{\alpha}'$ and the mesoscale part as $\tilde{\alpha} = \alpha_0 + \tilde{\alpha}'$. Using this expression, the relevant terms in the equations can be written as follows: equation (A.14) becomes

$$\frac{Du}{Dt} - fv = -\frac{R(T_0 + \hat{T}' + \tilde{T}')}{(p_{s0} + \hat{p}_s' + \tilde{p}_s')}\,\frac{\partial(p_{s0} + \hat{p}_s' + \tilde{p}_s')}{\partial x} - \frac{\partial(\phi_0 + \hat{\phi}' + \tilde{\phi}')}{\partial x} + \cdots$$

$$= -\frac{R(T_0 + \hat{T}')}{(p_{s0} + \hat{p}'_s + \tilde{p}'_s)} \frac{\partial \hat{p}'_s}{\partial x} - \frac{R\tilde{T}'}{(p_{s0} + \hat{p}'_s + \tilde{p}'_s)} \frac{\partial \hat{p}'_s}{\partial x}$$

$$-\frac{R(T_0 + \tilde{T}')}{(p_{s0} + \hat{p}'_s + \tilde{p}'_s)} \frac{\partial \tilde{p}'_s}{\partial x} - \frac{R\hat{T}'}{(p_{s0} + \hat{p}'_s + \tilde{p}'_s)} \frac{\partial \tilde{p}'_s}{\partial x} - \frac{\partial \hat{\phi}'}{\partial x} - \frac{\partial \tilde{\phi}'}{\partial x} + \cdots$$

Neglecting terms that are the product of two perturbations and noting that the horizontal derivatives of the base state are zero, we obtain

$$\frac{Du}{Dt} - fv = -\frac{R\hat{T}}{(\hat{p}_s + \tilde{p}'_s)} \frac{\partial \hat{p}_s}{\partial x} - \frac{R\tilde{T}}{(\tilde{p}_s + \hat{p}'_s)} \frac{\partial \tilde{p}_s}{\partial x} - \frac{\partial \hat{\phi}}{\partial x} - \frac{\partial \tilde{\phi}}{\partial x} + \cdots .$$

Now

$$\hat{p}_s + \tilde{p}'_s = \hat{p}_s \left(1 + \frac{\tilde{p}'_s}{\hat{p}_s}\right) \approx \hat{p}_s, \quad \text{and } \tilde{p}_s \gg \hat{p}'.$$

Therefore

$$\frac{Du}{Dt} - fv = -\frac{R\hat{T}}{\hat{p}_s} \frac{\partial \hat{p}_s}{\partial x} - \frac{R\tilde{T}}{\tilde{p}_s} \frac{\partial \tilde{p}_s}{\partial x} - \frac{\partial \hat{\phi}}{\partial x} - \frac{\partial \tilde{\phi}}{\partial x} + \cdots . \tag{A.23}$$

We choose the synoptic state to be in geostrophic balance, so

$$-fv_g = -\frac{R\hat{T}}{\hat{p}_s} \frac{\partial \hat{p}_s}{\partial x} - \frac{\partial \hat{\phi}}{\partial x}$$

$$fu_g = -\frac{R\hat{T}}{\hat{p}_s} \frac{\partial \hat{p}_s}{\partial y} - \frac{\partial \hat{\phi}}{\partial y} .$$

Substituting these expressions into Eq. (A.23) gives

$$\frac{Du}{Dt} - f(v - v_g) = -\frac{R\tilde{T}}{\tilde{p}_s} \frac{\partial \tilde{p}_s}{\partial x} - \frac{\partial \tilde{\phi}}{\partial x} + (\underline{\nabla}_H \cdot K_m^H \underline{\nabla}_H) u - \frac{g}{\tilde{p}_s} \frac{\partial \tau_{\sigma x}}{\partial \sigma} .$$

Similarly Eq. A.(15) becomes

$$\frac{Dv}{Dt} + f(u - u_g) = - \frac{R\tilde{T}}{\tilde{p}_s} \frac{\partial \tilde{p}_s}{\partial y} - \frac{\partial \tilde{\phi}}{\partial y} + (\underset{\sim}{\nabla}_H \cdot K_m^H \underset{\sim}{\nabla}_H) v - \frac{g}{\tilde{p}_s} \frac{\partial \tau_{\sigma y}}{\partial \sigma} .$$

The remaining equations stay the same, with $\tilde{\phi}$, $\tilde{p}_s$ and $\tilde{T}$ replacing ϕ, p_s and T. Dropping the ~, the equations used in LADM are

$$\frac{Du}{Dt} - f(v - v_g) = - \frac{RT}{p_s} \frac{\partial p_s}{\partial x} - \frac{\partial \phi}{\partial x} + (\underset{\sim}{\nabla}_H \cdot K_m^H \underset{\sim}{\nabla}_H) u - \frac{g}{p_s} \frac{\partial \tau_{\sigma x}}{\partial \sigma} ,$$

$$\frac{Dv}{Dt} + f(u - u_g) = - \frac{RT}{p_s} \frac{\partial p_s}{\partial y} - \frac{\partial \phi}{\partial y} + (\underset{\sim}{\nabla}_H \cdot K_m^H \underset{\sim}{\nabla}_H) v - \frac{g}{p_s} \frac{\partial \tau_{\sigma y}}{\partial \sigma} ,$$

$$\frac{\partial \phi}{\partial \sigma} = - \frac{RT}{\sigma} ,$$

$$\frac{D(\ln p_s)}{Dt} + \underset{\sim}{\nabla}_H \cdot \underset{\sim}{v}_H + \frac{\partial \dot{\sigma}}{\partial \sigma} = 0 ,$$

$$\frac{DT}{Dt} = \frac{TR}{C_p} \left\{ \frac{D(\ln p_s)}{Dt} + \frac{\dot{\sigma}}{\sigma} \right\} + (\underset{\sim}{\nabla} \cdot K_T^H \underset{\sim}{\nabla}) T + \frac{g}{C_p p_s} \frac{\partial H}{\partial \sigma} + \left(\frac{\partial T}{\partial t} \right)_{rad} ,$$

$$\frac{Dq}{Dt} = (\underset{\sim}{\nabla}_H \cdot K_q^H \underset{\sim}{\nabla}_H) q + \frac{g}{L p_s} \frac{\partial E}{\partial \sigma} .$$

APPENDIX B

Experiments on the sampling box size and number of particles

The dispersion component of LADM is run in two modes; *near-source* mode to determine the maximum ground-level concentration (*glc*), which usually occurs within 5 km of a stack in convective conditions, and *far-field* mode to examine dispersion many kilometres from the stack. In this Appendix, we examine (1) the rate at which particles must be released in order to obtain realistic *glcs* both near and far from the source, and (2) the size of the sampling box needed to obtain accurate values of the maximum *glc* near the source. The model version used for all experiments in this Appendix employs a Gaussian rather than a skewed pdf for the vertical turbulent component.

B.1 Particle release rates (N) for far-field concentrations

In this section we discuss the threshold accuracy *e* of the predicted *glcs* and present a Table showing, as a function of emission rate, the value of N needed to obtain a specified accuracy *e*. The significance of *e* is illustrated by *glc* plots from a model run with Liddell power station as the emitter for the case-study day 30 November 1989 (see Section 4.3). The winds cover a wide range of speed and direction on this day, allowing *glcs* to be calculated under a variety of meteorological conditions. Particles are released each timestep (20 seconds) from 0700 LST onwards, with hourly-averaged *glcs* calculated from 0900 till 1700 LST. The emission rate Q is 1000 g s^{-1}. The sampling box in these experiments has horizontal dimensions of $\Delta x = \Delta y = 1000$ m and a height Δz of 25 m. This is quite sufficient to resolve the plume at distances greater than 4 to 5 km from the source.

If the emission rate of a pollutant is Q g s^{-1} and the release rate of particles is N s^{-1}, then the pseudo mass of each particle is Q/N g. Thus one particle in the sampling volume represents a concentration of

$$C = Q/(N\Delta x\Delta y\Delta z). \qquad (B.1)$$

If we desire the accuracy of predicted ground-level concentrations to be greater than *e*, then C must be less than *e*. This relation is used to calculate N as follows,

$$N = Q/(e\Delta x\Delta y\Delta z). \qquad (B.2)$$

Table B.1 shows this relation in tabular form for $\Delta x = \Delta y = 1000$ m and $\Delta z = 25$ m.

Emission rate Q (g/s)	Threshold accuracy e ($\mu g\ m^{-3}$)							
	5	10	15	20	25	30	40	50
250	2.00	1.00	0.67	0.50	0.40	0.33	0.25	0.20
500	4.00	2.00	1.33	1.00	0.80	0.67	0.50	0.40
1000	8.00	4.00	2.67	2.00	1.60	1.33	1.00	0.80
1500	12.00	6.00	4.00	3.00	2.40	2.00	1.50	1.20
2000	16.00	8.00	5.33	4.00	3.20	2.67	2.00	1.60
3000	24.00	12.00	8.00	6.00	4.80	4.00	3.00	2.40
4000	32.00	16.00	10.67	8.00	6.40	5.33	4.00	3.20
5000	40.00	20.00	13.33	10.00	8.00	6.67	5.00	4.00

Table B.1. Particle release rate N s^{-1} needed for concentration threshold accuracy e ($\mu g\ m^{-3}$), as a function of emission rate Q ($g\ s^{-1}$), for $\Delta x = \Delta y = 1000$ m and $\Delta z = 25$ m.

For the model run, we choose a value of 20 $\mu g\ m^{-3}$ for e, which gives N = 2 according to Equation (B.2). Fig.B.1 shows the hourly-averaged *glc* distribution at 1000 LST for contour intervals of 50 (a), 20 (b), and 10 (c) $\mu g\ m^{-3}$. Similarly the 1400 LST *glcs* are plotted in Fig.B.2. Only contours below 80 $\mu g\ m^{-3}$ are plotted for the 10 $\mu g\ m^{-3}$ contour interval to avoid cluttering. At 1000 LST when the plume is still being fumigated to the ground and is relatively narrow, plots at all contour intervals are quite smooth and *when averaged over an hour*, little noise is evident at the sub-threshold concentration of 10 $\mu g\ m^{-3}$. However at 1400 LST when the plume has been dispersed over a wider area by the sea breeze, and by convection, the 10 $\mu g\ m^{-3}$ plot is too noisy to allow any conclusions to be drawn on *glc* distribution at the 10 $\mu g\ m^{-3}$ level. The smoothness of the plot at the pre-set threshold accuracy e of 20 $\mu g\ m^{-3}$ gives us confidence that

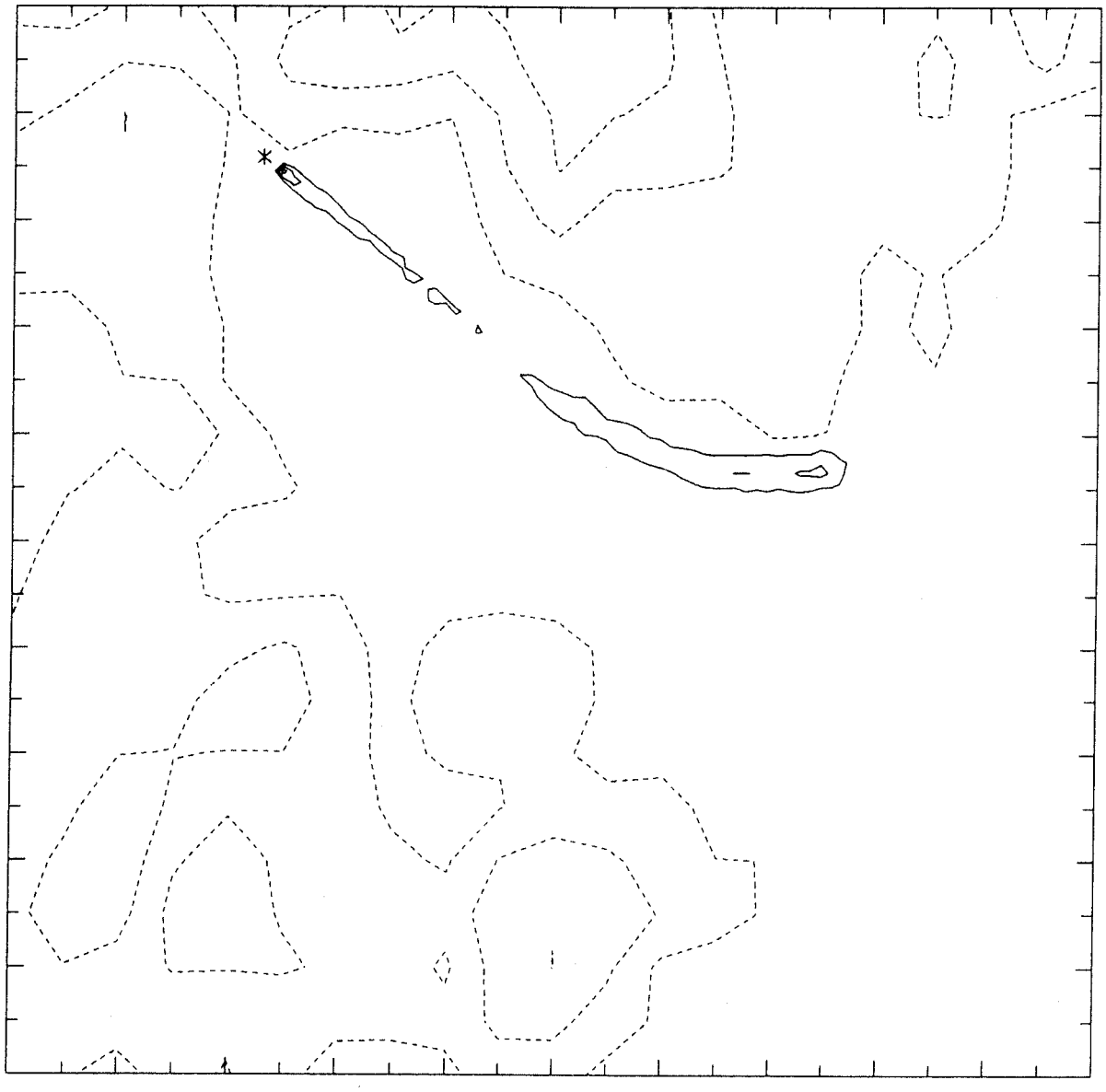

Figure B.1a: Predicted ground-level concentrations of SO_2 (solid lines) for the hourly period ending at 1000 LST. Contour interval is 50 $\mu g\ m^{-3}$. Dashed lines indicate orography contours at a spacing of 200 m. Tick mark interval is 5 km. Asterisk denotes source.

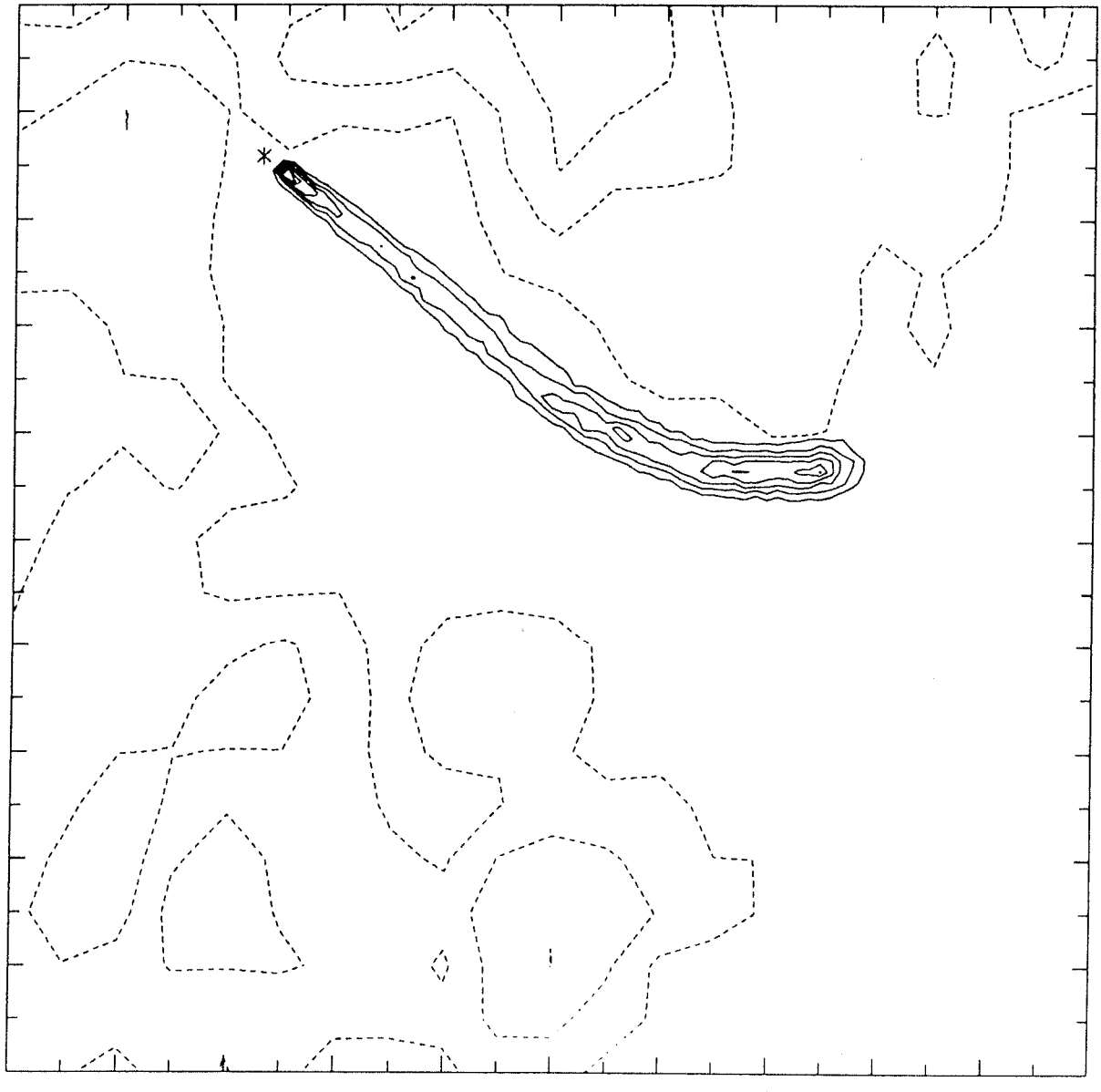

Figure B.1b: Predicted ground-level concentrations of SO_2 (solid lines) for the hourly period ending at 1000 LST. Contour interval is 20 $\mu g\ m^{-3}$. Dashed lines indicate orography contours at a spacing of 200 m. Tick mark interval is 5 km. Asterisk denotes source.

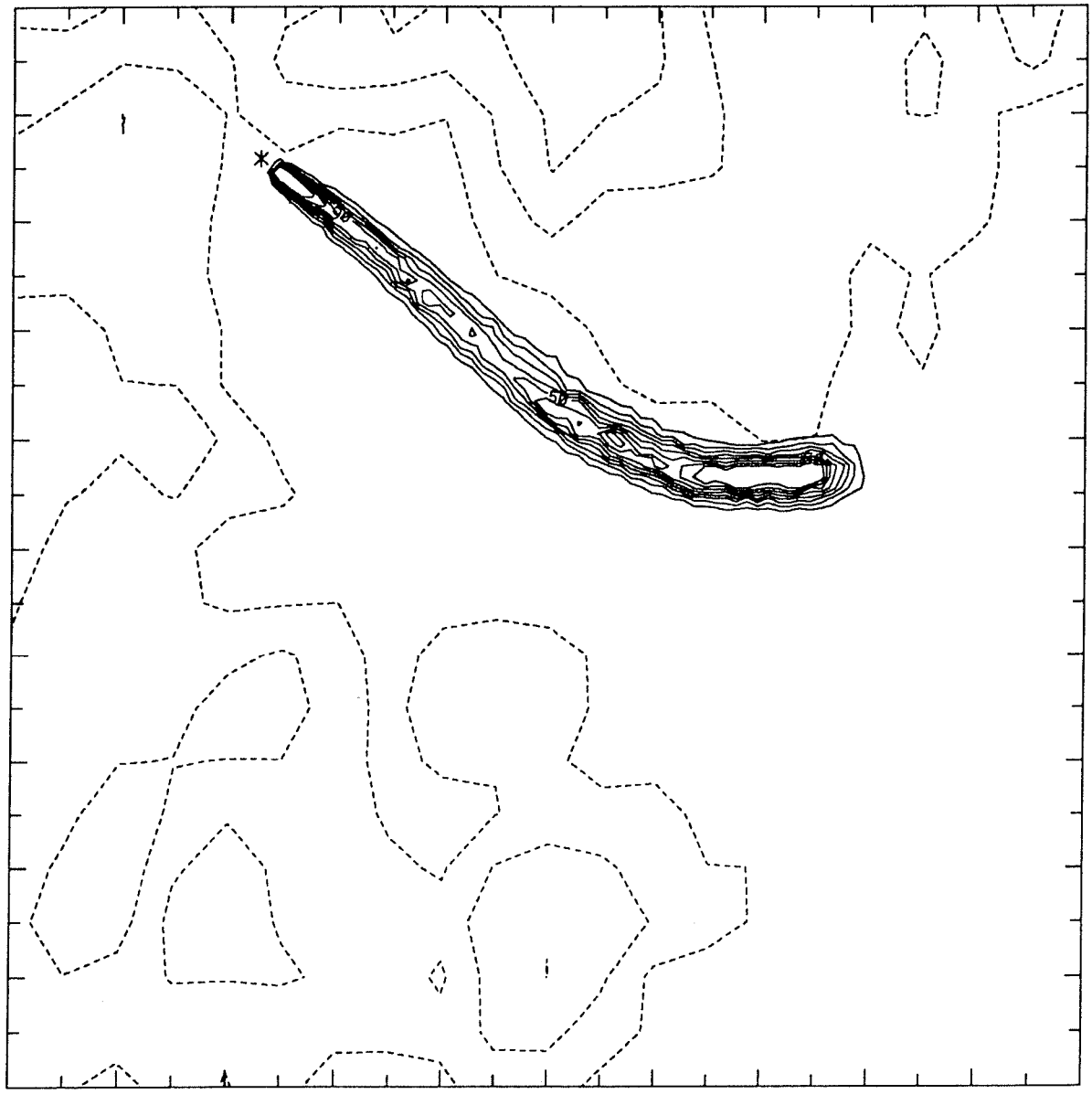

Figure B.1c: Predicted ground-level concentrations of SO_2 (solid lines) for the hourly period ending at 1000 LST. Contour interval is 10 $\mu g\ m^{-3}$. Dashed lines indicate orography contours at a spacing of 200 m. Tick mark interval is 5 km. Asterisk denotes source.

predictions of *glcs* at this value and above do not suffer from insufficient particle problems.

B.2 Particle release rates for near-field concentrations

B.2.1 Size of sampling box

Before investigating the release rates, we determine the size of the sampling box needed for accurate concentrations near the source. The experiments are carried out for a source emitting into a steady convective boundary layer. Parameter values are listed in Table B.2 and box sizes (Δx, Δy, Δz), particle release rates (N) and the corresponding accuracy (e) are shown for each experiment in Table B.3.

Q	h_e	U	z_i	w_*
1000	500	2	1000	2

Table B.2. Values of source strength Q, effective stack height h_e, windspeed U, mixed-layer depth z_i and convective velocity scale w_*.

Expt.	Δx (m)	Δy (m)	Δz (m)	N s^{-1}	e ($\mu g\ m^{-3}$)
1	1000	1000	25	2	20
2	500	500	25	5	32
3	250	250	25	25	26

Table B.3. Experiment details.

Particles are released for a total of 3 hours and an hourly-averaged *glc* is calculated over the final hour. Glcs down the plume centreline (x) for each experiment are shown in Table B.4. Note that in this case, distance x in Table B.4 can also be considered as non-dimensional distance $X = xw^*/(Uz_i)$, due to the choice of parameter values.

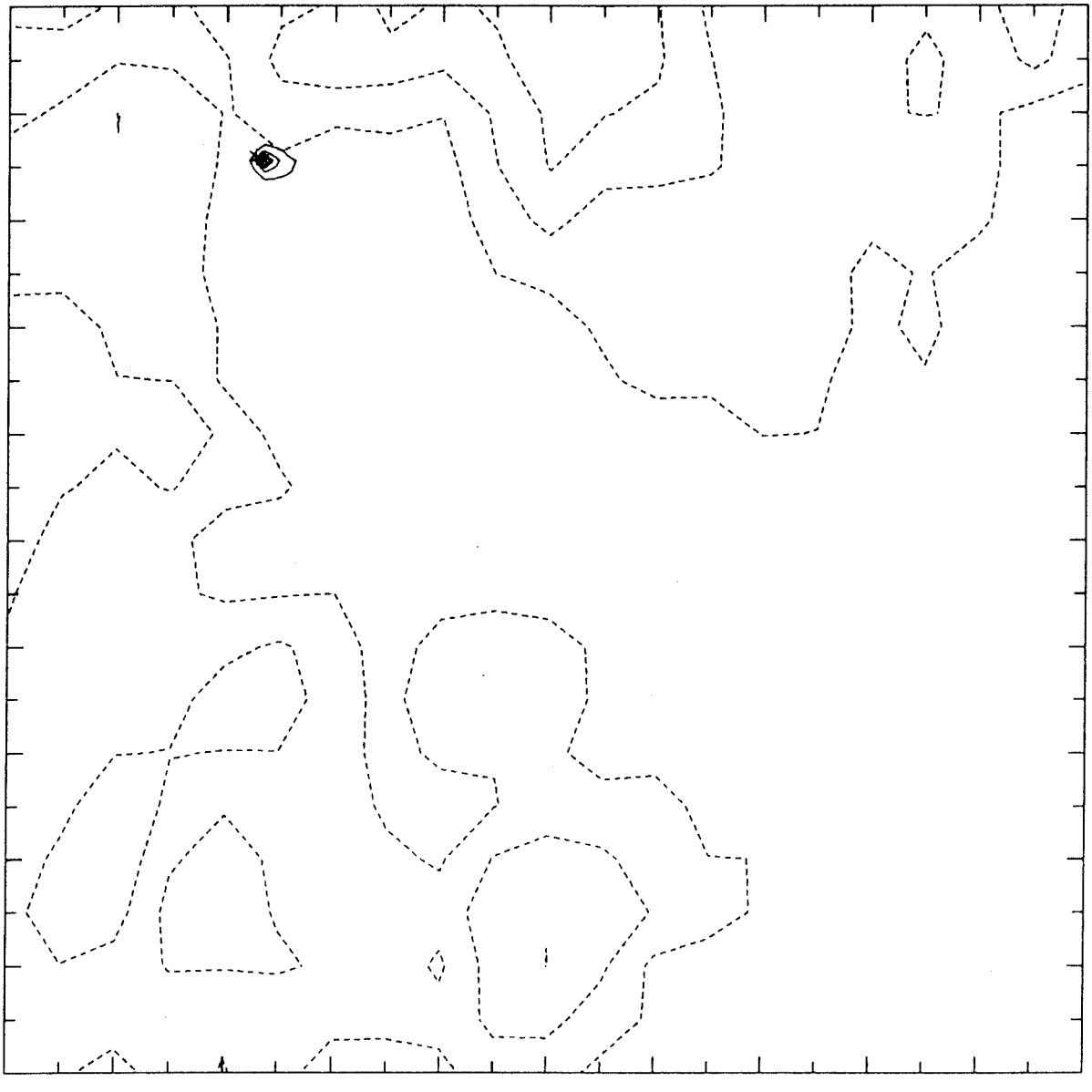

Figure B.2a: Predicted ground-level concentrations of SO_2 (solid lines) for the hourly period ending at 1400 LST. Contour interval is 50 $\mu g\ m^{-3}$. Dashed lines indicate orography contours at a spacing of 200 m. Tick mark interval is 5 km. Asterisk denotes source.

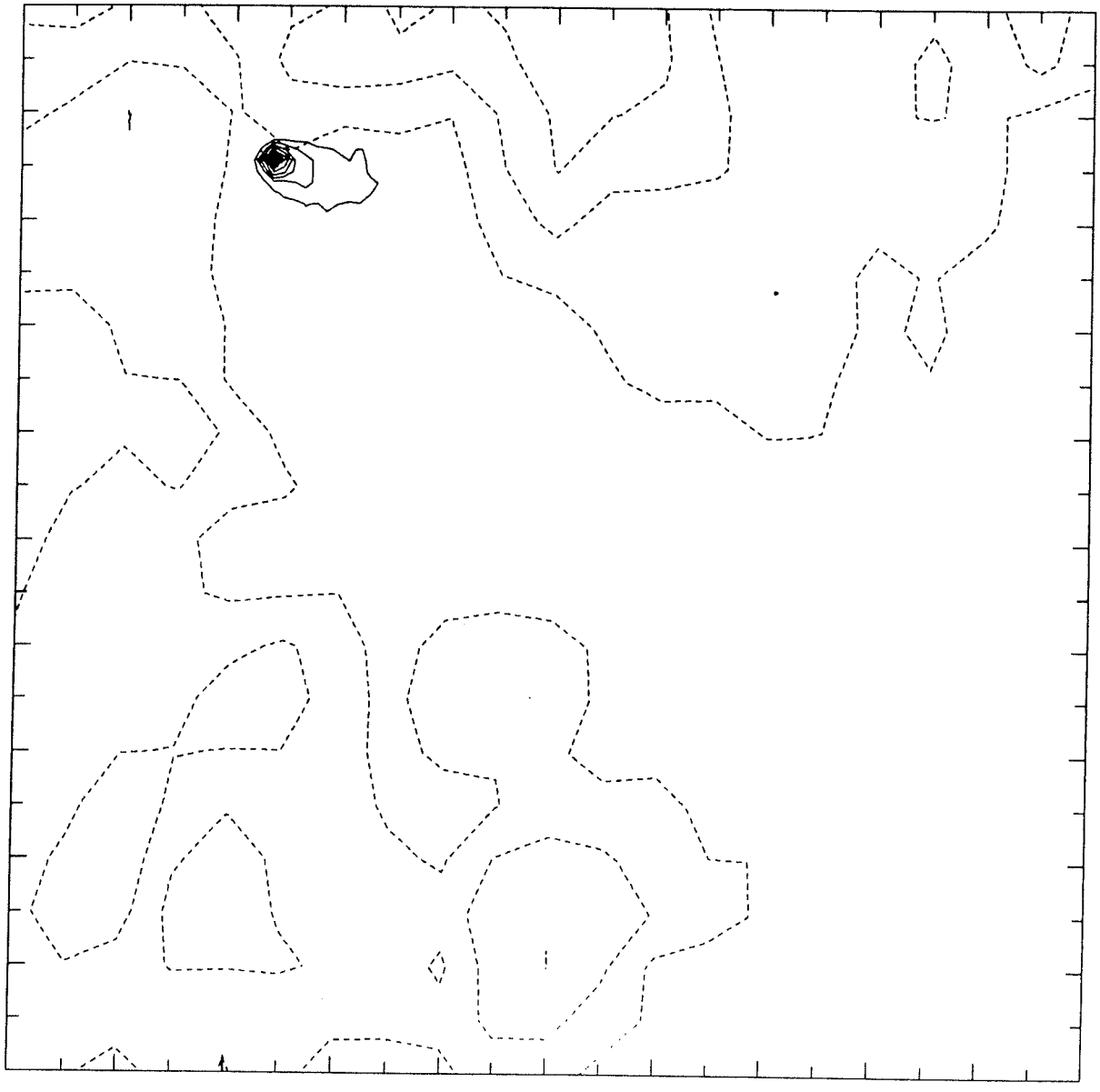

Figure B.2b: Predicted ground-level concentrations of SO_2 (solid lines) for the hourly period ending at 1400 LST. Contour interval is 20 $\mu g\ m^{-3}$. Dashed lines indicate orography contours at a spacing of 200 m. Tick mark interval is 5 km. Asterisk denotes source.

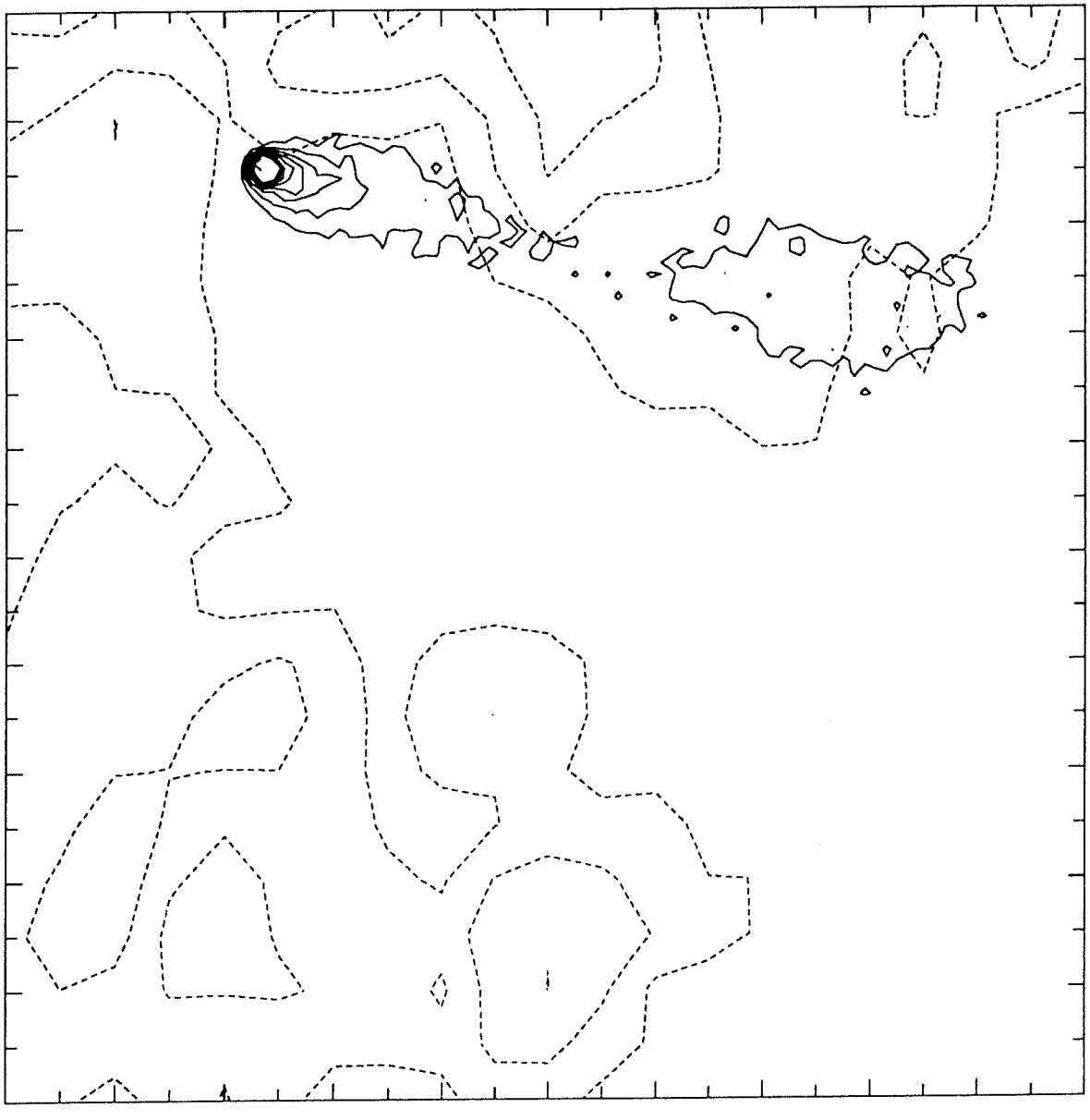

Figure B.2c: Predicted ground-level concentrations of SO_2 (solid lines) for the hourly period ending at 1400 LST. Contour interval is 10 $\mu g\ m^{-3}$. Dashed lines indicate orography contours at a spacing of 200 m. Tick mark interval is 5 km. Asterisk denotes source.

x (km)	Glc ($\mu g\ m^{-3}$) for each experiment 1	2	3
0.25	-	-	48
0.50	-	174	189
0.75	-	-	329
1.00	296	387	401
1.25	-	-	426
1.50	-	385	385
1.75	-	-	378
2.00	290	324	355
2.25	-	-	330
2.50	-	314	297
2.75	-	-	291
3.00	242	282	274
3.25	-	-	279
3.50	-	266	259
3.75	-	-	233
4.00	207	258	221
4.25	-	-	254
4.50	-	225	220
4.75	-	-	217
5.00	199	203	215

Table B.4. Hourly-averaged *glcs* ($\mu g\ m^{-3}$) along the plume centreline for different sampling volumes.

The results shown in Table B.4 are also presented graphically in Fig.B.3, where it can be seen that there is little difference between the 500 and 250 m sampling boxes, suggesting that 250 m is adequate to resolve the plume in the near-stack region. This is consistent with the value of σ_y, derived in the following manner.

If we define $X = xw^*/(Uzi)$ (=x/1000 = x(km))

then $\sigma_y = \sigma_v t$ in the near-stack region

$= 0.6w_* t$

$= 0.6z_i X = 750$ m at max. *glc* location.

From these experiments, we conclude that

(a) a sampling box size of 250 by 250 m is sufficient to resolve the plume and thus eliminate under-prediction of *glcs* in the near-stack region.

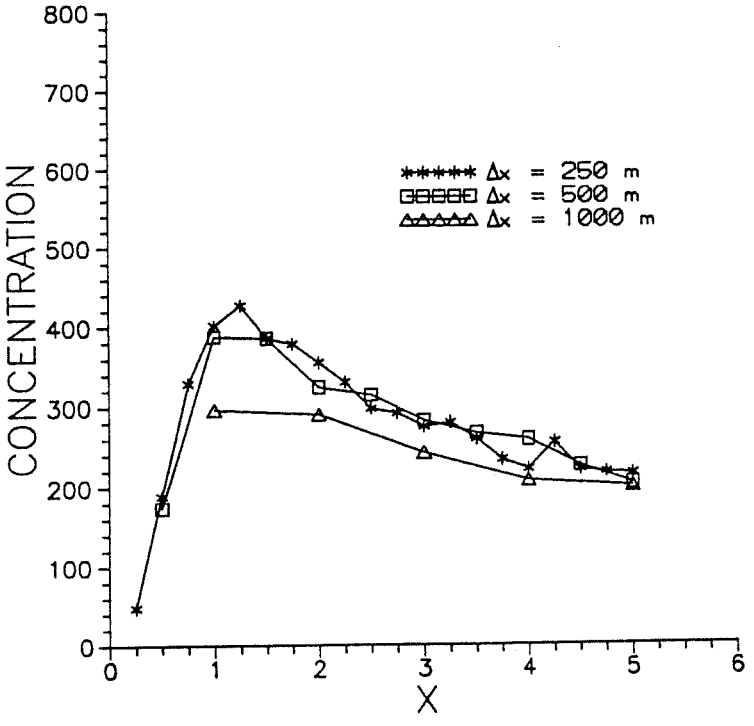

Figure B.3: Predicted ground-level concentrations of SO_2 ($\mu g\ m^{-3}$) as a function of distance downwind for various sampling box sizes (Δx).

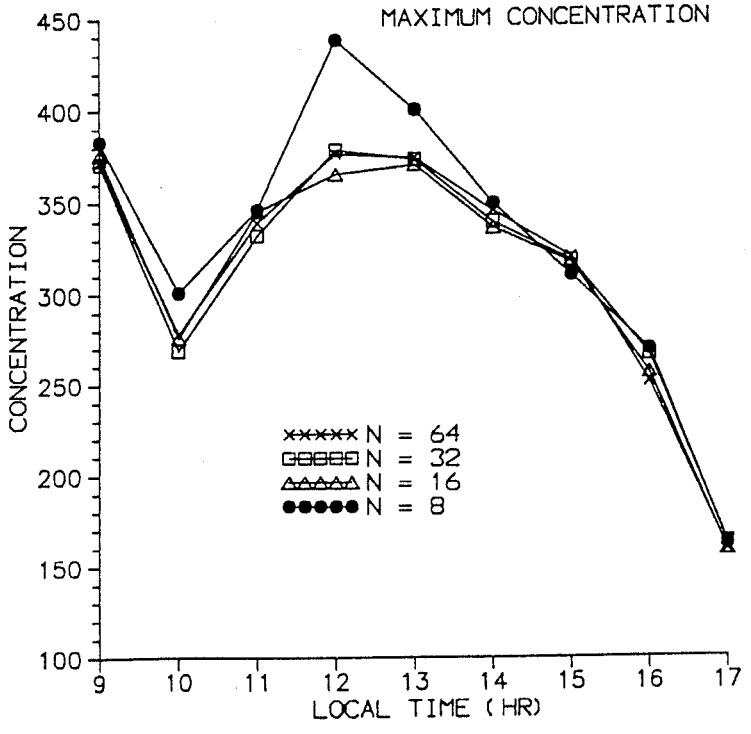

Figure B.4: Diurnal variation of the near-source maximum concentration ($\mu g\ m^{-3}$) for various particle release rates N (s^{-1}).

(b) as far as the resolution problem is concerned, predicted values of near-source maximum *glcs* made with a sampling box of dimensions 1000 by 1000 m underestimate the 'true maximum' by about 45%.

B.2.2 Near-field concentrations

In this section, we examine the effect of the particle release rate N on the value of the near-stack maximum concentration. The source and meteorological conditions in these experiments are the same as in section B.1. The sampling box size is $\Delta x = \Delta y = 250$ m, $\Delta z = 25$ m and we carry out runs for values of N equal to 64, 32, 16 and 8. The highest value used for N (=64) gives a value of 10 $\mu g\ m^{-3}$ for the threshold accuracy *e*. As the maximum concentration under convective conditions (excluding fumigation) occurs within a few kilometres of the source, we restrict the size of our modelling domain to 10 x 10 km. This means that particles are no longer tracked when they pass outside this region.

Maximum concentrations throughout the day are plotted in Fig.B.4 for the various values of N. It can certainly be concluded that there is no advantage in using a larger value for N than 32 and in fact for most purposes N = 16 is quite satisfactory; in this run the largest error is less than 5%, assuming N = 64 is the "correct " solution. The errors associated with N = 8 are unacceptable.

B.3 Downstream compatibility between sampling box sizes

In order to obtain valid predictions for the maximum concentration near the stack, we have shown that it is necessary to sample in this region with a smaller box size (250 m) than that which is sufficient further downwind (1000 m). This implies that further from the stack where the plume is wider, there should be little difference in *glcs* predicted with each box size. This point is illustrated in Figs.B.5 and B.6, where *glcs* from runs with box sizes of 250 and 1000 m are compared. Once again the 29 November 1989 case study day for Liddell was simulated. The release rates N in the runs were 32 and 2 respectively, values which were found previously to give sufficiently accurate *glcs* for each box size. It is seen that the two solutions do indeed differ very little at some point downwind, and that as expected the finer resolution maximum *glc* is considerably higher than the coarser resolution prediction (by 50% at 1000 LST and by 30% at 1400 LST). Note that the results

from the two runs differ less at 1400 LST because the wind direction has been backing over the previous hour and the plume has been laterally dispersed more than at the earlier time.

B.4 Summary

Our experiments have shown that a sampling box of 1000 x 1000 x 25 m is adequate to calculate *glcs* at distances further than 4 to 5 km from the source, and that it is necessary to reduce the box size to 250 x 250 x 25 m to obtain realistic *glcs* closer in. Under convective conditions, a release rate N of 16 particles per second was found to be sufficient for accurate predictions of the near-source maximum *glc*. Further from the source, the release rate needed to obtain results to a pre-set accuracy has been calculated and presented in tabular form for various source strengths.

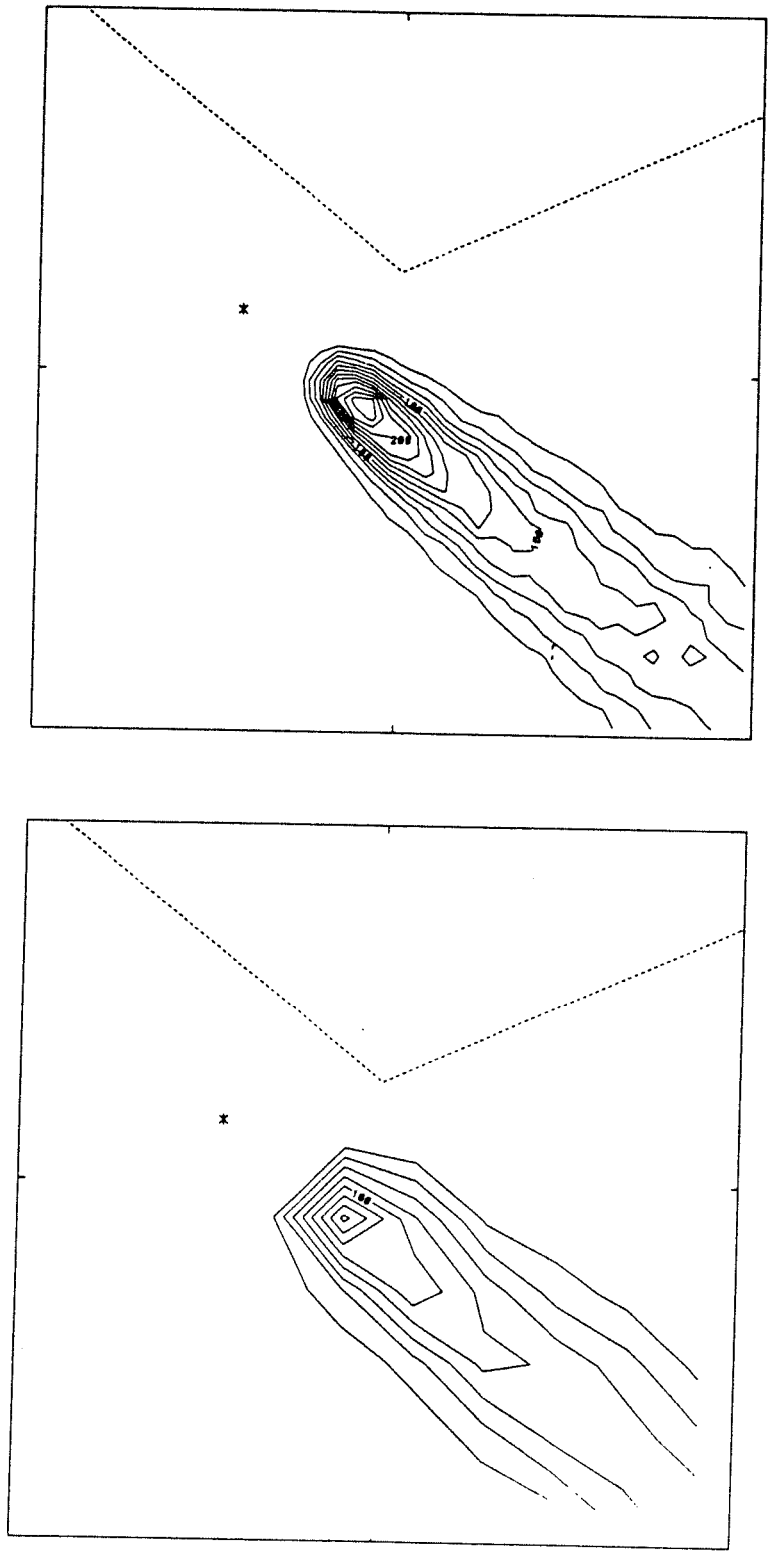

Figure B.5: Predicted ground-level concentrations of SO_2 (solid lines) for the hourly period ending at 1000 LST computed with sampling box sizes of 250 m (top) and 1000 m (bottom). Contour interval is 20 $\mu g\ m^{-3}$. Dashed line indicates an orography contour. Tick mark interval is 5 km. Asterisk denotes source.

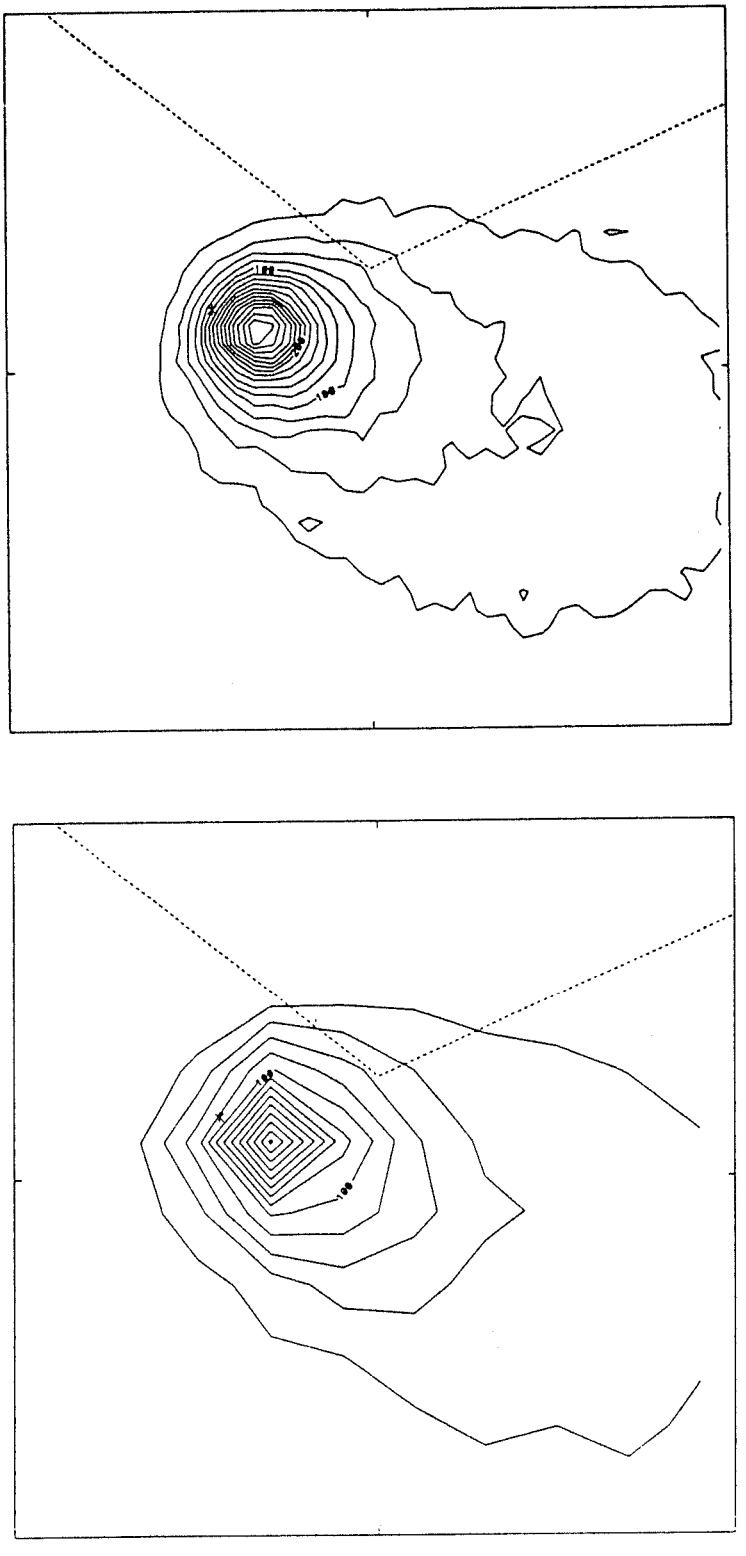

Figure B.6: Predicted ground-level concentrations of SO_2 (solid lines) for the hourly period ending at 1400 LST computed with sampling box sizes of 250 m (top) and 1000 m (bottom). Contour interval is 20 $\mu g\ m^{-3}$. Dashed line indicates an orography contour. Tick mark interval is 5 km. Asterisk denotes source.